The Dissertation Committee for Rodolfo Jose Barniol Duran
certifies that this is the approved version of the following dissertation:

High-Energy Emission and Recent Afterglow Studies
of Gamma-Ray Bursts

Committee:

_____
Pawan Kumar, Supervisor

_____
Duane Dicus, Supervisor

_____
Sonia Paban

_____
John C. Wheeler

_____
Miloš Milosavljević

High-Energy Emission and Recent Afterglow Studies of Gamma-Ray Bursts

by

Rodolfo Jose Barniol Duran, B.S.

DISSERTATION

Presented to the Faculty of the Graduate School of

The University of Texas at Austin

in Partial Fulfillment

of the Requirements

for the Degree of

DOCTOR OF PHILOSOPHY

THE UNIVERSITY OF TEXAS AT AUSTIN

May 2011

Dedicated to my wife Jessa.

Acknowledgments

It has been a true privilege to work with Professor Pawan Kumar these past years. He has been extremely generous with his time, patience and knowledge. Without hesitation, I can say that he has been the best teacher I have ever had. I am grateful for invaluable conversations with Pawan Kumar about science, but also for teaching me about honesty and integrity, and for always motivating me to do the best work I can.

I want to thank Rongfeng Shen for his guidance during my first year in Pawan Kumar's research group. He did an excellent job introducing me to high-energy astrophysical concepts and explaining to me many astronomical observations.

I want to thank Jarrett Johnson, Erin McMahon, Patrick Crumley, Rodolfo Santana and Chris Lindner for very interesting and useful discussions.

I had the wonderful opportunity in the past two years to collaborate with Professor Guido Chincarini and Raffaella Margutti at the Brera Astronomical Observatory in Merate, Italy. I want to thank them for believing in my work even at the early stages of my life as a researcher.

I want to thank Eliot Quataert, Ramesh Narayan, Miloš Milosavljević, Ehud Nakar and Tsvi Piran for invaluable discussions.

I want to gratefully acknowledge support from the Lawrence C. Biedenharn Endowment for Excellence for the past year. This endowment allowed me to concentrate on research and freed up my time, allowing me to travel with

the purpose of fostering collaborations and presenting my work at different Universities.

Special thanks go to my parents, Rodolfo and Luly Barniol, my brothers, Pablo, Julio and Sebastian, my extended family and friends both in Ecuador and Mexico, and my mother-in-law and sister-in-law, Taria and Abbie Hollett. Their support during all these years has been very much appreciated.

Finally and more importantly, I want to thank my wife, Jessa Barniol, to whom this dissertation is dedicated, for always being patient and supportive of my work. It has been a privilege and immense joy to share our lives together during these past years and I look forward to the future with great enthusiasm and optimism.

High-Energy Emission and Recent Afterglow Studies
of Gamma-Ray Bursts

Publication No. _____

Rodolfo Jose Barniol Duran, Ph.D.
The University of Texas at Austin, 2011

Supervisors: Pawan Kumar
Duane Dicus

Gamma-ray Bursts (GRBs) are powerful explosions that emit most of their energy, as their name suggests, in gamma-rays of typical energies of about 1 MeV. This emission lasts for about two minutes or less and it is called the prompt emission. The isotropic energy radiated in GRBs is equivalent to the energy that the Sun will radiate in its entire lifetime. After decades of studying this cosmological phenomenon, we have come to learn that it involves a collimated and relativistic jet. Also, we know that they radiate energy in the X-ray, optical and radio bands for days, weeks and years, respectively, which is called the afterglow. Recently, NASA's *Fermi* Satellite was launched and, in addition to MeV photons, it detected GeV photons from these astrophysical sources. We show that these GeV photons are produced when the GRB jet interacts with the medium that surrounds it: the external forward shock model. We arrive at this conclusion not only by studying the GeV emission, but also by studying the afterglow observations (Chapter 2). We corroborate this model by studying the electron acceleration in the external forward shock

model and find that electrons can radiate at the maximum observed energy of ~ 10 GeV (Chapter 3). We also provide an extensive analysis of the most recent afterglow observations of GRB 090902B within the same framework of an external forward shock origin. We find that the data for this burst requires a small deviation from the traditionally used power-law electron energy distribution, however, our previous results remain unchanged (Chapter 4). To conclude, we use the end of the prompt emission phase, which exhibits a steep X-ray temporal decay, to constrain the behavior of the central engine responsible for launching the relativistic jet (Chapter 5).

Table of Contents

List of Tables

xiii

List of Figures

2.1 We determine the sub-space of the 4-D parameter space (for the forward external forward shock model with $s = 0$) allowed by the high energy data for GRB 090902B at t=50 s as described in Section 2.3.1. The projection of the allowed subspace onto the ϵ_B–n plane is shown in this figure (dots); the discrete points reflect the numerical resolution of our calculation. We also plot the expected ϵ_B for a shock compressed CSM magnetic field of 5 and 30 μG as the green and blue lines respectively; for a CSM field of strength B_0, the value of ϵ_B downstream of the shock-front resulting from the shock compressed CSM field is $\approx B_0^2/(2\pi nm_pc^2)$, where nm_p is the CSM mass density, and c is the speed of light. Note that no magnetic field amplification is needed, other than shock compression of a CSM magnetic field of ~ 30 μG, to produce the >100 MeV photons. The synchrotron injection and cooling frequencies at $t = 50$ s for the sub-space of 4-D parameter space allowed by the high energy data are 100 eV $\lesssim \nu_i \lesssim 3$ keV and 30 MeV $\lesssim \nu_c \lesssim 100$ MeV respectively, the Lorentz factor of the blast wave at $t = 50$ s lies between 330 and 1500, and 10^{55} erg $\lesssim E_{KE,iso} \lesssim 3 \times 10^{55}$ erg. Note that at 0.5 d ν_i would be below the optical band, and $\nu_c > 1$ MeV, and these values are consistent with the X-ray spectrum and the X-ray and optical decay indices at this time.   29

2.2 The optical and X-ray fluxes of GRB 090902B predicted at late times using only the high energy data at 50 s (assuming synchrotron emission from external forward shock) are shown in the right half of this figure, and the predicted flux values are compared with the observed data (discrete points with error bars). The width of the region between the green (magenta) lines indicates the uncertainty in the theoretically predicted X-ray (optical) fluxes (the width is set by the error in the measurement of 100 MeV flux at 50 s, and the error in the calculation of external forward shock flux due to approximations made – both these contribute roughly equally to the uncertainty in the predicted flux at late times). LAT (X-ray) data red (black) circles, are from Abdo et al. 2009d (Evans et al. 2007, 2009) and were converted to flux density at 100 MeV (1 keV) using the average spectral index provided in the text. Optical fluxes are from Swenson et al. 2009 (square) and Guidorzi et al. 2009 (triangle) and were converted to flux density using 16.4 mag ≈ 1 mJy. The blue dashed line shows schematically the light curve observed by *Fermi*/GBM. The predicted value for the radio flux at one day has a very large range (not shown), but consistent with the observed value.   30

xvii

xviii

Chapter 1

Introduction

1.1 What is a Gamma-Ray Burst?

Gamma-Ray Bursts (GRBs) are very intense flashes of gamma-rays that last anywhere from a fraction of a second to several hundred seconds; for a general review of GRBs see Piran (2004), Mészáros (2006), Woosley & Bloom (2006), Zhang (2007), Gehrels, Ramirez-Ruiz & Fox (2009). The isotropic energy in these gamma-rays is very large, comparable to the energy the Sun will radiate in all of its lifetime. Since gamma-rays are absorbed by our atmosphere, they are observed with gamma-ray detectors onboard man-made satellites that orbit the Earth. With the current GRB satellites, GRBs are detected a few times a day. GRBs are detected from random directions in the sky and they arrive from cosmological distances.

1.2 The prompt emission

Gamma-rays from a GRB show very strong variability in their light curves (Figure 1.1) and also show a non-thermal spectrum. The spectrum has been phenomenologically fitted by a "Band function" (Band et al. 1993), which is described by two smoothly connected power-laws. The specific flux below and above the peak of the spectrum asymptotically behaves with frequency ν as $\propto \nu^{-\beta}$, where $\beta \approx 0$ and $\beta \approx 1.2$, respectively, and the peak energy of the spectrum is typically ~ 300 keV (Preece et al. 2002). It is interesting to note

that the high energy part of the Band spectrum extends to at least several MeV.
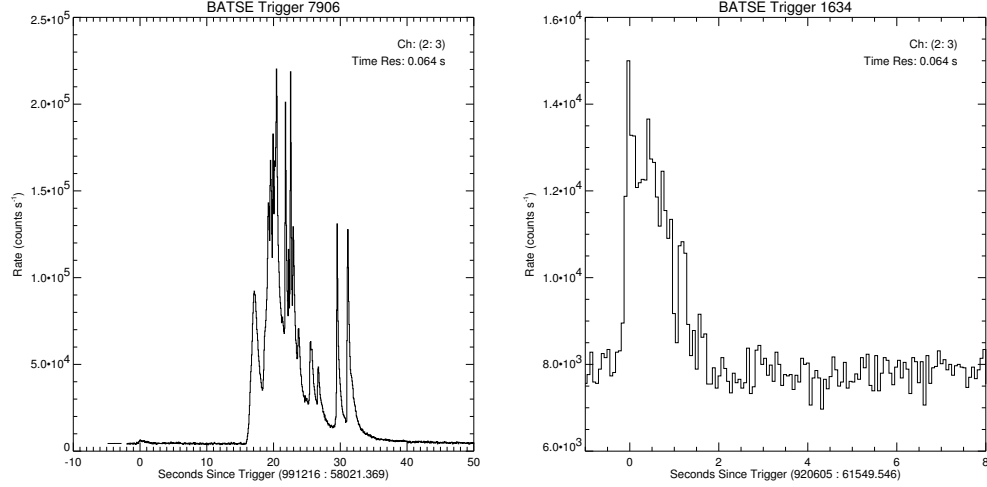
Figure 1.1: The gamma-ray emission of a long and a short GRB (left and right, respectively) detected by BATSE (Burst and Transient Source Experiment) onboard NASA's CGRO (from Kaneko et al. 2006).

The Compton Gamma-Ray Observatory (CGRO) – a NASA satellite – determined that there were two types of GRBs: short and long ones (Kouveliotou et al. 1993, see Figure 1.2). Short bursts are those that last for less than about 2 s in duration and long GRBs last longer than about 2 s (Kouveliotou et al. 1993). Also, short GRBs are typically "harder" compared to their long counterparts. The term harder here simply means that the ratio of count rate in a high energy band (100 - 300 keV) compared to a lower energy band (50 - 100 keV) is larger. The short-lived gamma-rays from a GRB are referred to as the "prompt" emission.

2
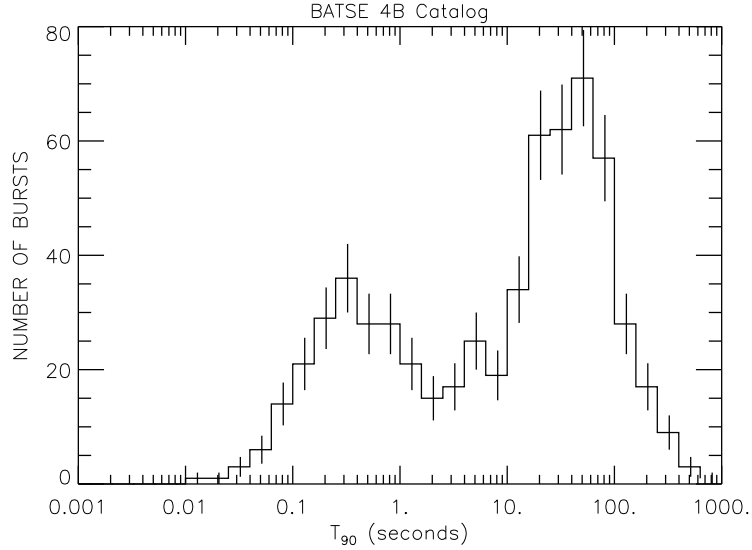
Figure 1.2: GRB durations of the 4B Catalog detected with BATSE. T_{90} is the time over which a GRB emits from 5% to 95% of its total measured counts. Short and long GRB populations can be clearly seen (from Kaneko et al. 2006).

1.3   The afterglow emission

The astronomical community first learned about GRBs in 1973 (Klebesadel et al. 1973). However, it wasn't until 1997 that an X-ray satellite, BeppoSAX, was able to follow-up a GRB with an X-ray detector a few hours after the end of the prompt emission. This X-ray detection allowed for a better determination of the position of the GRB in the sky. With this position, optical and radio telescopes on Earth were able to point at this direction in the sky and detect emission from the same source. The optical and radio radiation were seen for a few days and months, respectively. This long-lasting emission is called the "afterglow", and it is the emission that follows the prompt phase at lower energies (X-ray, optical, radio) for very long timescales: from days to months (Costa et al. 1997, van Paradijs et al. 1997, Frail et al. 1997). GRB

3

afterglow specific fluxes have a power-law dependence on frequency ν and time t as $f_\nu \propto t^{-\alpha} \nu^{-\beta}$, where $\alpha \sim 1.2$ and $\beta \sim 0.9$ (Piro 2001).

Afterglow observations answered some of the basic questions regarding these objects that had been mysterious for many years. By identifying the "host galaxies", where the optical afterglow originated, it was possible to spectroscopically determine the distance (redshift) to the host galaxy, and it was concluded that these events happened at cosmological distances (Bloom, Djorgovski & Kulkarni 2001, see also Meegan et al. 1992). Also, distance measurements enabled the determination of the energy emitted in gamma-rays, which was found to be as large as $\sim 10^{54}$ erg. After carefully monitoring radio afterglows and determining how the size of the radio remnant changed with time, they confirmed that the remnant was moving relativistically (Frail et al. 1997, Taylor et al. 2004). This confirmed previous claims that in order to avoid pair-production that would prevent us from detecting MeV gamma-rays in the first place (the "compactness problem", see, e.g., Ruderman 1975, Piran 1997, Lithwick & Sari 2001), the emitting source should be moving relativistically towards us. The current understanding of the afterglow radiation is that it is produced when the relativistic outflow from GRBs interacts with the medium surrounding the explosion and drives a forward shock that heats the medium, which radiates via synchrotron emission: the external forward shock model (see, e.g., Rees & Mészáros 1992, Mészáros & Rees 1993, Paczyński & Rhoads 1993). The distance from the center of the explosion to the site at which the GRB outflow interacts with the surrounding medium depends on the energy in the explosion, the density of the medium and the Lorentz Factor of the outflow, however, typical values range from $10^{16} - 10^{18}$ cm. This model has been successful in explaining afterglow observations, which showed

a typical $\sim t^{-1}$ decline in their light curves.

It was discovered that many optical light curve decays steepen a few days after the explosion, which was an evidence for the fact that the material ejected relativistically in GRBs is narrowly collimated or beamed (Rhoads 1999, Sari et al. 1999). This can be understood as follows. Due to the "relativistic beaming effect" we can only see photons coming from a small opening angle equal to the inverse of the Lorentz Factor of the source. As the outflow collects more and more of the interstellar medium and its Lorentz Factor decreases, we see more and more of the outflow. When the Lorentz Factor drops to a value that is the inverse of the outflow opening angle we begin to see the entire GRB jet and at that time the light curve steepens from $\sim t^{-1}$ to $\sim t^{-2}$ (see Figure 1.3). This allows us to determine the angle of the GRB jet, which is found to be $\sim 2 - 20°$ (Frail 2001, Panaitescu & Kumar 2001). This collimation reduces the energy released in gamma-rays to be $\sim 10^{51}$ erg (Panaitescu & Kumar 2001, Piran et al. 2001), which is still enormous, but more reasonable for a stellar mass object to produce.

Prior to the launch of the NASA *Swift* satellite it usually took about half a day after the prompt phase of a GRB for X-ray, for optical and radio telescopes to point at the site where the gamma-rays where produced, and the majority of the data seemed to be explained very well by the external forward shock model. This model also predicts the existence of an external reverse shock (see, e.g., Mészáros & Rees 1997, Wen, Panaitescu & Mészáros 1997) that travels through the GRB jet, heating the particles in the jet, which radiate via synchrotron emission. However, this emission was predicted to be short-lived, to appear close to the end of the prompt phase, to peak at the optical band, to be very bright and to decay very quickly as $\sim t^{-2}$ (see, e.g.,

5
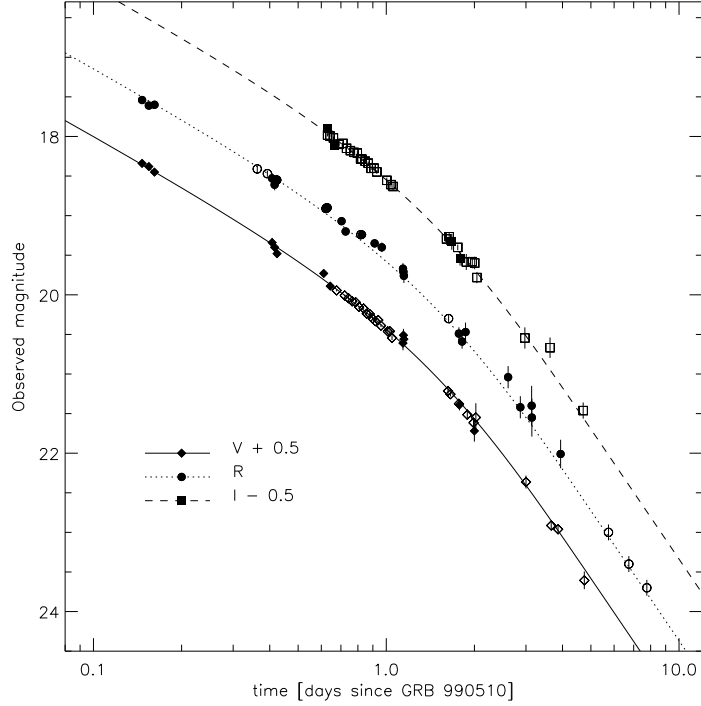
Figure 1.3: Example of an optical afterglow light curve. The various symbols correspond to different optical filters. The optical afterglow decays as $\sim t^{-1}$ until about a day, when the "jet break" is evident and the light curve steepens to $\sim t^{-2}$. The break can be seen in all different optical bands (from Harrison et al. 1999).

Sari & Piran 1999a). To test this hypothesis, one would have to be able to point an optical telescope to the location of the GRB very quickly. This has now been achieved for many GRBs and in a few cases a bright, short-lived, optical flash has been detected (Akerlof et al. 1999, Fox et al. 2003, Li et al. 2003, Boer et al. 2006, Klotz et al. 2006, Roming et al. 2006). There are several uncertainties that plague the calculation of the external reverse shock emission, for example, one needs to assume the composition of the GRB

jet. The previous predictions were done for a baryonic GRB jet, however, if one assumes that most of the energy in the GRB jet is in magnetic fields (Poynting jet), then one expects the emission of the external reverse shock to be weak (Fan et al. 2002, Zhang et al. 2003, Fan, Wei & Wang 2004, Zhang & Kobayashi 2005, Giannios et al. 2008).

1.4   Supernova connection, Host Galaxies and Progenitors

An important clue in the GRB phenomenon appeared in 1998, when a supernova explosion was seen associated with a GRB (Galama et al. 1998). We now have several spectroscopically confirmed cases of supernovae following long GRBs (see, e.g., Woosley & Bloom 2006), and other cases in which a "red bump" can be detected in their optical afterglows (Bloom et al. 1999), consistent with the expectations of a supernova accompanying the GRB. Supernovae are classified by different types and the ones that are associated with GRBs are Type Ic, which are produced by the collapse of a massive star that has lost its Hydrogen and Helium envelopes.

The host galaxies of long GRBs are typically dwarf spiral or irregular starburst galaxies. Short GRBs, on the other hand, are hosted by both early and late-type (spiral and elliptical) galaxies. The specific star-formation rate in long GRB hosts is about 10 solar masses per year (Christensen, Hjorth & Gorosabel 2004), while the specific star formation rate of short GRB late-type hosts is more than a factor of 10 smaller (Nakar 2007). Also, short GRBs are located at a large offset from the center of their host galaxies, consistent with the idea that they could be produced by the merging of two compact objects that are in a binary system (see, e.g., Fong, Berger & Fox 2010). The fact

that they show an offset is consistent with the "kick" that binary systems gains when one of the stars explodes as a supernova to become a compact object.

The current paradigm in regards of the progenitors of GRBs is the following: Long GRBs, since they appear in star forming regions and are associated with supernovae, are produced from massive stars when they undergo collapse (Woosley 1993, MacFadyen & Woosley 1999); short GRBs, since some of them belong to an older stellar population, are thought to be produced by the merging of a neutron star - black hole binary (Eichler et al. 1989, Paczyński 1991, Narayan, Paczyński & Piran 1992) or a neutron star - neutron star binary. In both cases, the resulting object is likely a black hole.

1.5   The *Swift* Satellite

The *Swift* Satellite was launched at the end of 2004 (Gehrels et al. 2004). This satellite was designed to detect gamma-rays in the energy range 15 - 150 keV with BAT (Burst Alert Telescope). In less than about 90 s after the detection of the gamma-rays, the satellite rotates and points both the XRT (X-ray Telescope: 0.3 - 10 keV) and the UVOT (UV/Optical Telescope: 170 - 600 nm) to the location of the sky where the gamma-rays were detected by BAT.

Swift has bridged the gap that existed between the afterglow observations that started usually at about 7 hours or more after the end of the prompt phase. Before *Swift*, people thought that afterglow fluxes would simple extrapolate backwards in time with a single power-law, however, most GRBs show a complicated behavior. More than two thirds of all GRBs detected by *Swift* exhibit a "X-ray canonical light curve" (see Figure 1.4), whose flux shows the following temporal behavior: (i) a steep decay ($\sim t^{-3}$) that follows the end

of the prompt phase and ends at ~ 500 s, followed by (ii) a shallow decay or plateau ($\sim t^{-0.5}$) that ends at $\sim 10^4$ s, followed by a (iii) "normal decay" ($\sim t^{-1.2}$), called normal because this is the typical decay index that was observed in afterglows before *Swift* (Zhang 2007). After this decay, it is also sometimes possible to see the "jet break" that was detected in pre-*Swift* data.
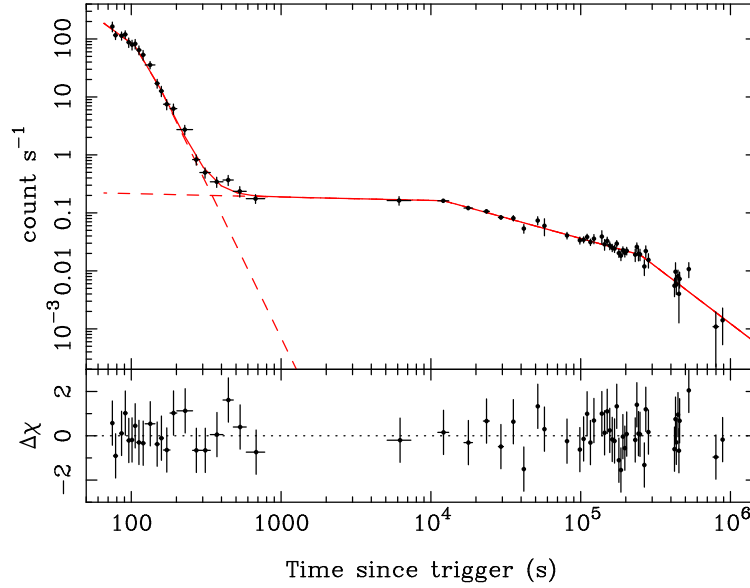
Figure 1.4: The *Swift* GRB 050315 X-ray light curve in the 0.3 - 5 keV band. This GRB clearly exhibits the X-ray canonical light curve. The filled circles show the X-ray detections while the solid line shows the result of the best fit. The lower panel shows a measure of the deviation of the data to the best fit (from Vaughan et al. 2006).

In addition to this interesting X-ray canonical light curve, *Swift* found X-ray flares, which are high amplitude, short duration spikes seen superimposed on the X-ray light curve. These X-ray flares appear in every segment of the canonical light curve (Falcone et al. 2006, Chincarini et al. 2007).

9

1.6 The *Fermi* Satellite

The *Fermi* Satellite was launched in 2008. One of the main objectives of this telescope was to study the high-energy behavior of GRBs. *Fermi* has onboard two detectors: the GBM (Gamma-ray Burst Monitor) and the LAT (Large Area Telescope). The GBM covers an energy range of ~ 10 keV - 40 MeV, while the LAT covers an energy range of 20 MeV - 300 GeV.

Fermi has allowed us to study, with better sensitivity, the high-energy photons from GRBs. There are a few key discoveries regarding GRBs that have been made by *Fermi* (Abdo et al. 2009a). 1. The first > 100 MeV photons arrive a few seconds after the first sub-MeV photons (left panel of Figure 1.5). 2. The duration of the sub-MeV photons varies from a fraction of a second to a few tens of seconds, whereas the duration of the > 100 MeV signal is much longer, usually ~ 1000 s, and that duration is only limited by the sensitivity of the instrument (right panel of Figure 1.5, top). 3. The spectrum of both signals, the sub-MeV one and the > 100 MeV one, can together be fitted with a Band function, while both the sub-MeV and > 100 MeV are active. When the sub-MeV signal disappears and the > 100 MeV remains, the > 100 MeV emission is well-fitted with a single power-law (right panel of Figure 1.5, bottom).

1.7 The Big Questions

In this introductory chapter we have not addressed the origin of the GRB prompt phase, because its origin is still uncertain. The most popular model is the "internal shock" model, in which the GRB jet exhibits a variable speed (e.g., Rees & Mészáros 1994, Paczyński & Xu 1994). In this model,

the faster parts of the jet "catch up" and interact with the slower moving parts driving a shock that heats the particles in the jet. The particles radiate via synchrotron emission or synchrotron-self-Inverse Compton scattering and they produce the gamma-ray photons at a typical distance from the center of the explosion of $\sim 10^{13}$ cm. However, this model has proven to have serious problems (Kumar & McMahon 2008, Kumar & Narayan 2009, Zou, Piran, Sari 2009).

Alternative models to the internal shock have been put forward (Thompson 1994, Lyutikov & Blandford 2003, Kumar & Narayan 2009, Lazar et al. 2009) and other emission mechanisms, like the photospheric emission (Mészáros & Rees 2000, Rees & Mészáros 2005, Pe'er, Mészáros & Rees 2006, Giannios & Spruit 2007, Ryde & Pe'er 2009, Beloborodov 2010) and the jitter radiation (Medvedev & Loeb 1999, Workman et al. 2008, Morsony et al. 2009), however, more work is needed to pinpoint the precise way that Nature behaves in this tremendous explosions.

A few decades after the the discovery of the first GRB, we still cannot answer with any degree of certainty two basic questions: 1. How is the energy in the relativistic GRB jet converted to particle thermal energy? 2. Which radiation process converts the particle energy to gamma-ray photons? There are three other important questions tied with the previous two and they are: 3. What is the composition of the GRB jet? 4. What is the central engine? 5. How are particles accelerated in relativistic shocks?

The launch of *Fermi* in 2008 offered a new opportunity to answer some of these basic questions. We have devoted most of our time and effort to developing a model that explains the *Fermi* GRB observations (Chapters 2, 3 and 4). This model answers questions 1 and 2 above, however, it only

explains the > 100 MeV emission, not the sub-MeV one, which still remains a mystery. We have also contributed to question 5 above by studying the particle acceleration that leads to > 100 MeV radiation (Chapter 3) and also to the lower energy emission (Chapter 4). Finally, we provide strong constraints on question 4 above on the central engine (Chapter 5) by studying the early X-ray steep decay seen in GRB light curves and by explaining how the central engine must behave after the prompt phase is over.
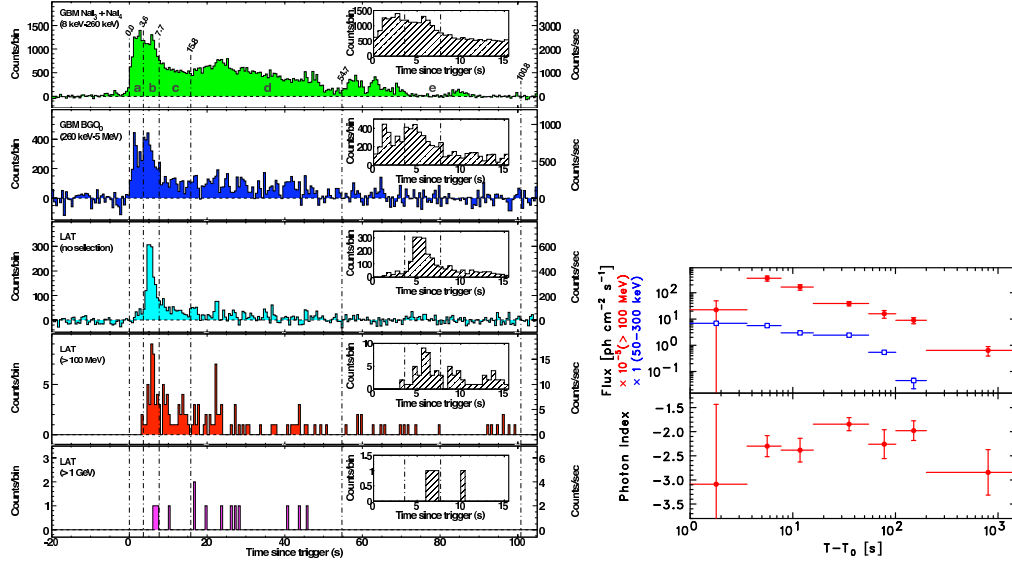
Figure 1.5: The light curve of GRB 080916C in different energy channels (left panel). Note that the fourth panel from top to bottom does not show any counts starting at 0 s until about 3 s. The light curve of GRB 080916C in two energy bands (right panel, top), > 100 MeV (filled circles) and 50 - 300 keV (empty squares). Note how the > 100 MeV light curve lasts for ~ 1000 s, while the lower energy one starts to decay rapidly at a few tens of seconds. The huge error bar of the first > 100 MeV data point comes from the fact that almost no > 100 MeV photons are detected in this time interval. The > 100 MeV emission photon index is shown in the bottom right panel (from Abdo et al. 2009a).

Chapter 2

External forward shock origin of high energy emission for three GRBs detected by *Fermi*

2.1 Introduction

The *Fermi* Satellite has opened a new and sensitive window in the study of GRBs. So far, *Fermi* has detected 18 GRBs with photons with energies >100 MeV. The $>10^2$ MeV emission of most bursts detected by the LAT (Large Area Telescope: energy coverage 20 MeV to >300 GeV) instrument aboard the *Fermi* satellite shows two very interesting features (Omedei et al. 2009): (1) The first >100 MeV photon arrives later than the first lower energy photon ($\lesssim 1$ MeV) detected by GBM (Gamma-ray Burst Monitor), (2) The >100 MeV emission lasts for much longer time compared to the burst duration in the sub-MeV band (the light curve in sub-MeV band declines very rapidly).

There are many possible >100 MeV photons generation mechanisms proposed in the context of GRBs; see Gupta & Zhang (2007) and Fan & Piran (2008) for a review. Shortly after the observations of GRB 080916C (Abdo et al. 2009a), we proposed a simple idea: the >100 MeV photons in GRB 080916C are produced via synchrotron emission in the external forward shock (Kumar & Barniol Duran 2009). This proposal naturally explains the observed delay in the peak of the light curve for >100 MeV photons – it corresponds to the deceleration time-scale of the relativistic ejecta – and also the long lasting >100 MeV emission, which corresponds to the power-law decay nature of the

external forward shock (ES) emission (the ES model was first proposed by Rees & Mészáros 1992, Mészáros & Rees 1993, Paczyński & Rhoads 1993; for a comprehensive review of the ES model, see, e.g., Piran, 2004, and references therein). Following our initial analysis on GRB 080916C, a number of groups have provided evidence for the external forward shock origin of *Fermi*/LAT observations (Gao et al. 2009; Ghirlanda, Ghisellini, Nava 2010; Ghisellini, Ghirlanda, Nava 2010; De Pasquale et al. 2010).

In this chapter we analyze the >100 MeV emission of GRB 090510 and GRB 090902B in detail, and discuss the main results of our prior calculation for GRB 080916C (Kumar & Barniol Duran 2009), to show that the high energy radiation for all these three arose in the external forward shock via the synchrotron process. These three bursts - one short and two long GRBs - are selected in this work because the high energy data for these bursts have been published by the *Fermi* team as well as the fact that they have good afterglow follow-up observations in the X-ray and optical bands (and also the radio band for GRB 090902B) to allow for a thorough analysis of data covering more than a factor 10^8 in frequency and $> 10^4$ in time to piece together the high energy photon generation mechanism, and cross check this in multiple different ways.

In the next section (Section 2.2) we provide a simple analysis of the LAT spectrum and light curve for these three bursts to show that the data are consistent with the external forward shock model. This analysis consists of verifying whether the temporal decay index and the spectral index satisfy the relation expected for the ES emission (closure relation), and comparing the observed flux in the LAT band with the prediction of the ES model (according to this model the high energy flux is a function of blast wave energy, independent of the unknown circumstellar medium density, and extremely weakly

dependent on the energy fraction in magnetic fields).

We describe in Section 2.3 how the >100 MeV data alone can be used to theoretically estimate the emission at late times ($t \gtrsim$ a few hours) in the X-ray and optical bands within the framework of the external forward shock model, and that for these three bursts the expected flux according to the ES model is in agreement with the observed data in these bands.

Moreover, if we determine the ES parameters (ϵ_e, ϵ_B, n, and $E_{KE,iso}$)[1] using only the late time X-ray and optical fluxes (and radio data), we can predict the flux at >100 MeV at any time after the deceleration time for the GRB relativistic outflow. We show in Section 2.3 that this predicted flux at $> 10^2$ MeV is consistent with the value observed by the *Fermi* satellite for the bursts analyzed in this chapter.

These exercises and results show that the high energy emission is due to the external shock as discussed in Section 2.3. We also describe in Section 2.3 that the magnetic field in the shocked fluid — responsible for the generation of > 100 MeV photons as well as the late time X-ray and optical photons via the synchrotron mechanism — is consistent with the shock compression of a circumstellar magnetic field of a few tens of micro-Gauss.

It is important to point out that we do not consider in this chapter the prompt sub-MeV emission mechanism for GRBs — which is well-known to have a separate and distinct origin as evidenced by the very rapid decay of sub-MeV flux observed by *Swift* and *Fermi*/GBM (the flux in the sub-MeV band drops-off with time as $\sim t^{-3}$ or faster as opposed to the $\sim t^{-1}$ observed

---

[1] ϵ_e and ϵ_B are the energy fraction of the shocked fluid in electrons and magnetic field, respectively, n is the number density of protons in the burst circumstellar medium, and $E_{KE,iso}$ is the isotropic kinetic energy in the ES blast wave.

	β_{LAT}	p	z	d_{L28}	$t_{GRB}[s]$	$E_{\gamma,iso}[erg]$
GRB 080916C	1.20 ± 0.03	2.4 ± 0.06	4.3	12.3	60	8.8×10^{54}
GRB 090510	1.1 ± 0.1	2.2 ± 0.2	0.9	1.8	0.3	1.08×10^{53}
GRB 090902B	1.1 ± 0.1	2.2 ± 0.2	1.8	4.3	30	3.63×10^{54}

Table 2.1: The main quantities used in our analysis for these 3 GRBs. β_{LAT} is the spectral index for the > 100 MeV data, p is the power-law index for the energy distribution of injected electrons, that is, $dn/d\gamma \propto \gamma^{-p}$, z is the redshift, d_{L28} is the luminosity distance in units of 10^{28} cm, t_{GRB} is the approximate burst duration in the *Fermi*/GBM band and $E_{\gamma,iso}$ is the isotropic equivalent of energy observed in γ-rays in the 10 keV-10 GeV band for GRB 080916C and GRB 090902B, and in the 10 keV-30 GeV band for GRB 090510. Data taken from Abdo et al. (2009a,b,d), De Pasquale et al. (2010).

in the LAT band). Nor do we investigate the emission process for photons in the LAT band during the prompt burst phase, except for Section 2.4.

2.2 ES model and the >100 MeV emission from GRBs: Simple arguments

In this chapter we consider 3 GRBs detected by *Fermi*/LAT in the $> 10^2$ MeV band: GRB 080916C (Abdo et al. 2009a), GRB 090510 (Abdo et al. 2009b, De Pasquale et al. 2010) and GRB 090902B (Abdo et al. 2009d). These bursts show the "generic" features observed in the >100 MeV emission of most of *Fermi* GRBs mentioned above, and these are the only three bursts for which we have optical, X-ray and *Fermi* data available. Some basic information for these 3 GRBs have been summarized in Table 2.1.

The synchrotron process in the ES model predicts a relationship between the temporal decay index (α) of the light curve and the energy spectral index (β), which are called closure relations. These relations serve as a quick

check for whether or not the observed radiation is being produced in the external shock. In this chapter, we use the convention $f(\nu, t) \propto \nu^{-\beta} t^{-\alpha}$.

Since the *Fermi*/LAT band detects very high energy photons ($\gtrsim 10^2$ MeV), it is reasonable to assume that this band lies above all the synchrotron characteristic frequencies (assuming that the emission process is synchrotron). In this case the spectrum should be $\propto \nu^{-p/2}$ (Sari, Piran, Narayan 1998)— where p is the power law index of the injected electrons' energy distribution — and according to the external forward shock model (see, e.g., Panaitescu & Kumar 2000), the light curve should decay as $\propto t^{-(3p-2)/4}$, giving the following closure relation: $\alpha = (3\beta - 1)/2$. Using the data in Table 2.1 we find that all three bursts satisfy this closure relation (Table 2.2), which encourages us to continue our diagnosis of the >100 MeV emission in the context of the ES model.

We check next if the predicted magnitude of the synchrotron flux in the ES is consistent with the observed values. This calculation would seem very uncertain at first, but we note that the predicted external forward shock synchrotron flux at a frequency larger than all characteristic frequencies of the synchrotron emission is independent of the circumstellar medium (CSM) density, n, and it is extremely weakly dependent on the fraction of the energy of the shocked gas in the magnetic field, ϵ_B, which is a highly uncertain parameter for the ES model. The density falls off as $\propto R^{-s}$, where R is the distance from the center of the explosion, and $s = 0$ corresponds to a constant CSM and $s = 2$ corresponds to a CSM carved out by the progenitor star's wind. The flux is given by (see e.g. Kumar 2000, Panaitescu & Kumar 2000):

$$f_\nu = 0.2 \text{mJy} \, E_{55}^{\frac{p+2}{4}} \epsilon_e^{p-1} \epsilon_{B,-2}^{\frac{p-2}{4}} t_1^{-\frac{3p-2}{4}} \nu_8^{-\frac{p}{2}} (1+Y)^{-1} (1+z)^{\frac{p+2}{4}} d_{L28}^{-2}, \qquad (2.1)$$

	α_{ES}	α_{obs}	$t[s]$	$f_{100MeV}^{ES}{}^{a}$	f_{100MeV}^{obs}
GRB 080916C	1.30 ± 0.05	1.2 ± 0.2	150	> 16	67
GRB 090510	1.2 ± 0.2	1.38 ± 0.07	100	> 3	14
GRB 090902B	1.2 ± 0.2	~ 1.5	50	> 100	220

[a]Fluxes in this table are in nJy. The fluxes are calculated using equation (2.1), the data in Table 2.1, and setting the isotropic kinetic energy in the ES to be $E_{KE,iso} = E_{\gamma,iso}$, which gives a lower limit on $E_{KE,iso}$; most likely $E_{KE,iso} = $ few $\times E_{\gamma,iso}$ and we find that using $E_{KE,iso} \sim 3 \times E_{\gamma,iso}$ the fluxes match the observed values very well. Also, for this calculation, $\epsilon_B = 10^{-5}$, $\epsilon_e = 0.25$, $p = 2.4$ and $Y < 1$.

Table 2.2: Comparison between the temporal decay index (α_{ES}) expected for the external forward shock model, and the observed decay index (α_{obs}); these values are equal to within 1–σ error bar. The ES flux calculated at time t is compared to the observed value at the same time. These two values are also consistent, further lending support to the ES origin of the > 100 MeV emission. Data are obtained from the same references as in Table 2.1. The theoretically calculated flux would be larger if $\epsilon_e > 0.25$; GRB afterglow data for 8 well studied bursts suggest that $0.2 < \epsilon_e \lesssim 0.8$ (Panaitescu & Kumar 2001).

where ϵ_e is the fraction of energy of the shocked gas in electrons, $t_1 = t/10s$ is the time since the beginning of the explosion in the observer frame (in units of 10s), ν_8 is photon energy in units of 100MeV, $E_{55} \equiv E_{KE,iso}/10^{55}$erg is the scaled isotropic kinetic energy in the ES, Y is the Compton-Y parameter, z is the redshift and d_{L28} is the luminosity distance to the burst (in units of 10^{28} cm). Using the values of Table 2.1, we can predict the expected flux at 100 MeV from the ES and compare it to the observed value at the same time. We show in Table 2.2 that the observed high energy flux is consistent with the theoretically expected values for all three busts.

The fact that these bursts satisfy the closure relation, and that the observed $> 10^2$ MeV flux is consistent with theoretical expectations, suggests that the high energy emission detected by *Fermi*/LAT from GRBs is produced

19

via synchrotron emission in the ES. In the next section we carry out a more detailed analysis that includes all the available data from these bursts during the "afterglow" phase, that is, after the emission in the sub-MeV band has ended (or fallen below *Fermi*/GBM threshold).

2.3 Detailed synthesis of all available data and the external forward shock model

The simple arguments presented in the last section provide tantalizing evidence that the high energy photons from the three bursts considered in this chapter are synchrotron photons produced in the external forward shock. We present a more detailed analysis in this section where we consider all available data for the three bursts after the end of the emission in the *Fermi*/GBM band, that is, for $t > t_{GRB}$, where t_{GRB} is the "burst duration" provided in Table 2.1. The data we consider consist of $> 10^2$ MeV emission observed by *Fermi*/LAT and AGILE/GRID, X-ray data from *Swift*/XRT, optical data from *Swift*/UVOT and various ground based observatories, and radio data from Westerbork in the case of GRB 090902B.

The *main idea* is to use the $> 10^2$ MeV data to constrain the ES parameters (ϵ_e, ϵ_B, n and $E_{KE,iso}$)[2] — which as we shall see allow for a large hyper-surface in this space — and for each of the points in the allowed 4-D parameter space calculate the flux in the X-ray, optical and radio bands from the external forward shock at those times where data in one of these bands are available for comparison with the observed value. It would be tempting

---

[2]In addition to these four parameters, the ES model also has an extra two, which are s and p. However, these last two can be estimated fairly directly by looking at the spectrum and temporal decay indices of the light curves at different wavelengths.

to think that such an exercise cannot be very illuminating as the ES flux calculated at any given time in these bands would have a large uncertainly that would reflect the large volume of the sub-space of 4-D parameter space allowed by the $>10^2$ MeV data alone. This, however, turns out to be incorrect – the afterglow flux generated by the ES in the X-ray and optical bands (before the time of jet break) is almost uniquely determined from the high-energy photon flux; the entire sub-space of the 4-D space, allowed by the $>10^2$ MeV data, projects to an extremely small region (almost to a point) as far as the emission at any frequency larger than $\sim \nu_i$ is concerned; ν_i is the synchrotron frequency corresponding to the minimum energy of injected electrons (electrons just behind the shock front), which we also refer to as synchrotron injection frequency. Therefore, we can compare the ES model predictions of flux in the X-ray and optical bands with the observed data, and either rule out the ES origin for high energy photons or confirm it[3].

We also carry out this exercise in the *reverse direction*, that is, find the sub-space of 4-D parameter space allowed by the late time ($t \gtrsim 1$ d) X-ray, optical, and radio data, and then calculate the expected $>10^2$ MeV flux at early times for this allowed subspace for comparison with the observed *Fermi*/LAT data. This *reverse direction* exercise is not equivalent to the one described in the preceding paragraph since the 4-D sub-space allowed by the $>10^2$ MeV data and that by the late time X-ray and optical data are in general quite different (of course they have common points whenever early high-energy and late low energy emissions arise from the same ES).

---

[3]It should be pointed out that the X-ray afterglow light curves of long-GRBs are rather complicated during the first few hours (see e.g. Nousek et al. 2006, O'Brien et al. 2006) and the ES model in its simplest form can't explain these features, however the behavior becomes simpler and consistent with ES origin after about 1/2 day.

The input physics in all of these calculations consist of the following main ingredients: synchrotron frequency and flux (see Rybicki & Lightman 1979 for detailed formulae; a convenient summary of the relevant equations can also be found in Kumar & Narayan 2009), Blanford-McKee self-similar solution for the ES (Blandford & McKee 1976), electron cooling due to synchrotron and synchrotron self-Compton radiation (Klein-Nishina reduction to the cross-section is very important to incorporate for all the three bursts for at least a fraction of the 4-D parameter space), and the emergent synchrotron spectrum as described in e.g. Sari, Piran & Narayan (1998). Although the calculations we present in the following sections can be carried out analytically (e.g. Kumar & McMahon 2008), it is somewhat tedious, and so we have coded all the relevant physics in a program and use that for finding the allowed part of 4-D parameter space and for comparing the results of theoretical calculation with the observed data. Numerical codes have also the advantage that they enable us to make fewer assumptions and approximations. Nevertheless, we present a few analytical estimates to give the reader a flavor of the calculations involved.

We analyze the data for each of the three bursts individually in the following three sub-sections in reverse chronological order.

2.3.1 GRB 090902B

The *Fermi*/LAT and GBM observations of this burst can be found in Abdo et al. (2009d). The X-ray data for this GRB started at about half a day after the trigger time. The spectrum in the 0.3–10 keV X-ray band was found to be $\beta_x = 0.9 \pm 0.1$, and the light curve decayed as $\alpha_x = 1.30 \pm 0.04$ (Pandey et al. 2010). The optical observations by *Swift*/UVOT started at the same time (Swenson & Stratta 2009) and show $\alpha_{opt} \sim 1.2$. ROTSE also detected

22

the optical afterglow starting at ~ 1.4 hours and its decay is consistent with the UVOT decay (Pandey et al. 2009). The Faulkes Telescope North also observed the afterglow at about 21 hours after the burst using the R filter (Guidorzi et al. 2009). There is a radio detection available at about 1.3 days after the burst and its flux is ~ 111 μJy at 4.8 GHz (van der Host et al. 2009).

The late time afterglow data obtained by *Swift*/XRT show that the X-ray band, 0.3–10 keV (ν_x), should lie between ν_i (the synchrotron injection frequency) and ν_c (the synchrotron frequency corresponding to the electrons' energy for which the radiative loss time-scale equals the dynamical time; we also refer to it as synchrotron cooling frequency). This is because $\nu_x > \nu_i$, otherwise the light curve would be rising with time instead of the observed decline. Moreover, if $\nu_c < \nu_x$, then $p = 2\beta_x \sim 1.8 \pm 0.2$, and in that case $f_{\nu_x}(t) \propto t^{-(3p+10)/16} = t^{-0.96 \pm 0.04}$, and that is inconsistent with the observed decline of the X-ray light curve (for decay indices for values of $p < 2$ see the table 1 in Zhang & Mészáros (2004)). Thus, $\nu_i < \nu_x < \nu_c$, so that $\beta_x = (p-1)/2$ or $p \sim 2.8 \pm 0.2$.

Next we determine if the X-ray data are consistent with a constant density circumstellar medium or a wind-like medium. For $s = 0$ ($s = 2$) the expected temporal decay index of the X-ray light curve is $\alpha = 3(p-1)/4 = 1.35 \pm 0.15$ ($\alpha = (3p-1)/4 = 1.85 \pm 0.15$). Thus, a constant density circumstellar medium is favored for this GRB.

The XRT flux at 1 keV at $t = 12.5$ h was reported to be 0.4 μJy (Pandey et al. 2010). Extrapolating this flux to the optical band using the observed values of α_x and β_x we find the flux at 21 h to be within a factor ~ 3 of the ~ 15 μJy flux reported by Guidorzi et al. (2009). Thus, the emissions in the optical and the X-ray bands arise in the same source (ES) with ν_i below

23

the optical band; also, if the optical band were below ν_i, then the optical light curve would be increasing with time, which is not observed. Moreover, the optical and X-ray data together provide a more accurate determination of the spectral index to be 0.69 ± 0.06 or $p = 2.38 \pm 0.12$ which is consistent with the p-value for the high-energy data at $t > t_{GRB}$ (see Table 2.1).

If the $>10^2$ MeV emission is produced in the external forward shock then we should be able to show that the early high energy γ-ray flux is consistent with the late time X-ray and optical data. We first show this approximately using analytical calculations, and then present results obtained by a more accurate numerical calculation in our figures.

The observed flux at 100 MeV and $t = 50$ s can be extrapolated to half a day to estimate the flux at 1 keV. This requires the knowledge of where ν_c lies at this time. It can be shown that $\nu_c \sim 100$ MeV at 50 s in order that the flux at 100 keV does not exceed the observed flux limit (see subsection below). Therefore, $\nu_c \propto t^{-1/2}$ is ~ 3 MeV at 12.5 h, and thus the expected flux at 1 keV is ~ 0.5 μJy which agrees with the observed value. Therefore, we can conclude that the > 100 MeV, X-ray and optical photons were all produced by the same source, and we suggest that this source must be the external forward shock as already determined for the X-ray and optical data.

We now determine the ES parameter space for this burst. We can determine this space using both the forward direction and reverse direction approaches. We first list the constraints on the ES model, then give a few analytical estimates using the equations in, for example, Panaitescu & Kumar (2002), and then present the results of our detail numerical calculations.

2.3.1.1 Forward direction

In this subsection we only use the early high-energy emission to constrain the ES parameter space. The constraints at $t = 50$ s are: (i) The flux at 100 MeV should agree with the observed value (see Table 2.2) - within the error bar of 10%, (ii) $\nu_c < 100$ MeV at 50 s for consistency with the observed spectrum, (iii) the flux at 100 keV should be smaller than 0.04 mJy (which is a factor of 10 less than the observed value), so that ES emission does not prevent the *Fermi*/GBM light curve to decay steeply after 25 seconds, and (iv) $Y < 50$ so that the energy going into the second Inverse Compton is not excessive.

The first 3 conditions give the following 3 equations at $t = 50$ s. The cooling frequency is given by (Panaitescu & Kumar 2002)

$$\nu_c \sim 6\text{eV} \, E_{55}^{-1/2} n^{-1} \epsilon_{B,-2}^{-3/2} (1+Y)^{-2} < 100\text{MeV} \,. \tag{2.2}$$

The flux at 100 keV, which is between ν_i and ν_c as discussed above, is (Panaitescu & Kumar 2002)

$$f_{100keV} \sim 53\text{mJy} \, E_{55}^{1.35} n^{0.5} \epsilon_{B,-2}^{0.85} \epsilon_{e,-1}^{1.4} < 0.04\text{mJy} \,. \tag{2.3}$$

And lastly, using (2.1), the flux at 100 MeV, which we assume is above ν_c, is

$$f_{100MeV} \sim 1 \times 10^{-4}\text{mJy} \, E_{55}^{1.1} \epsilon_{B,-2}^{0.1} \epsilon_{e,-1}^{1.4} = 220\text{nJy} \,. \tag{2.4}$$

Solving for n from (2.3) and for ϵ_e from (2.4), and substituting in (2.2), we find that at 50 s $\nu_c \gtrsim 50$ MeV. The injection frequency can also be estimated at $t = 50$ s, it is given by

$$\nu_i \sim 8\text{keV}\, E_{55}^{1/2}\epsilon_{B,-2}^{1/2}\epsilon_{e,-1}^2, \tag{2.5}$$

and using (2.4), one finds $\nu_i \sim 25\text{keV}\, E_{55}^{-1.07}\epsilon_{B,-2}^{0.36}$, which gives $\nu_i \sim 2$ keV for $\epsilon_B \sim 10^{-5}$. These values of ν_i and ν_c are consistent with the values obtained with detail numerical calculations and reported in the Fig. 1 caption.

Using (2.2), we can find a lower limit on ϵ_B, which is given by

$$\epsilon_B \gtrsim \frac{1 \times 10^{-7}}{n^{2/3}E_{55}^{1/3}(1+Y)^{4/3}}. \tag{2.6}$$

Also, we can solve for ϵ_e using (2.4) and substitute that into (2.3) to obtain an upper limit on ϵ_B, which is

$$\epsilon_B \lesssim \frac{3 \times 10^{-7}}{n^{2/3}E_{55}^{1/3}(1+Y)^{4/3}}. \tag{2.7}$$

Note that these estimates are consistent with the numerical results we present in Fig. 1. We also find the $\epsilon_B \propto n^{-2/3}$ dependence that is shown in the figure.

Moreover, with these parameters we can predict the fluxes at late times. The X-ray and optical band lie between ν_i and ν_c at ~ 1 day (see above). The first X-ray data point is at 12.5 h, and the theoretically expected flux at 1 keV at this time is given by

$$f_{1keV} \sim 1\text{mJy}\, E_{55}^{1.35}n^{0.5}\epsilon_{B,-2}^{0.85}\epsilon_{e,-1}^{1.4}, \tag{2.8}$$

and the optical flux at $\sim 7.5 \times 10^4$ s is

$$f_{2eV} \sim 47\text{mJy}\, E_{55}^{1.35}n^{0.5}\epsilon_{B,-2}^{0.85}\epsilon_{e,-1}^{1.4}. \tag{2.9}$$

26

We can use (2.3) to find an upper limit for the X-ray and optical fluxes. In addition, we can find ϵ_e using (2.4), and use (2.6) to find a lower limit for these fluxes. We find that

$$0.5\mu\text{Jy} \lesssim f_{1keV} \lesssim 0.8\mu\text{Jy} \qquad (2.10)$$

for the X-ray flux at 12.5 h, and

$$25\mu\text{Jy} \lesssim f_{2eV} \lesssim 36\mu\text{Jy} \qquad (2.11)$$

for the optical flux at $\sim 7.5 \times 10^4$ s. These estimates agree very well with the observed values of 0.4 μJy (Pandey et al. 2010) and 15 μJy (Guidorzi et al. 2009) at the respective bands and times. We note that, although Inverse Compton cooling is very important at late times, the X-ray band lies below ν_c and therefore X-ray and optical fluxes are unaffected by Inverse Compton cooling.

Next, we present the results obtained by detailed numerical calculations. We use the same constraints described at the beginning of this subsection to determine the parameter space allowed by the high-energy early data. It is worth noting that in our numerical calculations throughout the chapter we make no assumption regarding the ordering of the characteristic frequencies, nor the location of the observed bands with respect to them. The projection of the sub-space of the 4-D parameter space allowed by the high energy data onto the ϵ_B–n plane is shown in Figure 2.1, and some of the other ES parameters are presented in the Fig. 1 caption. It is clear that there is a large sub-space that is consistent with the LAT data, and also that the magnetic field needed for the synchrotron source is consistent with the shock-compressed magnetic

field in the CSM of strength $\lesssim 30\ \mu$G. For each point in the 4-D space allowed by the $>10^2$ MeV data we calculate the X-ray and the optical flux at late times. In spite of the fact that the 4-D sub-space allowed by the LAT data is very large (Fig. 2.1) the expected X-ray and optical flux at late times lie in a narrow range as shown by two diagonal bands in Figure 2.2; the width of these bands has been artificially increased by a factor 2 to reflect the approximate treatment of the radial structure of the blast wave and also to include in the calculation the effect of the blast wave spherical curvature on the ES emission (see, e.g., Appendix A of Panaitescu & Kumar 2000; both of these effects together contribute roughly a factor of 2). We see that the observed X-ray and optical light curves lie within the theoretically calculated bands (Fig. 2.2). This result strongly supports the ES model for the origin of the $>10^2$ MeV photons.

We note that the above mentioned extrapolation from early time, high-energy, data to late time, low-energy, flux prediction was carried out for a CSM with $s = 0$. We have also carried out the same calculation but by assuming a wind medium ($s = 2$), and in this case we find that the expected flux at late times is smaller than the observed values by a factor of 20 or more; this conclusion is drawn by comparing the late optical and X-ray fluxes predicted at a single time with the observations at that same time, that is, without making use of the temporal decay indices observed in these bands. We pointed out above that the late time afterglow data for this burst are consistent with a uniform density medium, but not with a $s = 2$ medium. Thus, there is a good agreement between the late time afterglow data and the early $>10^2$ MeV data in regards to the property of the CSM; the two methods explore the CSM density at different radii.
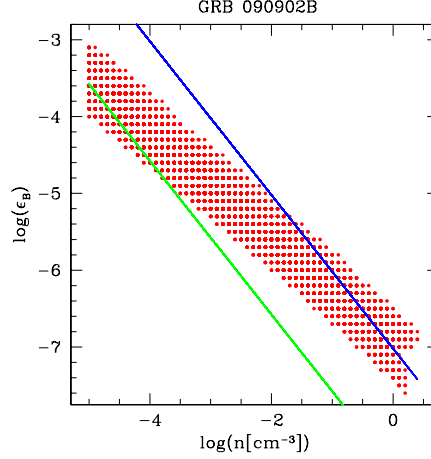
GRB 090902B

Figure 2.1: We determine the sub-space of the 4-D parameter space (for the forward external forward shock model with $s = 0$) allowed by the high energy data for GRB 090902B at t=50 s as described in Section 2.3.1. The projection of the allowed subspace onto the ϵ_B–n plane is shown in this figure (dots); the discrete points reflect the numerical resolution of our calculation. We also plot the expected ϵ_B for a shock compressed CSM magnetic field of 5 and 30 μG as the green and blue lines respectively; for a CSM field of strength B_0, the value of ϵ_B downstream of the shock-front resulting from the shock compressed CSM field is $\approx B_0^2/(2\pi n m_p c^2)$, where $n m_p$ is the CSM mass density, and c is the speed of light. Note that no magnetic field amplification is needed, other than shock compression of a CSM magnetic field of $\sim$ 30 μG, to produce the >100 MeV photons. The synchrotron injection and cooling frequencies at $t = 50$ s for the sub-space of 4-D parameter space allowed by the high energy data are 100 eV $\lesssim \nu_i \lesssim 3$ keV and 30 MeV $\lesssim \nu_c \lesssim 100$ MeV respectively, the Lorentz factor of the blast wave at $t = 50$ s lies between 330 and 1500, and 10^{55} erg $\lesssim E_{KE,iso} \lesssim 3 \times 10^{55}$ erg. Note that at 0.5 d ν_i would be below the optical band, and $\nu_c > 1$ MeV, and these values are consistent with the X-ray spectrum and the X-ray and optical decay indices at this time.

Figure 2.2: The optical and X-ray fluxes of GRB 090902B predicted at late times using only the high energy data at 50 s (assuming synchrotron emission from external forward shock) are shown in the right half of this figure, and the predicted flux values are compared with the observed data (discrete points with error bars). The width of the region between the green (magenta) lines indicates the uncertainty in the theoretically predicted X-ray (optical) fluxes (the width is set by the error in the measurement of 100 MeV flux at 50 s, and the error in the calculation of external forward shock flux due to approximations made – both these contribute roughly equally to the uncertainty in the predicted flux at late times). LAT (X-ray) data red (black) circles, are from Abdo et al. 2009d (Evans et al. 2007, 2009) and were converted to flux density at 100 MeV (1 keV) using the average spectral index provided in the text. Optical fluxes are from Swenson et al. 2009 (square) and Guidorzi et al. 2009 (triangle) and were converted to flux density using 16.4 mag $\approx$ 1 mJy. The blue dashed line shows schematically the light curve observed by *Fermi*/GBM. The predicted value for the radio flux at one day has a very large range (not shown), but consistent with the observed value.

2.3.1.2 Reverse direction

We carry out the above mentioned exercise in the reverse direction as well, that is, we determine the ES parameter space using only the late time X-ray, optical and radio data, and use these parameters to determine the flux at 10^2 MeV at early times when *Fermi*/LAT observations were made. The constraints on ES model parameters at late times are the following: (i) The X-ray and optical flux at 12.5 h and 7.5×10^4 s, respectively, should match the ES flux at these bands and at these times, (ii) the radio flux at 1.3 d should be consistent with the observed value. We first show some analytical estimates and then turn to more detailed numerical calculations.

Constraint (i) is simply equation (2.8) set equal to the observed value of 0.4 μJy at 12.5 h. For the analytical estimates presented here, it is not necessary to use the optical flux at late times, since both the optical and X-ray bands lie between ν_i and ν_c, so they provide identical constraints. Constraint (ii), assuming that the radio frequency is below ν_i, gives

$$f_{4.8GHz} \sim 19\text{mJy } E_{55}^{5/6} n^{1/2} \epsilon_{B,-2}^{1/3} \epsilon_{e,-1}^{-2/3} = 111\mu\text{Jy} . \tag{2.12}$$

Solving for ϵ_e in the last equation and substituting in constraint (i) gives an equation for ϵ_B, which is

$$\epsilon_B = \frac{6 \times 10^{-8}}{n E_{55}^2}. \tag{2.13}$$

This estimate is consistent with the numerical result presented on Fig. 2.3. Moreover, one can see that we find $\epsilon_B \propto n^{-1}$, which is exactly what is found numerically (and agrees very well with the shock-compressed CSM field prediction).
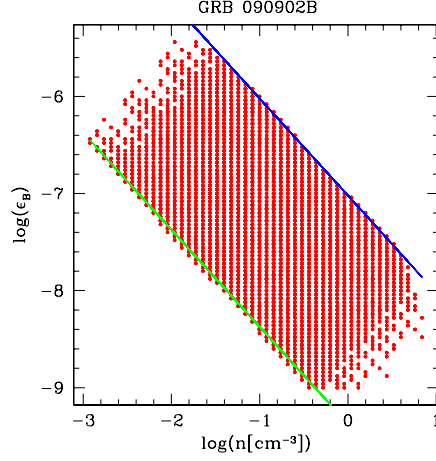
Figure 2.3: We determine the sub-space of the 4-D parameter space (for the external forward shock model with $s = 0$) allowed by the late time ($t > 0.5$ d) X-ray, optical and radio data for GRB 090902B as described in Section 2.3.1.2. The projection of the allowed subspace onto the ϵ_B–n plane at $t = 0.5$ d is shown in this figure (dots). We also plot the expected ϵ_B for a shock compressed CSM magnetic field of 2 and 30 μG as the green and blue lines, respectively; for a CSM field of strength B_0, the value of ϵ_B downstream of the shock-front resulting from the shock compressed CSM field is $\approx B_0^2/(2\pi n m_p c^2)$, where $n m_p$ is the CSM mass density, and c is the speed of light. Note that no magnetic field amplification is needed, other than shock compression of a CSM magnetic field of strength $\lesssim 30$ μG, to produce the late time X-ray, optical and radio data. We arrived at this same conclusion from the modeling of early time >100 MeV radiation alone (see Fig. 2.1).

We can now predict the high-energy flux at 100 MeV and early time using the ES parameters determined using late time afterglow data in X-ray and radio bands. We use (2.1) at $t = 50$ s, substituting ϵ_e from (2.12) and n from (2.13), and find that the flux should be

$$f_{100MeV} \sim 200 \text{nJy } E_{55}^{3/4} \epsilon_{B,-5}^{-1/4}, \tag{2.14}$$

in agreement with the observed value at $t = 50$ s. We now turn to our numerical results.

Using the same set of constraints presented at the beginning of this subsection, we perform our numerical calculations to determine the ES parameter space allowed by the late time ($t \gtrsim 0.5$ d) X-ray, optical and radio data and use that information to "predict" the 100 MeV flux at early times ($t \lesssim 10^3$ s). The numerical results of this exercise, for a $s = 0$ CSM medium, are also in good agreement with the $Fermi$/LAT data as shown in Figure 2.4. Moreover, the flux from the ES at $t = 50$ s and 100 keV is found to be much smaller than the flux observed by $Fermi$/GBM (Fig. 2.4 - left panel), which is very reassuring, because otherwise this would be in serious conflict with the steep decline of the light curve observed in the sub-MeV band; this also shows that the sub-MeV and GeV radiations are produced by two different sources.

We note that the range of values for ϵ_B allowed by the late time radio, optical and X-ray afterglow data is entirely consistent with shock compressed circumstellar medium magnetic field of strength < 30 μG (see Fig. 2.3). We also point out that the afterglow flux depends on the magnetic field B, and $B^2 \propto \epsilon_B n$, therefore, there is a degeneracy between ϵ_B and n and that makes it very difficult to determine n uniquely.

33
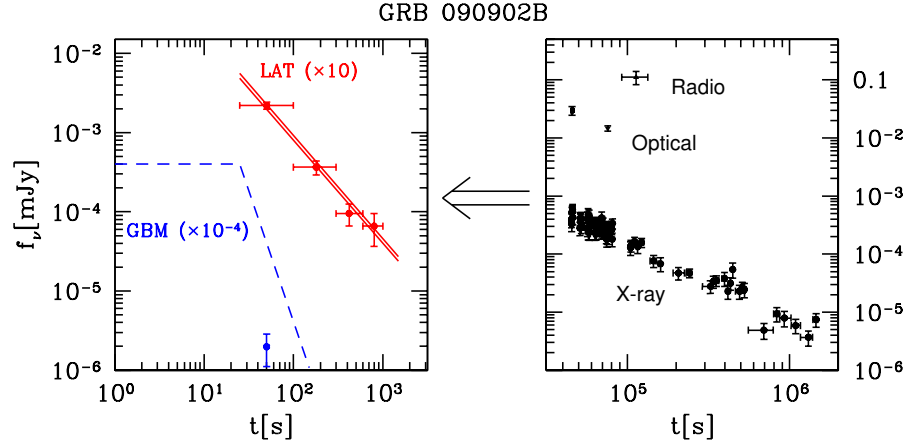
Figure 2.4: Using the X-ray, optical and radio data of GRB 090902B at late times (right panel) we constrain the external forward shock parameters, and then use these parameters to predict the 100 MeV flux at early times (left panel). The region between the red lines shows the range for the predicted flux at 100 MeV; note the remarkably narrow range for the predicted 100 MeV flux in spite of the large spread to the allowed ES parameters as shown in Fig. 2.3. The blue point (left panel) indicates the flux at 100 keV and 50 s that we expect from the ES model; note that the ES flux at 100 keV falls well below the observed *Fermi*/GBM flux shown schematically by the dashed line in the left panel, and that is why the GBM light curve undergoes a rapid decline with time ($\sim t^{-3}$) at the end of the prompt burst phase. The radio flux is taken from van der Host et al. (2009). All other data are the same as in Fig. 2.2.

2.3.2 GRB 090510

The *Fermi*/LAT and GBM observations of this burst are described in Abdo et al. (2009b) and De Pasquale et al. (2010). This short burst has very early X-ray and optical data starting only 100 s after the burst. The X-ray spectrum is $\beta_x = 0.57 \pm 0.08$ (Grupe & Hoverstein 2009). The temporal decay index is $\alpha_{x,1} = 0.74 \pm 0.03$ during the initial $\sim 10^3$ s and subsequently the decay steepens to $\alpha_{x,2} = 2.18 \pm 0.10$ with a break at $t_x = 1.43^{+0.09}_{-0.15}$ ks. The optical data shows $\alpha_{opt,1} = -0.5^{+0.11}_{-0.13}$ and $\alpha_{opt,2} = 1.13^{+0.11}_{-0.10}$ with a break at $t_{opt} = 1.58^{+0.46}_{-0.37}$ ks (De Pasquale et al. 2010).

In the context of the ES model (also considered by Gao et al. 2009, Ghirlanda, Ghisellini, Nava 2010 and De Pasquale et al. 2010 for the case of this specific burst), the data suggests that $\nu_x < \nu_c$, because in this case $\beta_x = (p-1)/2$, so $p = 2.14 \pm 0.16$ and the temporal decay index (for $s = 0$) is $\alpha_x = 3(p-1)/4 = 0.86 \pm 0.12$ consistent with the observed value of $\alpha_{x,1}$. If we take $\nu_x > \nu_c$, then $\beta_x = p/2$, so $p = 1.14 \pm 0.16$ and the temporal decay index should have been $\alpha_x = (3p+10)/16 = 0.84 \pm 0.03$, since $p < 2$, which is consistent with the observed temporal decay, however, the expected optical light curve index for this value of p is $\alpha_{opt} = -(p+2)/(8p-8) = -2.8$, which is inconsistent with the observed value of $\alpha_{opt,1}$ (see next paragraph). The X-ray afterglow data also shows that the medium in the vicinity of the burst must have been of constant density. This is because, for an $s = 2$ medium, the expected temporal decay of the X-ray flux, when $\nu_x < \nu_c$, is $\propto t^{-(3p-1)/4} = t^{-1.36}$ – much steeper than the observed decline of $t^{-0.74}$ – while for $s = 0$ the expected decline is consistent with observations (Gao et al. 2009).

Given the fact that the break in the optical light curve and that in the X-ray light curve occur at the same time, that is, $t_x = t_{opt}$, it is unlikely that

35

the emission in these two bands comes from two different, unrelated sources. Thus, it is natural to attribute both the optical and X-ray emissions to the external forward shock. The fact that the optical light curve is rising during the first ~ 0.5 h as $t^{1/2}$ means that $\nu_{opt} < \nu_i$ during this time period (Panaitescu & Kumar 2000), where ν_{opt} is the optical band. The break seen in both light curves can be attributed to the jet break. The X-ray light curve decay of $t^{-2.2}$ for $t > 1.4 \times 10^3$ s agrees very well with the expected post-jet-break light curve of $\propto t^{-p} = t^{-2.12\pm0.14}$ (Rhoads 1999), and suggests a jet opening angle of $\sim 1^o$ (Sari, Piran & Halpern, 1999). The reason that $\alpha_{opt,2}$ is not as steep can be understood the following way. At the time of the jet break, the optical band is below ν_i, therefore, the light curve decays as $\propto t^{-1/3}$ instead of $\propto t^{-p}$ (Rhoads 1999). At later times, when ν_i, which is decreasing rapidly, crosses the optical band, the optical light curve will transition slowly from $\propto t^{-1/3}$ to $\propto t^{-p}$, and that is why $\alpha_{opt,2}$ is not as large as $\alpha_{x,2}$; the timescale for this transition can be long/short depending on how far above γ_i the asymptotic distribution of $n(\gamma) \propto \gamma^{-p}$ is attained. This interpretation is supported by the results of our numerical calculation shown in Figure 2.5 — we obtain a value of $\nu_i \sim 500$ eV at 100 s, which should cross the optical band at ~ 4000 s - a factor of ~ 3 larger than the observed time of the jet break. This idea can be tested with optical data available at much later times: it should show the light curve slowly steepening to the asymptotic value of $\propto t^{-p}$. Moreover, the optical spectrum before the break in the light curve ($t < t_{opt}$) should be consistent with $\nu^{1/3}$.

Is it possible that the rise of the optical band light curve might be due to the onset of the ES, while the initial X-ray emission (until the break at ~ 1.4 ks) and the gamma-ray photons are from the "internal shock" mechanism (De

36
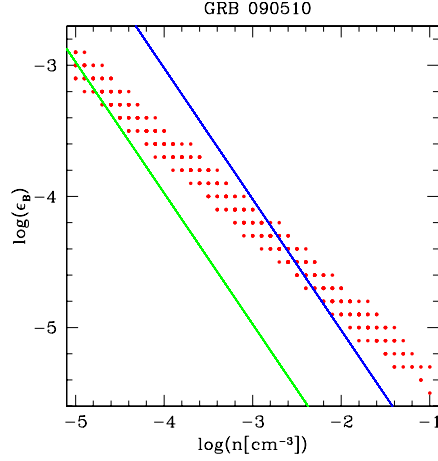
Figure 2.5: Using the observational constraints mentioned in the text (Section 2.3.2), we determine the sub-space of 4-D parameter space (for the external forward shock with $s = 0$) allowed by the data for GRB 090510 at $t = 50$ s. We show the projection of the allowed subspace onto the ϵ_B–n plane in this figure (dots); the region agrees with the expected ϵ_B from shock-compressed CSM magnetic field of $\lesssim 30$ μG (the green and blue lines show 10 μG and 30 μG, respectively). The other parameters for the ES solution at this time are: The Lorentz factor of the blast wave is between 260 and 970, $0.1 < \epsilon_e < 0.7$ and 10^{53} erg $\lesssim E_{KE,iso} \lesssim 4 \times 10^{53}$ erg. At $t = 100$ s, we also find $Y < 4$, $\nu_i \sim 500$ eV, $\nu_c \sim 40$ MeV.

Pasquale et al. 2010)? This seems unlikely, given that the density of the CSM required for the deceleration time of the GRB jet to be $\sim 10^3$s (t_{opt}) is extremely low, as can be seen from the following equation

$$n = \frac{3E_{KE,iso}(1+z)^3}{32\pi c^5 m_p \Gamma^8 t_{peak}^3}, \tag{2.15}$$

where m_p is the mass of the proton, c is the speed of light, Γ is the initial Lorentz factor of the GRB jet, t_{peak} is the time when the peak of the light curve is observed and $E_{KE,iso}$ is the isotropic energy in the ES. For GRB 090510, Γ was determined to be $\Gamma \gtrsim 10^3$ by using $\gamma\gamma$ opacity arguments (Abdo et al. 2009b), which is a limit applicable to the scenario proposed by De Pasquale et al. (2010), where MeV and GeV photons are produced in the same source. We take $t_{peak} \sim 10^3 s$ and $E_{KE,iso} \sim E_{\gamma,iso}$ ($E_{53} \equiv E_{KE,iso}/10^{53}$erg) and find that we need a CSM density of $n \approx 10^{-9} E_{53} \Gamma_3^{-8} t_{peak,3}^{-3} cm^{-3}$, which is much smaller than the mean density of the Universe at this redshift, and therefore unphysical. Even though there is a strong dependence of CSM density on Γ, the upper limit on density provided above cannot be increased by more than a factor of ~ 10, since the error in the determination of Γ is much less than a factor of 2 (Abdo et al. 2009b). Thus, the possibility that the peak of the optical light curve at $\sim 10^3$ s is due to the deceleration of the GRB jet seems very unlikely. We note that in the scenario we present in this chapter, the > 100 MeV emission observed by *Fermi*/LAT and the lower energy ($\lesssim 1$ MeV) observed by *Fermi*/GBM are produced by two different sources, therefore, the pair-production argument can't be used to constrain Γ. However, in this scenario, the deceleration time for the GRB jet is $\lesssim 1$ s, and that means that the peak of the optical light curve at $\sim 10^3$ s cannot correspond to the deceleration time.

We conclude that the available data suggest that optical and X-ray photons are coming from the same source (ES model). We now consider whether the observed >100 MeV emission is also consistent with the ES model. We first use the observed data to show that >100 MeV, X-ray and optical data are produced by the ES, then we provide some analytical estimates of the ES model parameters and later show the results of our detailed numerical results in the figures.

AGILE/GRID reported a photon count in the 30 MeV–30 GeV band of 1.5×10^{-3} cm^{-2} s^{-1} at 10s, and the light curve was reported to decline as $t^{-1.3 \pm 0.15}$ (Giuliani et al. 2010). Therefore, the photon flux at 100s in this band is estimated to be $\sim 7.5 \times 10^{-5}$ cm^{-2} s^{-1} (Ghirlanda, Ghisellini, Nava, 2010; have also reported a single power-law decline of flux in the *Fermi* LAT band from ~ 1 s to 200 s). The *Swift*/XRT reported a photon flux of 0.07 cm^{-2} s^{-1} in the 0.3–10 keV band at 100 s. Using the spectrum reported in the *Swift*/XRT band (Grupe & Hoverstein 2009) — which is entirely consistent with the spectrum found in the AGILE/GRID band (Giuliani et al. 2010) — to extrapolate the observed photon count in the XRT band to the GRID band we find the expected photon flux at 100 s in the 30 MeV–30 GeV band of 7.9×10^{-5} cm^{-2} s^{-1}, and that is consistent with the flux observed by AGILE.

The peak of the optical light curve was observed at ~ 1000 s with a value of ~ 100 μJy, and the X-ray flux at 1000 s and ~ 4 keV was 2.2 μJy (De Pasquale et al. 2010). Since we attribute the optical light curve peak with the crossing of ν_i through the optical band, then the peak of the optical light curve determines the synchrotron flux at the peak of the spectrum. Therefore, using the X-ray flux at 1000 s and the X-ray spectrum we can extrapolate back to optical band (2 eV) and we find a flux of 170 μJy, which is consistent, within a

factor of better than 2, with the observed optical value at this time. Therefore, we can conclude that >100 MeV, X-ray and optical emissions are all produced by the same source, and that source must be the external forward shock as that is known to produce long lasting radiation in the X-ray and optical bands with a well known closure relation between α and β that is observed in GRB 090510 in all energy bands.

Using the data in the LAT, XRT and optical bands we can determine the ES parameters for GRB 090510. The following observational constraints must be satisfied by the allowed ES parameters: (i) The flux at 100 MeV and 100 s should be equal to the observed value (Table 2.2), (ii) $\nu_c < 100$ MeV at 100 s, (iii) the X-ray flux at 1000 s and ~ 4 keV should be equal to the observed value of 2.2 μJy (De Pasquale et al. 2010), and (iv) the flux at the peak of synchrotron spectrum should be ~ 100 μJy (De Pasquale et al. 2010). This last constraint arises because the optical flux peaks when ν_i passes the optical band, and therefore the peak synchrotron flux should be equal to the measured peak optical flux; it should be noted that the peak synchrotron flux for $s = 0$ according to the ES model does not change with time as long as the shock front moves at a relativistic speed.

We present some analytical estimates for the ES parameters before showing our detailed numerical results. The ES flux at 100 MeV and $t = 100$ s, assuming that 100 MeV is above ν_c is given by (2.1) and is

$$f_{100MeV} \sim 2.4 \times 10^{-6} \text{mJy } E_{53}^{1.1} \epsilon_{B,-2}^{0.1} \epsilon_{e,-1}^{1.4} = 14 \text{nJy} , \qquad (2.16)$$

which is constraint (i). The flux at 4 keV and 1000 s, assuming that it is between ν_i and ν_c is given by

$$f_{4keV} \sim 3\text{mJy } E_{53}^{1.35} n^{0.5} \epsilon_{B,-2}^{0.85} \epsilon_{e,-1}^{1.4} = 2.2\mu\text{Jy} ,\qquad(2.17)$$

which is constraint (iii). And lastly, constraint (iv) is that the peak synchrotron flux should equal the flux at the peak of the optical light curve, i.e.,

$$f_p \sim 12\text{mJy } E_{53} n^{1/2} \epsilon_{B,-2}^{1/2} = 100\mu\text{Jy} .\qquad(2.18)$$

Just as was done for GRB 090902B, constraint (ii) gives a lower limit on ϵ_B, which in the case for this GRB is not too useful. Instead, we can solve ϵ_e from (2.16) and substitute it in (2.17), which gives

$$\epsilon_B = \frac{1 \times 10^{-6}}{E_{53}^{1/3} n^{2/3} (1+Y)^{4/3}},\qquad(2.19)$$

consistent with the numerical calculation presented in Fig. 2.5. Also, with this last expression and using (2.18) we find that the CSM density for this GRB is

$$n \sim 0.3\text{cm}^{-3} \, (1+Y)^4 E_{53}^{-5},\qquad(2.20)$$

which is also consistent with the fact that we only find numerical solutions with CSM densities lower than $\sim$0.1 cm^{-3}.

For the ES parameters of this burst, the cooling frequency at 100 s can be estimated to be

$$\nu_c \sim 76\text{eV } E_{53}^{-1/2} n^{-1} \epsilon_{B,-2}^{-3/2} (1+Y)^{-2},\qquad(2.21)$$

and substituting n from (2.18) gives $\nu_c \sim 1\text{MeV } E_{53}^{3/2} \epsilon_{B,-2}^{-1/2} (1+Y)^{-2}$. Thus, for $\epsilon_B \sim 10^{-5}$ we find $\nu_c \sim 30$ MeV. The injection frequency at 100 s is given by

$$\nu_i \sim 240\text{eV } E_{53}^{1/2}\epsilon_{B,-2}^{1/2}\epsilon_{e,-1}^2, \tag{2.22}$$

and substituting ϵ_e from (2.16) one finds $\nu_i \sim 250\text{eV } E_{53}^{-1.07}\epsilon_{B,-5}^{0.36}$. These values of ν_i and ν_c are consistent with the values obtained with detailed numerical calculations and reported in the Fig. 2.5 caption.

The detailed numerical results of the parameter search can be found in Figure 2.5; the sub-space of the 4-D parameter space allowed by the data for GRB 090510 is projected on the 2-D ϵ_B–n plane, which is a very convenient way of looking at the allowed sub-space. Note that all the available data for GRB 090510 can be fitted by the ES model and that the value of n allowed by the data is less than 0.1 cm^{-3}, which is in keeping with the low density expected in the neighborhood of short bursts. Moreover, ϵ_B for the entire allowed part of the 4-D sub-space is small, and its magnitude is consistent with what one would expect for the CSM magnetic field of strength $\lesssim 30$ μG that is shock compressed by the blast wave (Fig. 2.5). The ES shock model provides a consistent fit to the data from optical to $>10^2$ MeV bands as can be clearly seen in Figure 2.6. The ES parameters found for this GRB can be found in the Fig. 2.5 caption.

2.3.3 GRB 080916C

The *Fermi*/LAT and GBM observations for GRB 0809016C have been presented in Abdo et al. (2009a). For this burst, the optical and X-ray observations started about 1d after the burst and both bands are consistent with $f_\nu(t) \propto \nu^{-0.5\pm0.3}t^{-1.3\pm0.1}$ (Greiner et al. 2009).

The fact that the optical light curve is decaying as $t^{-1.3}$ means that ν_i is below the optical band at 1 day, because if ν_i is above the optical band,
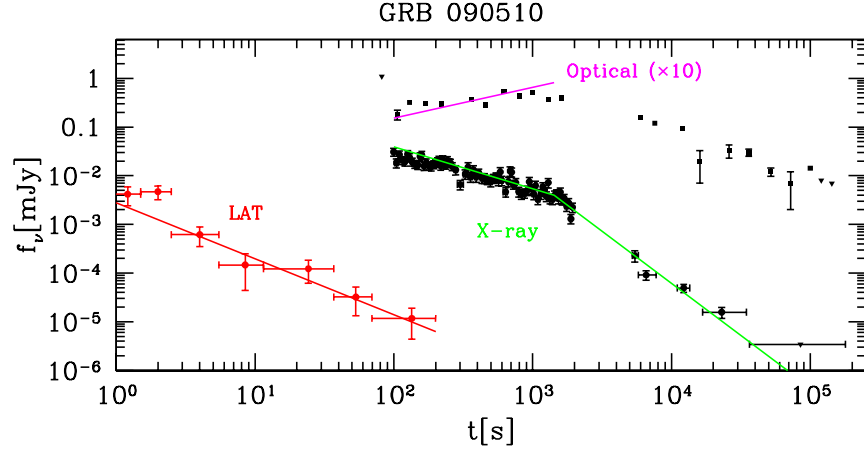
Figure 2.6: Shown in this figure are data for GRB 090510 obtained by *Fermi*/LAT (>100 MeV), *Swift*/XRT (X-ray) and *Swift*/UVOT (optical) data, and a fit to all these data by the external forward shock model (solid lines). The jet break seen in X-ray has been modeled with a power-law, $\propto t^{-p}$; the optical light curve after the jet break should show a shallower decay $\propto t^{-1/3}$, because at this time $\nu_{opt} < \nu_i$, but then it slowly evolves to an asymptotic decay $\propto t^{-p}$ at later times (Rhoads 1999). The LAT (X-ray) data are from De Pasquale et al. 2009 (Evans et al. 2007, 2009) and have been converted to flux density at 100 MeV (1 keV) using the average spectral index mentioned in the text (Section 2.3.2). The optical data (squares) are from De Pasquale et al. (2010). Triangles mark upper limits in the X-ray and optical light curves.

then the light curve should be rising as $\propto t^{1/2}$ (as in the case of GRB 090510). Moreover, the shallow spectral index in the *Swift*/XRT band ($\beta_x < 1$) suggests that $\nu_c > 10$ keV at 1 d. The X-ray and optical data together yield a spectral index of 0.65 ± 0.03, and therefore $p = 2.3 \pm 0.06$ which is consistent with the *Fermi*/LAT spectrum (see Table 2.1). The value of p can be used to calculate the time dependence of the light curve, and that is found to be $t^{-0.98}$ ($t^{-1.48\pm0.05}$) for $s = 0$ ($s = 2$) CSM. Thus, $s = 2$ CSM is preferred by the late time optical and X-ray afterglow data (Kumar & Barniol Duran 2009; Gao et al. 2009; Zou, Fan & Piran 2009).

Using the early >100 MeV data only, we determine the ES model parameters. With these parameters, we can then predict the X-ray and optical fluxes at late times, that is, the forward direction approach. The constraints that should be satisfied are: (i) The ES flux at 100 MeV and 150 s should match the observed value (Table 2.2), (ii) $\nu_c < 100$ MeV to be consistent with the observed spectrum, and (iii) the ES flux at 150 s should be smaller than the observed value to allow the 100 keV flux to decay rapidly as observed. These constraints are the same as the ones presented for the case of GRB 090902B and the analytical approach is the same as the one presented on Section 2.3.1, therefore, we omit the details here. The ES parameters obtained numerically can be found in fig. 2 of Kumar & Barniol Duran (2009). With these parameters the X-ray and optical flux at late times can be calculated, and we find these in excellent agreement with the observations (Figure 2.7).

It is important to note here that this extrapolation from high-energy early time data to low energy, late time, flux prediction was carried out for a circumstellar medium with $s \sim 2$. We have also carried out the same calculation but for a uniform density medium ($s = 0$), and in this case the
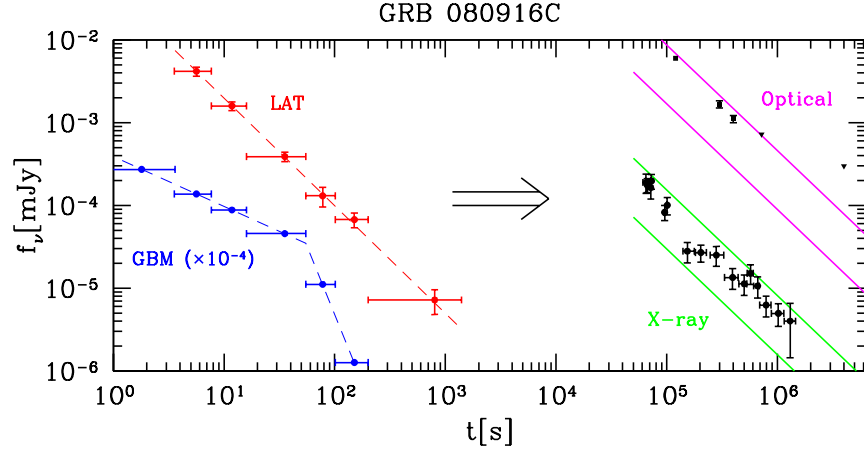
Figure 2.7: The optical and X-ray fluxes of GRB 080916C predicted at late times using only the high energy data at 150 s (assuming synchrotron emission from external forward shock) are shown in the right half of this figure, and the predicted flux values are compared with the observed data (discrete points with error bars). The width of the region between the green (magenta) lines indicates the uncertainty in the theoretically calculated X-ray (optical) fluxes. The LAT (Abdo et al. 2009a) and X-ray fluxes (Evans et al. 2007, 2009) at 100 MeV and 1 keV, respectively, have been converted to mJy the same way as done for Figure 2.2. Optical fluxes (squares) are from Greiner et al. 2009 (triangles are upper limits). GBM flux at 100 keV – blue filled circles – is taken from Abdo et al. 2009a. The thin dashed lines connecting LAT and GBM data are only to guide the eye.

theoretically calculated flux at late times is larger than the observed values by a factor of ~ 5 or more; the factor of 5 discrepancy is much larger than error in the flux calculation. We pointed out above that the late time afterglow data for this burst are consistent with a $s = 2$ medium but not $s = 0$ medium. Thus, there is a nice agreement between the late time afterglow data and the early $> 10^2$ MeV data — which explore very different radii — in regards to the density stratification of the CSM.

We have carried out the exercise in the "reverse direction" as well. Using only the late X-ray and optical data, we determine the ES parameters. The observational constraints that need to be satisfied are: (i) The ES flux at X-ray and optical energies at 1 d should match the observed values, (ii) we should have the ordering $\nu_i < \nu_{opt} < \nu_X < \nu_c$ to be consistent with the observed spectrum, (iii) the ES flux at 150 s should be smaller than the observed value to allow the 100 keV flux to decay rapidly as observed, and (iv) the Lorentz Factor of the ejecta should be $\gtrsim 60$ at 1 d, since we do not want Γ to be too small at the beginning of the burst, because this would contradict estimates done at early times (Greiner et al. 2009). Since the analytical approach is very similar to the one for GRB 090902B, we omit it here – the only difference is that it must be done for a wind-like medium, since the data of this GRB prefers it. The ES parameters can be found numerically and with these parameters we predict the > 100 MeV flux at early times. This predicted flux agrees with the *Fermi*/LAT observations as shown in Figure 2.8.

2.4   The Band function fit at early times

Does it require a coincidence for the superposition of two different spectra, that originated in two separate sources, to have the shape of a Band func-
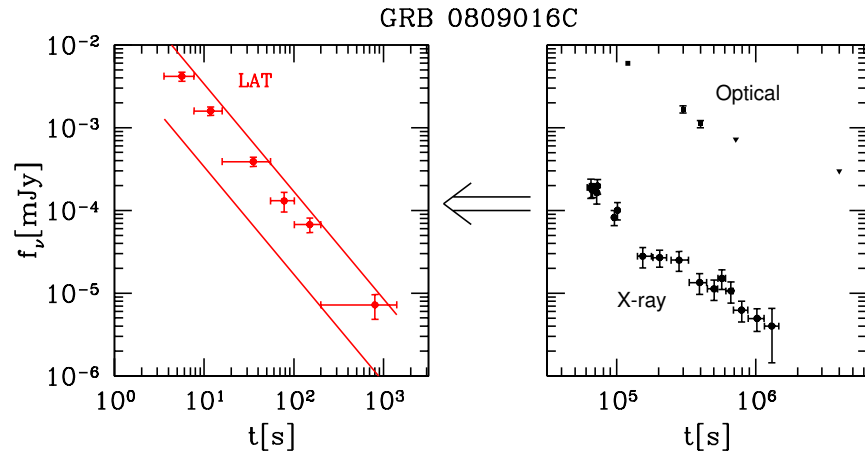
Figure 2.8: Using the X-ray and optical data of GRB 080916C at late times (right panel) we constrain the external forward shock parameters, and then use these parameters to predict the 100 MeV flux at early times (left panel). The region between the red lines shows the range for the predicted flux at 100 MeV. The data are the same as in Figure 2.7.

tion? It turns out that no fine tuning or coincidence is needed because the spectral peaks, and the flux at the peak, for ES radiation is closely tied to the GRB jet luminosity which also regulates the sub-MeV emission; for GRB 080916C, a very broad range of values for ϵ_B and n the peak of νf_ν for the external shock emission, at the deceleration time of 4 s, lies between $\sim$1 MeV and 10^2 MeV. Figure 2.9 shows an example of a superposition of external shock spectrum and the sub-MeV source, and the result of a Band function fit to it.

2.5 Discussion and Conclusion

The *Fermi* Satellite has detected 18 GRBs with >100 MeV emission so far. In this chapter we have analyzed the >100 MeV emission of three of them: two long-GRBs (090902B and 080916C) and one short burst (GRB 090510), and find that the data for all three bursts are consistent with synchrotron emission in the external forward shock. This idea was initially proposed in our previous work on GRB 080916C (Kumar & Barniol Duran 2009), shortly after the publication of this burst's data by Abdo et al. (2009a). Now, there are three GRBs for which high energy data has been published, and for all of them we have presented here multiple lines of evidence that >100 MeV photons, subsequent to the prompt GRB phase, were generated in the external forward shock. The reason that high energy photons are detected from only a small fraction of GRBs observed by *Fermi* is likely due to the fact that the high energy flux from the external forward shock has a strong dependence on the GRB jet Lorentz factor, and therefore very bright bursts with large Lorentz factors are the only ones detected by *Fermi*/LAT (Kumar & Barniol Duran 2009); there should be no difference in long and short bursts, as far as the >100 MeV emission is concerned - the high energy flux is only a function of
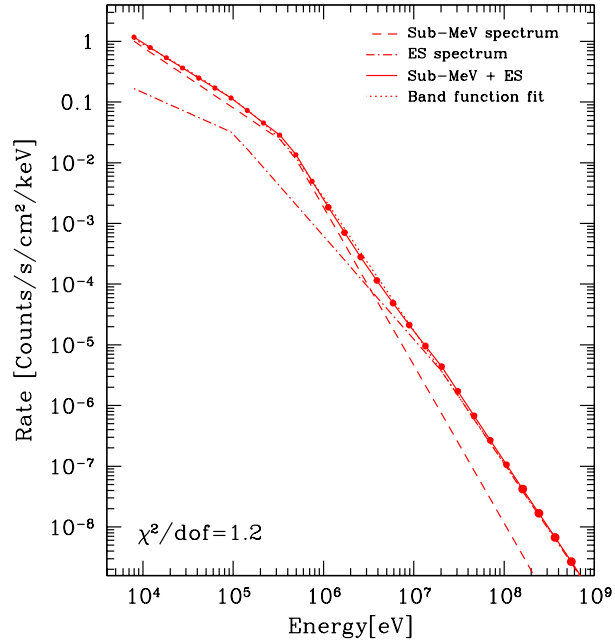
Figure 2.9: GRB 080916C: Band function fit to a superposition of external shock (ES) spectrum (shown as a dot-dash line) and the sub-MeV source spectrum (dashed line). The superposed spectrum is shown by a solid line, and the best fit Band function by a dotted line (χ^2/dof for the Band function fit is 1.2); errors in the Count Rate are taken from Abdo et al. (2009), and these are equal to the size of filled circles. The ES spectrum is a synchrotron spectrum in the slow cooling regime with break frequencies 100 keV and 20 MeV (values taken from the ES calculation). The Sub-MeV spectrum (dashed line) peaks at 400 keV and has a slope of ν^0 ($\nu^{-1.6}$) below (above) the peak; the choice of the high energy spectral index for this component is motivated by observations during the first 4 s of the burst, when the emission is dominated by the sub-MeV component. If one were to use different break frequencies for the ES spectrum (for instance, 100 keV and 70 MeV), the superposition would also give an acceptable Band function fit.

burst energy and time, see equation 2.1).

We have analyzed the data in 4 different ways, and all of them lead to the same conclusion regarding the origin of $>10^2$ MeV photons. First, we verified that the temporal decay index for the >100 MeV light curve and the spectral index are consistent with the closure relation expected for the synchrotron emission in the external forward shock. Second, we calculated the expected magnitude of the synchrotron flux at 100 MeV according to the external forward shock model and find that to be consistent with the observed value. Third, using the >100 MeV data only, we determined the external shock parameters, and from these parameters we predict the X-ray and optical fluxes at late times and find that these predicted fluxes are consistent with the observed values within the uncertainty of our calculations, that is, a factor of two (see Figs. 2.2, 2.7). And lastly, using the late time X-ray, optical and radio fluxes — which the GRB community has believed for a long time to be produced in the external forward shock — we determine the external shock parameters, and using these parameters we predict the expected >100 MeV flux at early times and find the flux to be in agreement with the observed value (see Figs. 2.4, 2.8). The fact that the >100 MeV emission and the lower energy ($\lesssim 1$ MeV) emission are produced by two different sources at two different locations suggests that we should be cautious when using the highest observed photon energy and pair-production arguments to determine the Lorentz factor of the GRB jet.

We point out that the external shocks for these bursts were nearly adiabatic, that is, radiative losses are small. The evidence for this comes from two different observations: (1) the late time X-ray spectrum lies in the adiabatic regime; (2) a radiative shock at early times (close to the deceleration time)

would produce emission in the 10–10^2 keV band far in excess of the observed limits. We find that radiative shock is not needed to explain the temporal decay index of the >100 MeV light curve as suggested by Ghisellini, Ghirlanda, Nava (2010), provided that the observing band is above all synchrotron characteristic frequencies.

We find that the magnetic field required in the external forward shock for the observed high and low energy emissions for these three bursts is consistent with shock-compressed magnetic field in the CSM; the magnetic field in the CSM – before shock compression – should be on the order of a few tens of micro-Gauss (see figs. 2.1, 2.3 and 2.5). For these three bursts, at least, no magnetic dynamo is needed to operate behind the shock front to amplify the magnetic field.

The data for the short burst (GRB 090510) are consistent with the medium in the vicinity of the burst (within ~ 1 pc) being uniform and with density less than 0.1 cm^{-3}; the data rules out a CSM where $n \propto R^{-2}$. On the other hand, the data for one of the two long *Fermi* bursts (GRB 080916C) prefers a wind like medium and the other (GRB 090902B) a uniform density medium; these conclusions are reached independently from late time afterglow data alone and from the early time high energy data projected to late time using the 4-D parameter space technique described in Section 2.3.

It is also interesting to note that the power-law index of the energy distribution of injected electrons (p) in the shocked fluid, for all the three *Fermi* bursts analyzed in this work, is 2.4 to within the error of measurement, suggesting an agreement with the *Fermi* acceleration of particles in highly relativistic shocks, e.g. Achterberg et al. (2001); a unique power-law index for electrons' distribution in highly relativistic shocks is not found in all simu-

lations. The study of high energy emission close to the deceleration time of GRB jets is likely to shed light on the onset of collisionless shocks and particle acceleration process.

It might seem surprising that we are able to fit all data (optical, X-ray, $\gtrsim 10^2$ MeV) for these three *Fermi* bursts with just a few parameters for the external forward shock. This is in sharp contrast to *Swift* bursts which often display a variety of puzzling (poorly understood) features in their afterglow light curves. There are two reasons that these *Fermi* bursts can be understood using a very simple model (external forward shock). (1) The data for the two long *Fermi* bursts (080916C and 090902B) are not available during the first 1/2 day, and that is precisely the time frame when complicated features (plateau, etc., e.g. Nousek et al. 2006, O'Brien et al. 2006) are seen in the X-ray afterglow light curves of *Swift* bursts (we note that the external forward shock model in its simplest form can't explain these features) — however, the afterglow data at later times is almost invariably a smooth single (or double) power-law function that can be modeled by synchrotron emission from an external forward shock. (2) For very energetic GRBs — the three bursts we have analyzed in this chapter are among the most energetic bursts in their class — the progenitor star is likely to be completely destroyed leaving behind very little material to fall back onto the compact remnant at the center to fuel continued activity and give rise to complex features during the first few hours of the X-ray afterglow light curve (Kumar, Narayan & Johnson 2008). To summarize, the GRB afterglow physics was simple in the decade preceding the launch of *Swift*, and then things became quite complicated, and now the *Fermi* data might be helping to clear the fog and reveal the underlying simplicity once again.

Chapter 3

Implications of electron acceleration for high-energy radiation from gamma-ray bursts

3.1 Introduction

The >100 MeV LAT (Large Area Telescope) emission from GRBs detected by the *Fermi* Satellite can be described as follows. The first 100 MeV photons arrive $\sim$ 1 s (in the host galaxy frame) after the trigger time, for long GRBs; the trigger time is the time when low energy photons ($\sim$ 1 MeV) are first detected by the GBM (Gamma-ray Burst Monitor onboard *Fermi*). The 100 MeV light curve rises fast until it peaks and then it decays as a single power-law for a long duration of time (of order 10^3 s) – much longer than the duration of the lower energy photons detected by GBM – until it falls below the detector's sensitivity. Radiation above 100 MeV from GRBs has been suggested to be produced via the synchrotron mechanism in the external forward shock (Kumar & Barniol Duran 2009, 2010); the external forward shock scenario was first proposed by Rees & Mészáros (1992), Mészáros & Rees (1993), Paczyński & Rhoads (1993), and since then it has been used widely, see, e.g., Mészáros & Rees (1997), Sari, Piran, Narayan (1998), Dermer & Mitman (1999), for a comprehensive review see, e.g., Piran (2004) and references therein. After our initial suggestion, many groups have also considered and provided evidence for this origin of the >100 MeV radiation (Gao et al. 2009; Corsi, Guetta, Piro 2010; De Pasquale et al. 2010; Ghirlanda, Ghisellini,

Nava 2010; Ghisellini, Ghirlanda, Nava 2010). The magnetic field required for this model is consistent with being produced via shock-compressed seed magnetic field in the CSM (circumstellar medium) of strength of a few tens of micro-Gauss. The peak of the 100 MeV light curve can be attributed to the deceleration time which is the time it takes for the GRB-jet to transfer about half of its energy to the external medium.

We investigate in this chapter whether electrons in the external forward shock can be accelerated to sufficiently high Lorentz factors, even for a small CSM magnetic field of a few tens of μG, so that the synchrotron radiation can extend to ~ 10 GeV as seen by *Fermi*/LAT for a number of GRBs. We study the electrons acceleration in the context of diffusive shock acceleration (e.g., Krymskii 1977, Axford, Leer & Skadron 1978, Bell 1978, Blandford & Ostriker 1978, Blandford & Eichler 1987), which was developed for non-relativistic shocks and has now been developed to consider relativistic shocks (semi-) analytically (e.g. Gallant & Achterberg 1999, Achterberg et al. 2001) and recently using 2-D particle-in-cell simulations (e.g. Spitkovsky 2008a,b, Keshet et al. 2009). We assume that the electrons acceleration proceeds in the Bohm diffusion limit and that the magnetic field downstream is simply shock-compressed upstream magnetic field (other possibilities are considered in, e.g., Milosavljević & Nakar 2006, Sironi & Goodman 2007, Goodman & MacFadyen 2008, Couch, Milosavljević, Nakar 2008).

If the downstream magnetic field is simply the shock-compressed large-scale upstream field, then the field component perpendicular to the shock normal is amplified, while the parallel component is not. In this case, the downstream magnetic field will be mainly pointing to the direction perpendicular to the shock front normal, therefore particles trying to cross the shock

front from downstream to upstream will find it difficult to catch up with the shock front, which moves with a speed of $\sim c/3$ with respect to the downstream medium (see, e.g., Achterberg et al. 2001, Lemoine, Pelletier & Revenu 2006, Pelletier, Lemoine & Marcowith 2009). One way that the particles might return to the upstream is if there is efficient cross-field diffusion of particles, which might occur if turbulent magnetic field is produced downstream (Jokipii 1987, Achterberg & Ball 1994, Achterberg et al. 2001). In principle, the turbulent magnetic field could dominate the shock-compressed field throughout the downstream region. However, it seems that although some turbulence is present just downstream of the shock front it does not persist across the entire downstream region (see recent simulations by Sironi & Spitkovsky 2011 that show that magnetic field is amplified only right behind the shock front and returns to the shock-compressed value far downstream). In this case, much of the radiation is produced by particles swept downstream where the turbulence has died out and the magnetic field is consistent with the shock-compressed value. We also note that as long as the thickness of the turbulent magnetic field layer is smaller than the thickness of the shocked fluid divided by $(B_t/B_d)^2$ then the energy loss in the turbulent layer is small; B_t is the turbulent magnetic field strength and B_d is the shock-compressed magnetic field. Therefore, in this work we neglect energy loss in the turbulent magnetic field layer since it persists for a very short distance compared to the thickness of the shocked fluid (see, e.g., Keshet et al. 2009 and references therein).

This chapter is organized as follows. In Section 3.2 we address the question of high-energy electron confinement upstream and downstream of the shock front, and also radiative losses suffered by electrons in between acceleration. Also, in Section 3.2, we discuss the lag of the >100 MeV light curves

observed by *Fermi* LAT for several GRBs in light of our results on electron acceleration. In Section 3.3, we calculate the rise of the external forward shock light curve, taking into consideration the non-zero time to accelerate electrons to high enough energies so they can radiate at >100 MeV. We present our conclusions in Section 3.4.

3.2 Electron acceleration for >100 MeV emission

3.2.1 Electron confinement

It is widely believed that electrons in non-relativistic shocks undergo diffusive shock acceleration. (e.g., Krymskii 1977, Axford et al. 1978, Bell 1978, Blandford & Ostriker 1978, Blandford & Eichler 1987). In the context of relativistic shocks, it has been shown that electrons gain energy each time they cross the shock front by a factor of ~ 2, except on the first crossing when they gain energy by a factor of the Lorentz Factor (LF) of the shock front (Achterberg et al. 2001).

In order for electrons to turnaround while up/down stream and cross the shock front, their Larmor radius should be smaller than the size of the system, that is, electrons should be confined to the system in order to be accelerated. In this subsection, we explore the confinement of electrons in the external forward shock model when the magnetic field in the unshocked medium, upstream of the shock front, is a few tens of μG in strength, and the magnetic field in the shocked medium, downstream of the shock front, is simply the shock-compressed upstream field.

The highest photon energy detected for *Fermi* GRBs is on the order of 10 GeV. We first calculate the random LF in the downstream co-moving frame, γ_e, of electrons radiating 10 GeV photons via synchrotron radiation,

because these electrons have the largest Larmor radius and thus give us stricter confinement requirements. The synchrotron frequency in observer frame is $\nu_{syn} = eB_d\gamma_e^2\Gamma/2\pi m_e c(1+z)$, where Γ is the bulk LF of the shocked fluid measured in the upstream rest frame (lab frame), B_d is the magnetic field downstream (measured in the local rest frame), z is the redshift, m_e and e are the electron's mass and charge, respectively, and c is the speed of light (Rybicki & Lightman 1979). We convert the synchrotron frequency to 10 GeV, that is, $\nu_{10} = h\nu_{syn}/1.6 \times 10^{-2}$ erg, where h is the Planck constant and 10 GeV corresponds to 1.6×10^{-2} erg. Using the convention $Q_x = Q/10^x$ and solving the last expression for γ_e yields

$$\gamma_e = 1.5 \times 10^8 \nu_{10}^{1/2}(1+z)^{1/2}\Gamma_3^{-1}B_{u,-5}^{-1/2}, \tag{3.1}$$

where B_u is the magnetic field upstream, which is the magnetic field in the CSM. To obtain (3.1) we have assumed that the magnetic field in the downstream region is $B_d = 4\Gamma B_u$ (Gallant & Achterberg 1999, Achterberg et al. 2001; note that the shock front LF measured in the lab frame is $\Gamma_s = \sqrt{2}\Gamma$, Blandford & McKee 1976), that is, B_d is the shock-compressed magnetic field in the upstream (lab frame), which is what we have found for *Fermi* GRBs (Kumar & Barniol Duran 2009, 2010).

The electrons' LF in the rest frame of the upstream plasma is $\gamma_e\Gamma$, therefore, the Larmor radius in the upstream is given by

$$R_{L,u} = \frac{m_e c^2 \gamma_e \Gamma}{eB_u} = (2.6 \times 10^{19}\text{cm})\,\nu_{10}^{1/2}(1+z)^{1/2}B_{u,-5}^{-3/2}, \tag{3.2}$$

where we made use of (3.1) to eliminate γ_e. Comparing the Larmor radius with the size of the system upstream, R, which is given by the blast wave radius in the host galaxy rest frame — $R = 2c\Gamma^2 t/(1+z) \sim 10^{17}$cm (where $t \sim$ a few

seconds and $\Gamma \sim 10^3$ is the blast wave Lorentz factor, e.g. Abdo et al. 2009a) — we find that $R_{L,u} \gg R$. This might suggest that electrons of $\gamma_e \sim 10^8$ are not confined to the system. However, an electron upstream of the shock front travels only a distance $\sim R_{L,u}/\Gamma$ before returning to the downstream, because by the time the angle between electrons' velocity vector and the normal to the shock front exceeds $\sim 1/\Gamma$, the shock front catches up with the electron and sweeps it back downstream (Achterberg et al. 2001). Therefore, for electron confinement upstream one should compare $R_{L,u}/\Gamma$ with R:

$$\frac{R_{L,u}}{\Gamma R} = 0.26 \frac{\nu_{10}^{1/2}(1+z)^{1/2}}{\Gamma_3 B_{u,-5}^{3/2} R_{17}} = 1.1 \frac{\nu_{10}^{1/2} t_3^{1/8}(1+z)^{3/8}}{B_{u,-5}^{3/2}(E_{54}/n_0)^{3/8}}, \qquad (3.3)$$

where E is the isotropic kinetic energy in the blast wave, t is the time since the burst trigger in observer frame, and n is the number density of particles in the CSM; in deriving the second equality we made use of the time dependence of Γ and R in the external forward shock scenario for a homogeneous CSM (Sari, Piran, Narayan 1998). For $B_{u,-5} \approx 4$ found for the *Fermi* bursts, $R_{L,u}/(\Gamma R) \lesssim 0.2$, and, thus, electrons radiating at 10 GeV cannot escape from the upstream side of the shock front; note that this conclusion holds for at least several hours in the observer frame.

One should also check for electron confinement downstream. Here, the Larmor radius is smaller than it is upstream, because the magnetic field is larger by at least a factor of 4Γ due to shock compression. Therefore, the requirement for the confinement of electrons downstream is automatically satisfied whenever it is satisfied upstream.

We conclude that there is no problem confining external forward shock electrons that radiate $\sim$10 GeV synchrotron photons by the CSM magnetic field of strength $\gtrsim 10 \ \mu$G.

3.2.2 Radiative losses during electron acceleration

Electrons suffer radiative losses while being accelerated that could prevent them from reaching LFs of $\sim 10^8$ that are needed for radiating photons of 10 GeV via the synchrotron process. In this section, we ascertain whether or not the radiative losses suffered by electrons – due to synchrotron and inverse-Compton processes – are small compared with the energy gain in each round of crossing the shock front. We do this by comparing the total radiative cooling time-scale, t'_{cool}, which is the time-scale for electrons to lose half of their energy, with the acceleration time-scale.

For the case of ultra-relativistic shocks when the downstream magnetic field is simply the shock compressed upstream field, the upstream and downstream residency times for electrons are approximately equal, when particle diffusion is in the Bohm limit (Gallant & Achterberg 1999, Achterberg et al. 2001). Thus, the time it takes for electrons to make one complete cycle across the shock front is about twice the upstream residency time, and the upstream residency time is on the order of the gyro-time in the shock front co-moving frame (Baring 2004). In the lab frame, their upstream residency time is on the order of the time it takes them to travel a distance $\sim R_{L,u}/\Gamma$. Since the Larmor radius ($R_{L,u}$) increases with increasing electron energy, the last shock crossing dominates the total upstream residency time. Thus, the time, in the co-moving frame of the blast wave, that electrons spend during the last cycle of crossing the shock front (upstream $\rightarrow$ downstream $\rightarrow$ upstream) before getting accelerated to Lorentz factor γ_e – given by (3.1) –is:

$$t'_s \sim \frac{2R_{L,u}}{c\Gamma^2} = (1.7 \times 10^3 \text{s})\, \nu_{10}^{1/2}(1+z)^{1/2}\Gamma_3^{-2}B_{u,-5}^{-3/2}. \qquad (3.4)$$

Taking into account the energy loss that these electrons experience because of radiative cooling, the acceleration time-scale, in the blast wave co-moving frame, is given by

$$t'_{acc}(\gamma_e) \approx t'_{eq}(\gamma_e) + t'_s(\gamma_e), \qquad (3.5)$$

where $t'_{eq}(\gamma_e)$ is the elapsed time since the beginning of the explosion when $t'_s(\gamma_e) = t'_{cool}(\gamma_e)/2$ (shock front crossing time should be equal to at least half of the radiative cooling time in order to reach a particular γ_e). At t'_{eq} the electron barely reaches γ_e, therefore, it needs an extra time on the order of $\sim t'_s$ to fully reach the desired γ_e. If $t'_s > t'_{cool}/2$, then the radiative cooling is too strong and prevents the electron from reaching the desired γ_e. In the sub-sections below we discuss synchrotron and inverse-Compton losses and calculate the radiative cooling time.

3.2.2.1   Synchrotron losses

The synchrotron cooling time-scale (in the blast wave co-moving frame) in the upstream of the shock front is $t'_{syn,u} = 6\pi m_e c/\sigma_T B_u^2 \gamma_e \Gamma^2$, where σ_T is the Thomson scattering cross-section. We find that the synchrotron cooling time for an external froward shock electron with LF given by (3.1) is

$$t'_{syn,u} = (5.2 \times 10^4 \text{s}) \, \nu_{10}^{-1/2} (1+z)^{-1/2} \Gamma_3^{-1} B_{u,-5}^{-3/2}. \qquad (3.6)$$

Since $t'_{syn,u} > t'_s$ by a factor of 30, then synchrotron cooling in the upstream is unimportant for electrons radiating at 10 GeV.

Next, we calculate synchrotron losses in the downstream. Since $t'_{syn} \propto B^{-2}$, the synchrotron loss rate is larger downstream because of the larger magnetic field. For shock-compressed magnetic field downstream, B is larger

than upstream field by a factor 4 (in the blast wave co-moving frame), and therefore $t'_{syn,d} = t'_{syn,u}/16$. The effective synchrotron cooling time for electrons of LF given in (3.1) is $t'_{syn} \approx [1/2t'_{syn,d} + 1/2t'_{syn,u}]^{-1}$, which gives

$$t'_{syn} = (6.1 \times 10^3 \mathrm{s})\, \nu_{10}^{-1/2}(1+z)^{-1/2}\Gamma_3^{-1}B_{u,-5}^{-3/2}. \tag{3.7}$$

We see from (3.4) that $t'_{syn} \sim 4t'_s$ for electrons that produce synchrotron photons of 10 GeV energy, and therefore the maximum synchrotron photon energy — obtained by setting $t'_s = t'_{syn}$ — is $\nu_{max,syn} \sim 40\Gamma_3(1+z)^{-1}$ GeV (see, e.g., Guilbert, Fabian, Rees 1983, de Jager et al. 1996, Cheng & Wei 1996).

3.2.2.2 Inverse-Compton losses

In this sub-section we calculate the inverse-Compton (IC) cooling time-scale for electrons. The inverse-Compton cooling time depends on the energy density of photons, and on the electron LF. Electrons in the external forward shock region are exposed to photons from three different sources of radiation: (a) prompt $\sim$MeV γ-ray radiation which carries most of the energy released in GRBs; (b) synchrotron radiation produced in the external forward shock heated CSM and (c) radiation produced in the external reverse shock heated GRB-jet. We will consider all of these sources in our estimate for the IC cooling time. All calculations will be carried out in the rest frame of the shocked CSM.

The IC cooling time is given by

$$t'_{IC} = \frac{3m_e c^2}{4\int d\nu\, \sigma F'(\nu)\gamma_e}, \tag{3.8}$$

where $F'(\nu)$ is the energy flux in radiation per unit frequency in the co-moving frame of the shocked CSM, ν is photon frequency in observer frame, and σ

is the cross-section for interaction between electrons and photons; $\sigma \approx \sigma_T$ (Thomson cross-section) when $\nu < \Gamma m_e c^2/[(1+z)h\gamma_e] \equiv \nu_{kn}$, and for $\nu \gg \nu_{kn}$, $\sigma \approx \sigma_T(\nu/\nu_{kn})^{-1}$. Thus, an approximate equation for the IC cooling time is

$$ t'_{IC} \approx \frac{3m_e c^2}{4\sigma_T \gamma_e} \left[F'(< \nu_{kn}) + \frac{\nu_{kn}}{\nu_p} F'(> \nu_{kn}) \right]^{-1}, \tag{3.9}$$

where $F'(< \nu_{kn})$ is photon energy flux in the shock co-moving frame below the frequency ν_{kn} and $F'(> \nu_{kn})$ is the flux above ν_{kn}. The frequency at the peak of the $\nu F(\nu)$ spectrum is ν_p (in observer frame, that is, co-moving synchrotron peak frequency boosted by a factor of Γ and redshift corrected) and ν_{kn}, the Klein-Nishina frequency in the observer frame, for an electron of LF γ_e, is $h\nu_{kn} \approx (5\,\text{eV}) \, \Gamma_3 \gamma_{e,8}^{-1}(1+z)^{-1}$. We note that for $\nu_{kn} \gtrsim \nu_p$, only the first term in (3.9) should be kept.

The co-moving energy flux in radiation is related to the observed bolometric luminosity by:

$$ F'(\lesssim \nu_p) \sim \frac{L_{obs}}{4\pi R^2 \Gamma^2}. \tag{3.10}$$

Combining (3.9) and (3.10) we find

$$ t'_{IC} \sim \frac{3\pi R^2 \Gamma^2 m_e c^2}{\sigma_T L_{obs} \gamma_e} \left(\frac{\nu_{kn}}{\nu_p}\right)^{-1} \left[1 + \left(\frac{\nu_{kn}}{\nu_p}\right)^{\alpha} \right]^{-1}, \tag{3.11}$$

where α is the spectral index, that is, $F'(\nu) \propto \nu^{\alpha}$ for $\nu_{kn} < \nu < \nu_p$; for $\alpha > 0$ the term in the square bracket is of order unity. The above equation is valid only when $\nu_{kn} < \nu_p$.

As mentioned before, there are three different sources of photons that interact with electrons in the external forward shock. We analyze these cases separately.

Case (a): The prompt γ-ray emission in GRBs – the origin of which is still uncertain – often has a low energy spectral index $\alpha \sim 0$, and the spectrum peaks at $\nu_{p,6} \sim 1$. The luminosity of this component is the highest of the three cases considered; $L_{obs,52} \sim 10$ for *Fermi* GRBs that have $>10^2$ MeV emission. The cooling time, obtained from (3.11), for this case is

$$t'_{IC,a} = (2.2 \times 10^3 \text{s}) \frac{R_{17}^2 \Gamma_3 \nu_{p,6}(1+z)}{L_{obs,53}} \left[1 + \left(\frac{\nu_{kn}}{\nu_p}\right)^\alpha\right]^{-1} \qquad (3.12)$$

Case (b): The external forward shock synchrotron spectrum peaks at ~ 100 keV (before the deceleration time), and the spectral index between ν_{kn} and ν_p is $\alpha \sim 1/3$. The luminosity from the external forward shock is $L_{obs,52} \sim 0.1$ at the deceleration radius (R_d), and at smaller radius it decreases as $\sim R^3$. Therefore, we find from (3.11) that, for $R \leq R_d$,

$$t'_{IC,b} \approx (2.2 \times 10^4 \text{s}) R_{17}^{-1} \Gamma_3 \nu_{p,5} L_{obs,51}^{-1} R_{d,17}^3 (1+z). \qquad (3.13)$$

Case (c): If the GRB-jet is composed of protons and electrons, then the interaction of the jet with the CSM will heat up these particles by the reverse shock propagating into the cold jet, and the synchrotron radiation produced would be very effective at cooling electrons in the forward shock region. This is because the peak of the reverse shock emission at the deceleration time is typically at a few eV (Sari & Piran 1999a), which is of order ν_{kn} for electrons of $\gamma_e \sim 10^8$. Since $\nu_p \sim \nu_{kn}$, then we can keep only the first term in (3.9), and use (3.10) for flux in the calculation of the cooling time. The observed luminosity (at the deceleration time) is given by $L_{obs,d} \approx 4\pi d_L^2 \nu_{p,d} F_{p,d}$, where d_L is the luminosity distance, and $F_{p,d}$ and $\nu_{p,d}$ are the observed external reverse shock flux and peak energy at the deceleration time, respectively. Thus, the IC

cooling time-scale for electrons in the external forward shock region, due to the radiation produced in the reverse shock heated GRB-jet, is

$$t'_{IC,c} \approx (400\text{s})\, R_{d,17}^2 \Gamma_{d,3}^2 d_{L,28}^{-2} \gamma_{e,8}^{-1} \nu_{p,d}^{-1} F_{p,d}^{-1}, \tag{3.14}$$

where Γ_d is the LF of the GRB-jet at the deceleration time, $F_{p,d}$ is in Jansky (Jy) and $\nu_{p,d}$ in eV; the reverse peak flux can be ~ 1 Jy for very bright bursts such as GRB 990123 (Sari & Piran 1999b).

The total IC cooling time is

$$t'_{IC} = \left[\frac{1}{t'_{IC,a}} + \frac{1}{t'_{IC,b}} + \frac{1}{t'_{IC,c}} \right]^{-1} \tag{3.15}$$

and, finally, the total radiative cooling time, t'_{cool}, is given by

$$t'_{cool} = \left[\frac{1}{t'_{syn}} + \frac{1}{t'_{IC}} \right]^{-1}. \tag{3.16}$$

3.2.3 Application to *Fermi* GRBs

In this section, we analyze 3 GRBs detected by *Fermi*: GRB 080916C, 090510 and 090902B (Abdo et al. 2009a,c,d). The relevant data for each burst are tabulated in Table 3.1. We apply the above general results to these three GRBs, and determine the time it would take for electrons in the external forward shock for these bursts to be accelerated – via shock acceleration – to LFs capable of producing synchrotron photons of energies 100 MeV and 1 GeV (Table 3.2).

The external reverse shock emission depends on the highly uncertain magnetic field strength in the GRB-jet, and it is therefore difficult to estimate

GRB	α	$\nu_p[MeV]$	$B_{u,-5}$	$L^{prompt}_{obs,53}$	$L^{ES}_{obs,51}$
080916C	0	0.5	4	1.5	30
090510	0.4	2.8	2	3.6	1.6
090902B	0.4	0.7	2	1.2	1.7

Table 3.1: The main quantities used in our analysis for three *Fermi* GRBs. α is the approximate spectral energy index, during the prompt emission phase, below the peak of the spectrum ($f_\nu \propto \nu^\alpha$ for $\nu < \nu_p$), ν_p is the observed peak of the spectrum; $B_{u,-5}$ is the average upstream magnetic field, in units of 10 μG, obtained by modeling of the data for these bursts (Kumar & Barniol Duran 2010); $L^{prompt}_{obs,53}$ and $L^{ES}_{obs,51}$ are the approximate observed isotropic equivalent luminosities of the prompt γ-rays and external forward shock emission at the deceleration time, respectively. Data are taken from Abdo et al. (2009a,c,d). B_u was obtained by setting three simple constraints while modeling the external forward shock emission: 1. Its flux at 100 MeV should agree with the observed value, 2. Its cooling frequency should be below 100 MeV at early times for consistency with the observed spectrum, and 3. Its flux at 100 keV should be smaller than the observed value during the observed steep decay, so that the external forward shock emission does not prevent the 100 keV to decay steeply (Kumar & Barniol Duran 2009, 2010).

with any confidence. We calculate t'_{cool} by neglecting the contribution of reverse shock emission to inverse-Compton cooling of electrons ($t'_{IC,c}$), and this provides a lower bound to t'_{acc} which is reported in Table 3.2 as a fraction of the deceleration time, $t'_d = (1.7 \times 10^3 \text{s}) R_{d,17} \Gamma^{-1}_{d,3}$, for several *Fermi* bursts. We also provide in Table 3.2 an upper limit for the external reverse shock peak flux that is obtained by the condition that $t'_{cool} = t'_s$, at the deceleration time, when the contribution of the external reverse shock emission is included in the calculation of t'_{cool}.

GRB 080916C: The first >100 MeV photons arrived $\sim$ 3 s after the trigger time and then the 100 MeV light curve rose rapidly, as $\sim t^6$, and peaked at $\sim$ 5s (Abdo et al. 2009a). After the peak, which we identify as the deceleration time,

t_d, the flux decayed as a single power-law (this power-law is consistent with the expectation of the external forward shock model). So the first >100 MeV photons arrived at $t/t_d \sim 0.6$, and photons of energies $>$GeV were detected at ~ 7 s ($t/t_d \sim 1.4$). The highest energy photon, ~ 13 GeV, was detected ~ 16 s after the trigger time ($t/t_d \sim 3$).

For electrons to produce 100 MeV photons their LF should be $\sim 10^7$ for this burst, and for 1 GeV photons the required $\gamma_e > 3 \times 10^7$; we used $B_{u,-5} \sim 4$ as suggested by the data for this burst (Kumar & Barniol Duran 2009) – see Table 3.1. The acceleration time for electrons to attain these LFs is calculated using (3.5); note that our theoretical estimates are roughly consistent with the observed time-scales for GRB 080916C to within a factor ~ 2 uncertainty of our estimates (Table 3.2).

GRB 090510: For GRB 090510 (Abdo et al. 2009c) there was a short delay in the detection of >100 MeV photons by ~ 0.1 s (we take the trigger time to be ~ 0.5 s after the GBM trigger, because of the presence of a precursor). The 100 MeV light curve peaked at ~ 0.2 s (which we associate with the deceleration time), and so the arrival of the first >100 MeV photons was at $t/t_d \sim 0.5$. Higher energy photons arrived later: >1 GeV photons started arriving at t_d, and ~ 10 GeV photons arrived slightly after t_d. As shown in Table 3.2 these results are roughly consistent with our estimates within a factor of 2.

GRB 090902B: The 100 MeV light curve for this burst peaked at ~ 10s, which we identify as t_d, and the first >100 MeV photons were detected at ~ 3s after the trigger time (Abdo et al. 2009d), that is, $t/t_d \sim 0.3$. Most of the GeV photons arrived at $\sim t_d$. The first 10 GeV photon is detected at ~ 12 s. The

highest energy photon detected was ~ 30 GeV at 80 s, that is, at $\sim 8t_d$ [1]. The arrival time for the first >100 MeV photons from this burst agrees with the electron acceleration time (Table 3.2).

To summarize the main results of this section, it takes a few seconds for electrons in the external forward shock to be accelerated to a LF so that they can produce 100 MeV photons, and it takes a bit longer time for them to produce GeV photons. For this reason, GeV photons lag the 100 MeV radiation. If the external reverse shock flux is high (~ 1 Jy), then the first 100 MeV photons will be detected after the deceleration time, and 10 GeV photons will be detected much later ($\sim 10t_d$), when the reverse shock flux has decreased substantially . If the external reverse shock flux is small (~ 10 mJy), then the first 100 MeV photons will arrive at about a third of the deceleration time, and GeV photons will be detected starting from close to the deceleration time.

3.3 Steep rise of the high-energy photon light curve

In this section, we calculate the onset of light curves of high-energy photons (>100 MeV). According to the standard external forward shock model, and assuming instantaneous acceleration of electrons, the observed flux rises as t^3 when the CSM-density is homogeneous. We show here that the light curve rises much more steeply – similar to what is seen by *Fermi*/LAT data – when finite time for electron acceleration is taken into consideration, as was suggested by Kumar & Barniol Duran (2009).

---

[1]At this time, the LF has dropped by a factor of $8^{3/8} \sim 2$, and at $z = 1.8$, $\nu_{max,syn} \sim 10$ GeV, a factor of ~ 4 smaller than the observed value. It can be shown that inhomogeneous magnetic fields lead to an increase of $\nu_{max,syn}$ by about an order of magnitude.

		Expected	Observed	
GRB	ν	t_{acc}/t_d	t/t_d	$F_{p,d}^{max}$
080916C	100 MeV	0.3	0.6	0.30
	1 GeV	0.6	1.4	0.02
090510	100 MeV	0.3	0.5	9.90
	1 GeV	0.6	1	0.90
090902B	100 MeV	0.3	0.3	1.20
	1 GeV	0.7	1	0.10

Table 3.2: t_{acc}/t_d is the ratio of the time for electron acceleration to a specific energy (corresponding to synchrotron frequency given in column 2) and the deceleration time; it is a measure of the delay, with respect of the trigger time, for photons of a given energy to arrive at the observer when the external reverse shock emission is smaller than given in the last column of the Table. The observed time delay of photons in column 2 with respect to the trigger time is t/t_d. $F_{p,d}^{max}$ (in Jy) is the maximum possible observed external reverse shock peak flux, so that electrons can be accelerated to produce photons of energy given in column 2 at t_d.

We calculate the rise of the light curve using a simple model. The external shock emission at some frequency, ν, is zero until the blast wave reaches a radius R_0, which is set by the time-scale for electrons to be accelerated to a LF so that they start radiating at ν; this time is calculated in Section 3.2. Electron distribution function in the neighborhood of the desired LF is assumed to grow with radius as $\propto R^x$, and the distribution attains its asymptotic power-law shape at some radius $R_f \sim 2R_0$. The rise of the light curve depends on R_0, R_f, x and the deceleration radius; the rise also depends weakly on the type of CSM and the energy spectral index.

We show in Figure 3.1 light curves for two different regimes $R_0 < R_d < R_f$ (case 1) and $R_d < R_0 < R_f$ (case 2); for $R_0 < R_f < R_d$ the light curve is similar to case 1 except that between t_f (the observer time corresponding
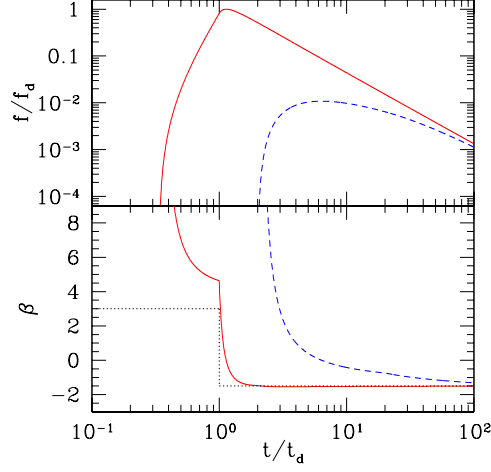
Figure 3.1: *Top.* The expected external forward shock light curve when the non-zero acceleration time of the emitting electrons is taken into account. We plot the specific flux (normalized to the flux at t_d, f_d) versus time (normalized to the deceleration time, t_d). We show two cases: (1) $R_0 < R_d < R_f$ (red solid line), and (2) $R_d < R_0 < R_f$ (blue dashed line). *Bottom.* The light curve temporal slope, $\beta = d\ln(f/f_d)/d\ln(t/t_d)$. The horizontal black dotted line shows the asymptotic value of the temporal decay index if we take electrons to accelerate instantaneously; for $t < t_d$ the light curve would rise as t^3. However, we find that the external forward shock light curve rises faster than t^3 due to the finite time it takes electrons to accelerate.

to radius R_f) and t_d the light curve rises as $\sim t^3$. Guided by the estimates provided in Section 3.2 we take $R_0 \sim R_d/3$ for 100 MeV photons, whereas for 10 GeV $R_0 \sim R_d$. We show the results for these choices of parameters in Figure 3.1; note the very steep rise of light curves which appear similar to the fast rise of the observed 100 MeV light curve for GRB 080916C as reported in Abdo et al. (2009a).

3.4 Conclusions

In this chapter we have investigated the acceleration of electrons via diffusion shock acceleration in the external forward shock of GRBs, and its implications for the high-energy photon detection by the *Fermi* Satellite. The external shock model, with a weak magnetic field, has been proposed as the origin of the observed >100 MeV emission detected by the *Fermi* Satellite from a number of GRBs (Kumar & Barniol Duran 2009, 2010). We find that high-energy electrons of Lorentz factor $\sim 10^8$, required for producing $\sim$10 GeV photons via the synchrotron process, can indeed be accelerated in an external shock that is moving through a CSM with a magnetic field of strength a few tens of μG; the electrons remain confined to the shock front as long as the upstream magnetic field is $\gtrsim 10\mu$G.

We have also calculated the time it takes for electrons to be accelerated to a Lorentz factor $\sim 10^7$ so that they can radiate synchrotron photons at $\sim$100 MeV. We find this acceleration time to be a few seconds in the observer frame; this calculation took into account radiation losses suffered during the acceleration process. This result offers a straightforward explanation as to why, for most *Fermi* GRBs, 100 MeV photons are not observed right at the trigger time but a little later. This also explains, why 100 MeV photons are observed before GeV radiation: it takes electrons radiating at GeV energies even longer time to accelerate. Taking this acceleration time into consideration while calculating high-energy light curves, we find that the light curve rises very rapidly – much faster than it does for the external forward shock model with instantaneous electron acceleration for which the flux rises as t^3 when the CSM has uniform density (the t^3 rise reflects the increasing number of swept-up electrons before the blast wave decelerates).

The detection of the first 100 MeV photons at some fraction of the deceleration time, the longer delays in the detection of higher energy photons[2] and the fast rise of the 100 MeV light curve, follow the expectation of the external forward shock model when the finite time for electron acceleration is taken into account. Detection of synchrotron photons of different energies provides an upper limit for the radiation flux produced in the reverse shock heated GRB-jet. For instance, the peak flux for the external reverse shock emission — if the peak of the spectrum is at a few eV — couldn't have been larger than about 300 mJy close to the deceleration time, for GRB 080916C, otherwise it would prevent electrons from accelerating to a Lorentz factor of $\sim 10^7$ so that they can produce synchrotron photons of 100 MeV energy at early times (see Table 3.2). Similarly, the reverse-shock flux should be $\lesssim$ 20 mJy for GRB 080916C in order that electrons in the forward shock are accelerated to a LF so that they produce 1 GeV photons.

We speculate that the lack of >100 MeV emission during the prompt phase of GRBs might be due to the presence of a bright optical source with observed flux larger than about 100 mJy, which would prevent electrons from reaching high Lorentz factors. This, coupled with the fact that GRBs with the largest LFs, which have small deceleration time, are the most likely bursts to be detected by *Fermi* (Kumar & Barniol Duran 2009) might explain the detection/non-detection of > 100 MeV radiation from GRBs.

We note that the shock-compressed magnetic field scenario requires some cross-field diffusion of particles - presumably generated by turbulence -

---

[2]Note that this possible trend in the data goes in the opposite direction than in the prompt ~ 1 MeV emission, where higher energy photons arrive *earlier* than lower energy photons in long GRBs and there is no lag detected for short GRBs (Norris et al. 1986, Norris & Bonnell 2006).

to allow them to travel back to the upstream (e.g. Achterberg et al. 2001, Lemoine et al. 2006). This turbulent layer probably occupies a small fraction of the downstream region as suggested by recent simulations by Sironi & Spitkovsky (2010). Therefore, the picture that seems to emerge from numerical simulations and *Fermi* observations, is that there might be a small region of turbulence behind the shock front that aids in the acceleration of particles across the shock, but that the radiation is mainly produced by particles that are swept downstream where the value of the downstream field is consistent with simple shock-compression of upstream field.

There exists also the possibility that the CSM seed field is actually a few μG and some instability produced ahead of the shock amplifies it to the value of a few tens of μG we infer by our modeling of *Fermi* GRBs (Kumar & Barniol Duran 2009, 2010). These instabilities have been studied by, e.g., Milosavljević & Nakar 2006, Sironi & Goodman 2007, Goodman & MacFadyen 2008, Couch et al. 2008. However, this *possible* amplification of a factor of ∼10 is much smaller than the amplification customarily invoked to explain afterglow observations.

Chapter 4

Evidence for mild deviation from power-law distribution of electrons in relativistic shocks: GRB 090902B

4.1 Introduction

The external forward shock model (see, e.g., Rees & Mészáros 1992; Mészáros & Rees 1993, 1997; Paczyński & Rhoads 1993; Wijers, Rees & Mészáros 1997; Sari, Piran & Narayan 1998; Dermer & Mitman 1999) has proven to be a very useful concept in the study of GRBs. The relativistic GRB jet or outflow interacts with the surrounding medium of the progenitor star (circumstellar medium or CSM) and drives a forward shock that accelerates the particles in the CSM, which radiate via synchrotron and Inverse Compton mechanisms. By modeling GRB afterglows one can learn more about the CSM medium properties (its density), general properties of the outflow (total kinetic energy in the shocked medium) and some details of the shock process (fractions of total energy in the shocked fluid imparted to electrons and magnetic fields). Particles are likely accelerated in collisionless shocks by the Fermi process and the resultant electron energy distribution is expected to be a decaying power-law in electron energy with index p (see, e.g., Krymskii 1977, Axford, Leer & Skadron 1978; Bell 1978; Blandford & Ostriker 1978; Blandford & Eichler 1987; Gallant & Achterberg 1999; Achterberg et al. 2001; Sironi & Spitkovsky 2011). Various studies have attempted to calculate the

value of p and to test for its universality among all bursts (see, e.g., Shen, Kumar & Robinson 2006). Even though in previous studies a single value of p is assumed for a particular burst, there is the possibility that the distribution function might deviate from a single power-law.

In this chapter we study the late ($\gtrsim$ 0.5 d) afterglow of GRB 090902B in the context of the external forward shock model. In Section 4.2, we study the afterglow data for this GRB. In Section 4.3, we present alternatives to the scenario proposed in Section 4.2. In particular, we devote most of this section on a very detailed calculation of Inverse Compton losses, which might mitigate some of the issues presented in Section 4.2. In Section 4.4, we show that the only viable solution seems to be that the electron energy distribution is a little steeper for the X-ray radiating electrons than for the optical electrons in the external forward shock, that is, there is some curvature in the electron energy distribution spectrum. In Section 4.5, we use the results of the previous section to study the early ($\sim$ 50 s) high-energy gamma-ray data of GRB 090902B and find it consistent with the same origin as the late time afterglow emission. In Section 4.6, we explore the possibility that the additional power-law spectral component found at $\sim$ 10 s, in addition to the prompt Band function, has also an external forward shock origin. We discuss our results in Section 4.7 and present our Conclusions in Section 4.8.

4.2 Late time afterglow data of GRB 090902B

GRB 090902B (Abdo et al. 2009d) has been studied extensively for its high energy emission during the prompt phase detected by the LAT (Large Area Telescope) onboard of the *Fermi* satellite (see, e.g., Asano, Inoue & Mészáros 2010; Feng & Dai 2010; Ghisellini, Ghirlanda & Nava 2010, Kumar

& Barniol Duran 2010; Toma, Wu & Mészáros 2010; Liu & Wang 2011; Zhang et al. 2011; Zhao, Li & Bai 2011). In this chapter we focus on the late time afterglow behavior in the radio, optical and X-ray bands (Cenko et al. 2010, McBreen et al. 2010, Pandey et al. 2010) with the assumption that radiation in these bands is produced by the synchrotron process in the external forward shock. We study the afterglow data after about a day of the explosion, because the optical data previous to this epoch seems to be dominated by the external reverse shock (Pandey et al. 2010). Here and in the rest of the chapter, we use the convention that the observed specific flux at a particular energy, ν, is given by $f_\nu(t) \propto \nu^{-\beta} t^{-\alpha}$, where t is the observed time and β (α) is the spectral (temporal) index. The GRB 090902B observations for $t \gtrsim 1$ d can be summarized as follows. The optical data (2 eV), detected by UVOT (Ultraviolet Optical Telescope) onboard of the *Swift* satellite, shows $\beta_{opt} = 0.76 \pm 0.07$ and $\alpha_{opt} = 0.89 \pm 0.05$, whereas the X-ray data (1 keV), detected by XRT (X-ray Telescope) also onboard *Swift*, shows $\beta_x = 0.90 \pm 0.13$ and $\alpha_x = 1.36 \pm 0.03$ (Cenko et al. 2010).

We assume that electrons in the CSM are accelerated to a power-law in the external forward shock model, such that the electrons energy distribution is given by $n(\epsilon) \propto \epsilon^{-p}$, where p is the power-law index. In this scenario both the spectral index and the temporal decay index depend on p (Sari et al. 1998), therefore, one can relate α and β via the "closure relations" (see table 1 of Zhang & Mészáros 2004). The values of the spectral and decay indices will depend also on the region where the observed frequency falls in the synchrotron spectrum. The synchrotron spectrum is characterized by three frequencies: the self-absorption frequency (ν_a), the injection frequency (ν_i), and the cooling frequency (ν_c); ν_i and ν_c correspond to the synchrotron frequencies of electrons

(just downstream of the shock front) whose energy correspond to the minimum energy of injected electrons and to the electrons that cool on a dynamical time, respectively, and ν_a is the highest frequency at which the system becomes opaque to synchrotron absorption.

Trying to explain both the X-ray and optical late time data for GRB 090902B in the context of the external forward shock model is not straightforward. We use the common terminology "slow cooling" ("fast cooling"), for $\nu_i < \nu_c$ ($\nu_c < \nu_i$), and constant density CSM (wind medium) for $s = 0$ ($s = 2$), where the CSM density falls off as $\propto R^{-s}$ and R is the distance from the center of the explosion. For this GRB we have the following options:

Option 1: If the optical band, ν_{opt}, and the X-ray band, ν_x, are in the same region of the synchrotron spectrum, that is, $\nu_i < \nu_{opt} < \nu_x < \nu_c$, then $\beta_x = \beta_{opt}$, which is supported by the data. However, the temporal decay indices in these two bands, which should be exactly the same, are very different. The X-ray decay is considerable steeper than the optical one, $\Delta\alpha = \alpha_x - \alpha_{opt} = 0.47 \pm 0.08$, and this particular issue is crucial for the rest of the chapter.

Option 2: If the optical band and the X-ray band lie in different parts of the spectrum, for instance, $\nu_i < \nu_{opt} < \nu_c < \nu_x$, then the spectral indices should differ by $\Delta\beta = \beta_x - \beta_{opt} = 0.5$, which is not supported by the data. Moreover, $\Delta\alpha$ is expected to be $-1/4$ (wind) or $1/4$ (constant density CSM), which is also inconsistent with the data – the X-ray decays too quickly.

Option 3: If both optical and X-ray bands lie above the cooling frequency, that is, $\nu_i < \nu_c < \nu_{opt} < \nu_x$, the discrepancies with the expected data and the observations are similar to Option 1. Since the temporal decay index is independent of type of medium there is no way to discriminate its type (Kumar 2000). This case is analogous to the fast cooling case where $\nu_c < \nu_i < \nu_{opt} < \nu_x$.

Option 4: Any possibility where $\nu_{opt} < \nu_i$ is ruled out by the data. For the case of slow cooling, the spectrum would be $\beta_{opt} = -1/3$ for both types of medium, which is inconsistent with the observed optical spectrum. Moreover, the optical light curve should be slowly rising (flat) for the constant medium (wind) case, which is inconsistent with the decaying light curve. For the case of fast cooling, if $\nu_{opt} < \nu_c < \nu_i$, then $\beta_{opt} = -1/3$, and if $\nu_c < \nu_{opt} < \nu_i$, then $\beta_{opt} = 1/2$ and $\alpha_{opt} = 1/4$ - for both types of medium - which is inconsistent with the optical spectrum and light curve.

We can see that Option 4 faces severe difficulties, thus we will not consider it any further. We will explore Options 1-3 in detail throughout the chapter.

First, we try to determine the type of medium that the blast wave is running into. For Options 1 and 2, the wind medium case can be ruled out. The reason is that, for Option 1, both the expected optical and X-ray decay would be too steep compared with the observations. For Option 2, one would expect $\Delta\alpha = \alpha_x - \alpha_{opt} = -1/4$, that is, the optical decay should be steeper than the X-ray one, which is the opposite to what it is seen. For these reasons, the only viable possibilities left are Options 1 and 2 with constant CSM, and for Option 3, optical and X-ray fluxes are independent of the type of CSM.

Pandey et al. (2010) and Cenko et al. (2010) have also analyzed GRB 090902B and they both prefer Option 2 with a constant density CSM. Pandey et al. (2010) suggested a value of $p = 1.8 \pm 0.2$, however, as the authors point out, the optical spectrum and X-ray temporal decay are inconsistent with the observed values. They appeal to optical extinction, which would make the optical spectrum agree with the observed value; nevertheless, the expected X-ray temporal decay is shallower than the observed one. Cenko et al. (2010)

find $p = 2.22^{+0.08}_{-0.04}$, which naturally mitigates the problem Pandey et al. (2010) have with the optical spectrum, but also gives an X-ray temporal decay that is shallower than the observed one. They suggest radiative losses to make the X-ray decay steeper - consistent with observations - however, as we will see in the next section, this would also affect the optical decay, and therefore it is not a viable option.

4.3 Saving the external forward shock model

In this section, we explore a number of different possibilities that might modify the standard external forward shock model and help us reconcile the theory with the observations for GRB 090902B. In particular, we are interested in mechanisms that could potentially make the X-ray light curve *steeper* than expected in the simple external forward shock model. We consider the following possibilities: (i) Radiative losses in the blast wave, (ii) Temporal evolution of microphysical parameters, (iii) Temporal evolution of Compton-Y parameter which would affect only the light curve of the observing band above ν_c and (iv) Curvature in the injected electron spectrum.

Some of these possibilities have been discussed in the literature and applied to a number of GRBs. Radiative losses in the blast wave was considered by, e.g., Cohen, Piran & Sari (1998), Sari et al. (1998). Also, the possibility of having the microphysical parameters vary with time in the external shock was proposed by Panaitescu et al. (2006). Recently, Wang et al. (2010) considered the possibility of having Klein-Nishina suppression weaken with time so as to increase the Inverse Compton losses and steepen the > 100 MeV light curve of *Fermi* GRBs. We now explore possibilities (i)-(iv) to find out if any of these can help us understand the optical and X-ray afterglow data for GRB

090902B.

4.3.1 Radiative losses or temporal evolution of microphysical parameters

For a constant CSM, the specific flux for an observed band $\nu > \nu_i$ is given by (see, e.g., Sari et al. 1998, Kumar 2000, Panaitescu & Kumar 2000)

$$
f_\nu \propto \begin{cases} E_{KE,iso}^{\frac{p+3}{4}} \epsilon_e^{p-1} \epsilon_B^{\frac{p+1}{4}} n^{\frac{1}{2}} t^{-\frac{3(p-1)}{4}} \nu^{-\frac{p-1}{2}} & \text{if } \nu_i < \nu < \nu_c \\ E_{KE,iso}^{\frac{p+2}{4}} \epsilon_e^{p-1} \epsilon_B^{\frac{p-2}{4}} t^{-\frac{3p-2}{4}} \nu^{-\frac{p}{2}} (1+Y)^{-1} & \text{if } \nu_c < \nu. \end{cases}
\tag{4.1}
$$

where ϵ_e and ϵ_B are the fractions of energy of the shocked gas in electrons and magnetic fields, respectively, t is the time since the beginning of the explosion in the observer frame, $E_{KE,iso}$ is the isotropic kinetic energy in the shocked medium, n is the density of the CSM and Y is the Compton-Y parameter, which is the ratio of the Inverse Compton to the synchrotron loss rates. Equation (4.1) is valid for $p > 2$; closure relations for $p < 2$ can be found in table 1 of Zhang & Mészáros (2004).

According to Option 2, for $p = 2.3$, the expected optical decay ($\nu_i < \nu_{opt} < \nu_c$) is given by $\propto t^{-0.98} \nu^{-0.65}$, consistent with both the optical decay and spectrum within 2-σ, while the expected X-ray flux ($\nu_c < \nu_x$) is $\propto t^{-1.23} \nu^{-1.15}$, consistent with the observed X-ray spectrum within 2-σ, however, inconsistent with the observed X-ray decay by more than 4-σ. To be consistent, the X-ray light curve must be steepened by $\propto t^{-0.13}$.

If the X-ray band is above ν_c then, according to the second part of equation (4.1), the way to steepen the light curve is by appealing to a decrease with time of $E_{KE,iso}$, ϵ_e or an increase of Y (the explicit dependence of ϵ_B in flux is extremely weak for $\nu > \nu_c$). The decrease of $E_{KE,iso}$ and ϵ_e will also

steepen the optical light curve, therefore, the increase of Compton-Y is the only possibility that we consider. Let us explore these arguments in detail now.

Radiative losses make the kinetic energy in the external forward shock decrease with time. For the X-ray band $(\nu_c < \nu_x)$ with $p = 2.3$, the observed flux is $\propto E_{KE,iso}^{1.08}$ and, thus, $E_{KE,iso}$ should decrease as $\propto t^{-0.12}$ to steepen the X-ray value to the observed value. However, since the flux in the optical band $(\nu_i < \nu_{opt} < \nu_c)$ is $\propto E_{KE,iso}^{1.33}$, the optical light curve will steepen by $\propto t^{-0.16}$, making the optical decay $\alpha_{opt} = 1.14$ inconsistent with the observations by 5-σ. Therefore, radiative losses cannot save the external forward shock model in Option 2. Appealing to a temporal evolution of ϵ_e or ϵ_B faces similar difficulties.

In Options 1 and 3, the X-ray and optical bands lie in the same spectral regime, therefore their fluxes have the same dependence on energy and microphysics parameters. Appealing to a temporal change of any of these would modify both light curves exactly the same way. For this reason, neither radiative losses nor temporal evolution of microphysical parameters can explain why the X-ray light curve decays faster than the optical one does.

4.3.2   Temporal evolution of Compton-Y

As mentioned above, another possibility could be that the Compton-Y parameter increases with time as $(1 + Y) \propto t^{0.13}$. Since Y only affects the flux for $\nu_c < \nu$ – see equation (4.1) – it would only affect the X-ray band, not the optical one (when $\nu_i < \nu_{opt} < \nu_c$), and since the optical data already agrees with the expected value, then this possibility is very attractive.

The Compton-Y parameter that needs to be calculated is the one for

electrons radiating at 1 keV, Y_x, since it is the X-ray flux at 1 keV that needs to be steepened. Moreover, the temporal behavior $(1+Y_x) \propto t^{0.13}$ should hold during the entire period of X-ray observations, which start at ~ 12.5 h and extend until ~ 15 d. In the following subsections, we search the 4-D parameter space (ϵ_e, ϵ_B, n, $E_{KE,iso}$) to determine if there is any part of the parameter space that satisfies the condition that $(1+Y_x) \propto t^{0.13}$. Before this, we present a very detailed calculation of Compton-Y parameter for electrons of arbitrary Lorentz factor (LF), where we take into account the effect of Inverse Compton and synchrotron losses on the electron energy distribution self-consistently and include the Klein-Nishina cross section and electron recoil effects on Compton scatterings.

4.3.2.1 Calculation of Inverse Compton loss

A general calculation of Inverse Compton loss has been carried out by a number of authors (see, e.g., Jones 1968, Blumenthal & Gould 1970, see also, Blumenthal 1970). Inverse Compton loss has also been calculated in the context of GRB prompt emission and afterglows (see, e.g., Panaitescu & Kumar 2000; Sari & Esin 2001; and more recently Bošnjak, Daigne & Dubus 2009, Nakar, Ando & Sari 2010, Wang et al. 2010, Daigne, Bošnjak & Dubus 2011). The calculation of Inverse Compton loss, which allows us to calculate Compton-Y, is not straightforward. Electrons cool via Inverse Compton scattering when they interact with synchrotron photons, and the same electron population is the one that emits the synchrotron photons. It is a problem of feedback, because the electron population in turn depends on the cooling the electrons experience. In this subsection we outline the calculation for Compton-Y. We include Klein-Nishina effects and also relativistic corrections

of the outgoing energy of the Inverse Compton scattered photons.

In the co-moving frame of the electron, the energy of an outgoing photon after the scattering off of an electron is given by (see, e.g., Rybicki & Lightman 1979, hereafter RL79)

$$x_1' = \frac{x'}{1 + x'(1 - \cos{(\theta_1' - \theta')})},\tag{4.2}$$

where the subscript "1" corresponds to the outgoing photon and the superscript $(')$ means that the quantity is measured in the co-moving frame of the electron before scattering. The quantity x' (x_1') is defined as $x' = h\nu'/m_e c^2$ $(x_1' = h\nu_1'/m_e c^2)$, where ν' (ν_1') is the frequency of the incoming (outgoing) photon, and h, c and m_e are Planck's constant, the speed of light and the mass of the electron, respectively. The angle θ' (θ_1') is that of the direction of the incoming (outgoing) photon with respect to the direction of the electron's momentum before scattering (see Figure 4.1).

The frequency of the incoming photon in the electron rest frame before scattering can be expressed in terms of the frequency measured in the lab frame, ν, by using the relativistic Doppler formula

$$\begin{aligned} \nu' &= \nu\gamma_e(1 + \beta_e \cos\theta) \\ \nu &= \nu'\gamma_e(1 - \beta_e \cos\theta') \end{aligned}\tag{4.3}$$

and the transformation between the angle of the incoming photon θ' in the electron rest frame and the lab frame, θ, is given by

$$\sin\theta' = \left(\frac{\nu}{\nu'}\right)\sin\theta = \frac{\sin\theta}{\gamma_e(1 + \beta_e \cos\theta)}\tag{4.4}$$

where β_e is the velocity of the electron divided by c, $\gamma_e = 1/\sqrt{1 - \beta_e^2}$ is the LF of the electron.
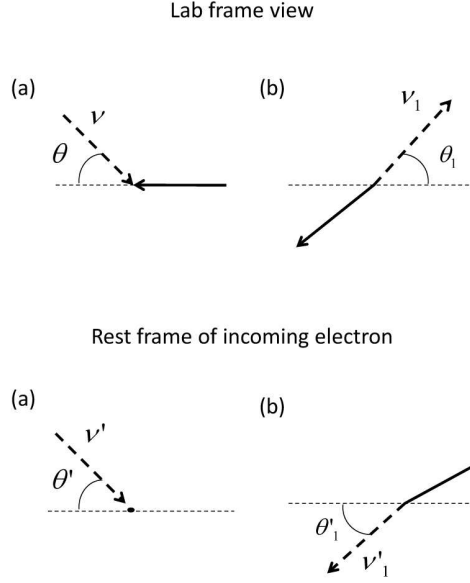
Figure 4.1: Geometry for scattering of a photon by an electron. The electron trajectory is denoted by a thick solid line, while the trajectory of the incoming and outgoing photon is denoted by a thick dashed line. We present the scattering viewed from the lab frame (top) and viewed from the rest frame of the incoming electron, that is, the electron is at rest in this frame before scattering (bottom). The diagrams before and after the collision are presented in (a) and (b), respectively. The un-primed quantities are in the lab frame, while the primed ($'$) quantities are in the electron rest frame before scattering.

The energy in a bundle of scattered photons in the electron rest frame is given by

$$dE'_s = \left[d\Omega' d\nu' \frac{I'_{\nu'}(\theta')}{h\nu'} \right] \frac{d\sigma_{KN}}{d\Omega'_1} h\nu'_1 d\Omega'_1 dt' \tag{4.5}$$

where $I'_{\nu'}$ is the specific intensity (in units of erg s^{-1} cm^{-2} sr^{-1} Hz^{-1}), $d\Omega'$ $(d\Omega'_1)$ is the differential solid angle of the incoming (outgoing) photons, $d\sigma_{KN}/d\Omega'_1$ is the differential cross section (the Klein-Nishina formula) and dt' is the duration of the event measured in the electron rest frame. The quantity in the square bracket is the number of photons per unit time per unit area moving within solid angle $d\Omega'$ and frequency band $d\nu'$ incident on the electron.

The component of the momentum vector of the scattered photons along the electron velocity considered above is

$$dp'_s = d\Omega' d\nu' \frac{I'_{\nu'}(\theta')}{h\nu'} \frac{d\sigma_{KN}}{d\Omega'_1} \frac{h\nu'_1}{c} \cos\theta'_1 d\Omega'_1 dt'. \tag{4.6}$$

The scattered photon energy in the lab frame is given by (see, e.g., RL79)

$$dE_s = \gamma_e(dE'_s - \beta_e dp'_s) = \gamma_e(1 - \beta_e \cos\theta'_1)dE'_s. \tag{4.7}$$

Using the fact that the time interval in the lab frame is $dt = \gamma_e dt'$, one finds

$$\frac{dE_s}{dt} = (1 - \beta_e \cos\theta'_1)\frac{dE'_s}{dt'}, \tag{4.8}$$

and combining this last equation with equation (4.5), we arrive to

$$\frac{dE_s}{dt} = \int d\Omega' d\nu' \frac{I'_{\nu'}(\theta')}{\nu'} \int d\Omega'_1 \nu'_1 \frac{d\sigma_{KN}}{d\Omega'_1}(1 - \beta_e \cos\theta'_1). \tag{4.9}$$

84

In this last equation, both $d\sigma_{KN}/d\Omega'_1$ and ν'_1 are functions of ν' and $(\theta'_1 - \theta')$, and we can use equation (4.2) to eliminate ν'_1. We thus find a general equation that describes the energy loss of an electron due to Inverse Compton cooling

$$\frac{dE_s}{dt} = \int d\Omega' d\nu' I'_{\nu'}(\theta') \int d\Omega'_1 \frac{1 - \beta_e \cos\theta'_1}{1 + x'[1 - \cos(\theta'_1 - \theta')]} \frac{d\sigma_{KN}}{d\Omega'_1}, \qquad (4.10)$$

where the Klein-Nishina cross section is given by (see, e.g., RL79 eq. 7.4)

$$\frac{d\sigma_{KN}}{d\Omega'_1} = \frac{3\sigma_T}{16\pi} \left(\frac{\nu'_1}{\nu'}\right)^2 \left[\frac{\nu'}{\nu'_1} + \frac{\nu'_1}{\nu'} - \sin^2(\theta'_1 - \theta')\right], \qquad (4.11)$$

and, again, one can use equation (4.2) to eliminate ν'_1, which yields

$$\begin{aligned}
\frac{d\sigma_{KN}}{d\Omega'_1} =\ & \frac{3\sigma_T}{16\pi} \left[\frac{1}{1 + x'[1 - \cos(\theta'_1 - \theta')]}\right]^2 \left[\frac{1}{1 + x'[1 - \cos(\theta'_1 - \theta')]}\right. \\
& \left. + x'[1 - \cos(\theta'_1 - \theta')] - \cos^2(\theta'_1 - \theta')\right].
\end{aligned} \qquad (4.12)$$

Equation (4.10) is general and contains no assumptions. To simplify the calculation we now make two assumptions. The first assumption allows us to simplify the expression of $\cos(\theta'_1 - \theta')$ the following way. The integrand of $d\Omega'_1$ in equation (4.10) depends on θ', and both x' and $d\sigma_{KN}/d\Omega'_1$ also depend on θ' – see definition of x' and equations (4.3) and (4.12). The cross section starts to fall-off steeply with angle only when $|\theta'_1 - \theta'| \gtrsim 1/\sqrt{x'}$; and also $\theta' \approx \gamma_e^{-1}$ – see equation (4.4). Thus, for parameters of interest to us, where $\gamma_e \gtrsim 10^3$ and $x' \lesssim 10^2$, we have $\theta'_1 \sim 0.1$ and $\theta' \sim 10^{-3}$. In this case, we can approximate $\cos(\theta'_1 - \theta') \approx \cos\theta'_1$. We call this the "head-on" approximation, since it corresponds to an incoming photon moving in the same direction as the incoming electron velocity vector before the collision as seen in the electron

rest frame. We note, however, that we cannot set $\theta' = 0$ in equation (4.3), since that would overestimate ν' by a factor of ~ 2. The second assumption we make is that the energy density in photons in the co-moving frame of the source where the photons are generated is distributed isotropically, therefore, we can write

$$d\Omega' d\nu' I'_{\nu'} = d\Omega d\nu I_\nu \left(\frac{\nu'}{\nu}\right)^2 = d\Omega d\nu \frac{u_\nu}{4\pi} c\gamma_e^2 (1 + \beta_e \cos\theta)^2, \qquad (4.13)$$

where u_ν is the source rest frame photon energy density. To derive the last expression we have used the fact that I_ν/ν^3 is a Lorentz invariant quantity and that $d\Omega' = d\Omega(\nu/\nu')^2$. With these two assumptions we can rewrite equation (4.10) as

$$\frac{dE_s}{dt} = \frac{c\gamma_e^2}{2} \int_0^\infty d\nu u_\nu \int_{-1}^1 d\mu (1 + \beta_e \mu)^2 \int_{-1}^1 d\mu'_1 \frac{1 - \beta_e \mu'_1}{1 + x'(1 - \mu'_1)} \frac{d\sigma_{KN}}{d\mu'_1}, \qquad (4.14)$$

and the Klein-Nishina cross section is given by

$$\frac{d\sigma_{KN}}{d\mu'_1} = \frac{3\sigma_T}{8} \frac{1}{[1 + x'(1 - \mu'_1)]^2} \left[\frac{1}{1 + x'(1 - \mu'_1)} + x'(1 - \mu'_1) - {\mu'_1}^2\right], \qquad (4.15)$$

where $\mu = \cos\theta$, $\mu'_1 = \cos\theta'_1$, and, as defined before, $x' = h\gamma_e\nu(1 + \beta_e\mu)/m_e c^2$. Combining equations (4.14) and (4.15) we find

$$\begin{aligned}
\frac{dE_s}{dt} &= \frac{3}{16}\sigma_T c\gamma_e^2 \int_0^\infty d\nu u_\nu \int_{-1}^1 d\mu (1 + \mu)^2 \int_{-1}^1 d\mu'_1 \left[\frac{1 - \mu'_1}{[1 + x'(1 - \mu'_1)]^4}\right. \\
&\quad \left. + \frac{x'(1 - \mu'_1)^2}{[1 + x'(1 - \mu'_1)]^3} - \frac{{\mu'_1}^2(1 - \mu'_1)}{[1 + x'(1 - \mu'_1)]^3}\right],
\end{aligned} \qquad (4.16)$$

86

where we made another approximation, which is that $\beta_e \approx 1$, which is valid for the case, where $\gamma_e \gg 1$ studied here.

The μ_1' integral in equation (4.16) can be carried out analytically. Let us define a function

$$G_n(x) = \int_{-1}^{1} \frac{d\mu_1'}{[1 + x(1 - \mu_1')]^n}. \tag{4.17}$$

It is straightforward to show that

$$
\begin{aligned}
G_1(x) &= \frac{\ln(1 + 2x)}{x}, \\
G_n(x) &= \frac{1}{(n-1)x}\left[1 - \frac{1}{(1 + 2x)^{n-1}}\right], \qquad \text{for } n \neq 1.
\end{aligned}
\tag{4.18}
$$

With this last equation, we can evaluate the μ_1' integral of the first term in equation (4.16), which is

$$\int_{-1}^{1} d\mu_1' \frac{1 - \mu_1'}{[1 + x'(1 - \mu_1')]^4} = -\frac{1}{3}\frac{d}{dx'}G_3(x') = \frac{2}{3}\frac{(3 + 2x')}{(1 + 2x')^3}, \tag{4.19}$$

and also the second term, which yields

$$\int_{-1}^{1} d\mu_1' \frac{x'(1 - \mu_1')^2}{[1 + x'(1 - \mu_1')]^3} = \frac{x'}{2}\frac{d^2}{dx'^2}G_1(x') = \frac{\ln(1 + 2x')}{x'^2} - \frac{2(1 + 3x')}{x'^2(1 + 2x')^2}. \tag{4.20}$$

To carry out the integral of the third term, we define a new function

$$J_n(x) = \int_{-1}^{1} d\mu_1' \frac{\mu_1'}{[1 + x(1 - \mu_1')]^n}, \tag{4.21}$$

87

which can be shown to be

$$J_1(x) = \frac{x+1}{x^2}\ln(1+2x) - \frac{2}{x},$$

$$J_n(x) = \frac{1}{(n-1)x}\left[1 + \frac{1}{(1+2x)^{n-1}}\right] - \frac{1}{(n-1)x}G_{n-1}(x), \quad (4.22)$$

for $n = 1$ and $n \neq 1$, respectively.

Using partial fractions decomposition, the μ_1' integral of the third term in equation (4.16) can be written as

$$\int_{-1}^{1} d\mu_1' \frac{\mu_1'^2(1-\mu_1')}{[1+x'(1-\mu_1')]^3} = -\frac{1}{x'^2}J_1(x') + \frac{2+x'}{x'^2}J_2(x') - \frac{1+x'}{x'^2}J_3(x'), \quad (4.23)$$

and by using equation (4.22), we find

$$\int_{-1}^{1} d\mu_1' \frac{\mu_1'^2(1-\mu_1')}{[1+x'(1-\mu_1')]^3} = -\frac{2'x+3}{x'^4}\ln(1+2x') + \frac{2x'^3 + 20x'^2 + 22x' + 6}{x'^3(1+2x')^3}. \quad (4.24)$$

Combining equations (4.19), (4.20) and (4.24), the μ_1' integral in equation (4.16) can be written as

$$K(x') = \frac{x'^2 + 2x' + 3}{x'^4}\ln(1+2x') - \frac{2(22x'^4 + 75x'^3 + 99x'^2 + 51x' + 9)}{3x'^3(1+2x')^3}. \quad (4.25)$$

In addition, we make one last transformation of equation (4.16) and that is the following: Since x' depends on $\mu = \cos\theta$, we write it as

$$x' = \frac{h\nu\gamma_e}{m_e c^2}(1 + \beta_e\cos\mu) \approx X(1+\mu), \quad (4.26)$$

88

where we have defined a new variable $X = h\nu\gamma_e/m_ec^2$, and we again have made use of the assumption that $\gamma_e \gg 1$, so that $\beta_e \approx 1$. With this, equation (4.16) can be rewritten as

$$\frac{dE_s}{dt} = \frac{3}{16}\sigma_T c\gamma_e^2 \int_0^\infty d\nu \frac{u_\nu}{X^3} \int_{X(1-\beta_e)}^{X(1+\beta_e)} dx' x'^2 K(x'). \qquad (4.27)$$

The x' integral can be done analytically, except for one term in the integrand, which is $2\ln(1+2x')/x'$, whose integral is a polylogarithm, specifically a dilogarithm or Spence's function.

The rate of Inverse Compton energy loss can be expressed as

$$\frac{d}{dt}(m_ec^2\gamma_e) = -\frac{dE_s}{dt} + \int d\nu \; u_\nu\sigma_{KN}c \approx -\frac{dE_s}{dt} \qquad (4.28)$$

where dE_s/dt is given by equation (4.27), and the second term is the integral of photon energy before scattering which is negligible compared with dE_s/dt for $\gamma_e \gg 1$.

Finally, the Compton-Y parameter, defined as the ratio of the rate of Inverse Compton energy loss and the rate of synchrotron energy loss, is given by

$$Y(\gamma_e) = \frac{\frac{dE_s}{dt}}{\frac{1}{6\pi}\sigma_T B^2\gamma_e^2 c}. \qquad (4.29)$$

The only thing left to determine now is the energy density in photons, u_ν. Since in the case of GRBs the entire source (jet) is moving relativistically towards the observer, then the photon energy density needed is the one measured in the source co-moving frame. All quantities considered in the following calculation will be in the source co-moving frame.

The power emitted in 4π sr at frequency ν by an electron in the shell (in units of erg s^{-1} sr^{-1} Hz^{-1}) is (see, e.g., RL79)

$$P_\nu = \frac{e^3 B}{m_e c^2} \left(\frac{\nu}{\nu_{\gamma_e}}\right)^{1/3}, \tag{4.30}$$

where e is the electron charge, B is the magnetic field in the shell co-moving frame and ν_{γ_e} is the synchrotron frequency of an electron with LF γ_e, which is given by

$$\nu_{\gamma_e} = \frac{e B \gamma_e^2}{2\pi m_e c}. \tag{4.31}$$

The numerical factors in the last two expressions are different than the ones in Wijers & Galama (1999) for $2 \lesssim p \lesssim 3$ by only less than $\sim 10\%$ and $\sim 40\%$ for equations (4.30) and (4.31), respectively. P_ν in equation (4.30) is valid for $\nu < \nu_{\gamma_e}$, for $\nu > \nu_{\gamma_e}$ we take P_ν to vanish, even though strictly speaking it decreases exponentially, which introduces a very small error.

We will now calculate the specific intensity, I_ν, in the middle of the shell (see Figure 4.2). Let us assume that the column density of electrons (emitters) in the shell is N (number of emitters per unit area) and the shell radius and LF are R and Γ, respectively. Since the photons cannot arrive at a point in the middle of the shell from a distance larger than R/Γ, which is the radius of the causally connected region, then the specific intensity in the middle of the shell is approximately given by

$$I_\nu(\theta) = \begin{cases} \frac{P_\nu}{4\pi} \frac{N}{2} |\sec\theta| & \text{for } 0 \le \theta \le \pi/3 \text{ and } 2\pi/3 \le \theta \le \pi \\ \frac{P_\nu N}{4\pi} & \text{for } \pi/3 < \theta < 2\pi/3, \end{cases} \tag{4.32}$$
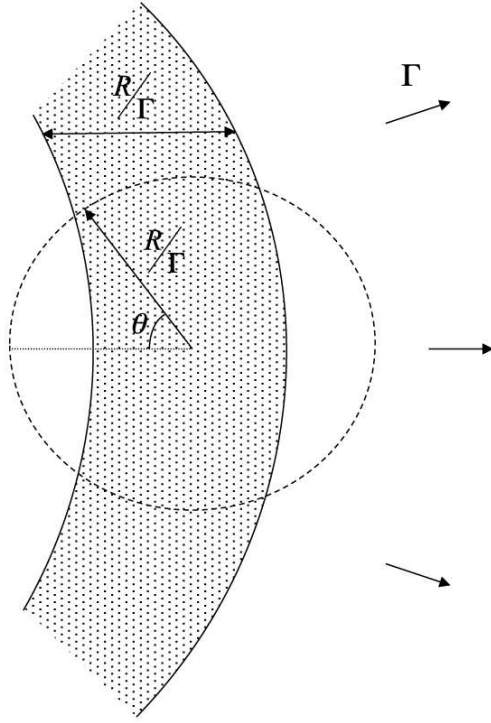
Figure 4.2: Schematic of a GRB jet. The width of the shell in the co-moving frame of the shell is R/Γ, where R is the distance from the center of the explosion and Γ is the LF of the source. To calculate the specific intensity in the middle of the shell one needs to take into account all photons produced by electrons (emitters) within the causally connected region of radius R/Γ. Since $R/\Gamma \ll R$ we assume a rectangular slab geometry.

where we have used a rectangular slab geometry since $R/\Gamma \ll R$. Therefore, we find that the energy density in photons of frequency ν in the middle of the shell is

$$u_\nu = \frac{1}{c}\int d\Omega I_\nu(\theta) = \frac{P_\nu N}{c}\left(\frac{\ln 2}{2} + \frac{1}{2}\right). \qquad (4.33)$$

A similar analysis shows that the photon energy density near the inner or outer edge of the shell is $u_\nu = P_\nu N/2c$. Thus, the average value of u_ν in the shell is $u_\nu \approx 0.7 P_\nu N/c$.

The column density of electrons can be written as a function of the electron energy distribution, which is defined as $n(\gamma_e)$ (number of electrons per unit area per unit γ_e). We define the specific flux in the co-moving frame of the shell, $f_\nu \equiv P_\nu N$, thus, $u_\nu \approx 0.7 f_\nu/c$. The specific flux is given by

$$f_\nu = \int d\gamma_e n(\gamma_e) P_\nu, \qquad (4.34)$$

where $n(\gamma_e)$ is calculated self-consistently by solving a coupled set of equations for $n(\gamma_e)$ and radiation (see below). Using equation (4.30) we rewrite the last equation as

$$f_\nu = \int_{\gamma_\nu}^\infty d\gamma_e n(\gamma_e) \left[\frac{e^3 B}{m_e c^2}\right]\left(\frac{\gamma_\nu}{\gamma_e}\right)^{2/3}, \qquad (4.35)$$

where γ_ν is the LF of electrons radiating at synchrotron frequency ν, that is – see equation (4.31) –,

$$\gamma_\nu^2 = \frac{2\pi m_e c\nu}{eB}. \qquad (4.36)$$

The task now is to determine the electron energy distribution, $n(\gamma_e)$, in order to calculate the synchrotron flux given by equation (4.35). The electron distribution function is determined by solving the following continuity equation

$$\frac{\partial n(\gamma_e)}{\partial t} + \frac{\partial}{\partial \gamma_e}[\dot{\gamma}_e n(\gamma_e)] = S(\gamma_e), \tag{4.37}$$

where the source term, $S(\gamma_e)$, is given by

$$S(\gamma_e) = \begin{cases} \dot{N}\left(\frac{\gamma_e}{\gamma_i}\right)^{-p} & \gamma_e \geq \gamma_i \\ 0 & \gamma_e < \gamma_i, \end{cases} \tag{4.38}$$

$\dot{N}$ is the total number of electrons crossing the shock front per unit time per unit area, and γ_i is the minimum LF of electrons injected in the shock.

We can solve equation (4.37) approximately the following way. Let us define a cooling time for electrons, t'_{cool}, in the shell co-moving frame, as follows $t'_{cool}(\gamma_e) = \gamma_e/\dot{\gamma}_e$ and a co-moving dynamical time, t'_{co}, as $t'_{co} = R/(\Gamma c)$. The dynamical time in the shell co-moving frame is related to the one in the observer frame, t_{obs}, as $t'_{co} = \Gamma t_{obs}/(1 + z)$, where z is the redshift and the column density is related to the shock radius, R, as $nR/3$, therefore, $\dot{N} = nR/3t'_{co}$.

If $t'_{cool} > t'_{co}$ for a given γ_e, electrons of this LF have not cooled much in the available time, therefore, equation (4.37) reads

$$n(\gamma_e) \approx t'_{co} S(\gamma_e), \qquad \text{for } t'_{cool} > t'_{co}. \tag{4.39}$$

On the other hand, when $t'_{cool} < t'_{co}$ for a given γ_e, then $n(\gamma_e)$ wouldn't change with time and thus

$$\frac{\partial}{\partial \gamma_e} [\dot{\gamma}_e n(\gamma_e)] \approx S(\gamma_e). \tag{4.40}$$

or

$$n(\gamma_e) = \int_{\gamma_e}^{\infty} d\gamma_e' S(\gamma_e') \Big/ \dot{\gamma}_e, \qquad \text{for } t_{cool}' < t_{co}'. \tag{4.41}$$

To summarize, we solve numerically the following equations *simultaneously* to find Compton $Y(\gamma_e)$: equation (4.37) to find the electron energy distribution, equation (4.35) to find the synchrotron flux, equation (4.27) to find the energy loss rate due to Inverse Compton and substituting all these results into equation (4.29) gives $Y(\gamma_e)$.

4.4 Solution for GRB 090902B

We use the parameters of GRB 090902B, $z = 1.8$ (Cucchiara et al. 2009), luminosity distance of $d_L = 4.3 \times 10^{28}$ cm and we also use $p = 2.3$ (see Section 4.3.1) and investigate Option 2 ($\nu_i < \nu_{opt} < \nu_c < \nu_x$) in detail. For this, we use the formalism developed in the previous section.

We use a numerical code that scans the 4 external forward shock parameters, viz. ϵ_e, ϵ_B, n and $E_{KE,iso}$, and finds the subset that satisfies a set of chosen constraints (see below). The parameters are varied in the following ranges: $\epsilon_e = 10^{-2} - 10^{-0.2}$, $\epsilon_B = 10^{-9} - 10^{-1}$, $n = 10^{-4} - 10$ cm^{-3} and $E_{KE,iso} = 10^{53} - 10^{55.5}$ erg. The value of the isotropic energy released in gamma-rays for GRB 090902B was $E_{\gamma,iso} = 3.63 \times 10^{54}$ erg (Abdo et al. 2009d), this is the reason why we chose to vary $E_{KE,iso}$ from being 30 times smaller to ~ 10 times larger than $E_{\gamma,iso}$. The radiation efficiency of the prompt

gamma-ray emission is given by $\eta = E_{\gamma,iso}/(E_{\gamma,iso} + E_{KE,iso})$. This efficiency will be useful when trying to further constrain our results.

We numerically calculate the allowed subspace of 4-D parameter space for GRB 090902B by imposing *only two* constraints: (1) the theoretically calculated X-ray flux at 1 keV at 12.5 h, the first X-ray data, must be consistent within 1-σ with the observed value of 0.38 ± 0.10 μJy (Cenko et al. 2010, Pandey et al. 2010) and (2) the injection frequency (ν_i) at this same time should be below the optical band ($\nu_i < 2$ eV) so that the optical light curve decays with time for $t > 12.5$ h.

For the resulting subspace of 4-D parameter space we calculate a few quantities of interest for this GRB. (1) Since we want to address the possibility of the X-ray decay being faster due to a time dependence of the Compton-Y parameter as $(1 + Y_x) \propto t^{0.13}$ (for Option 2: $\nu_i < \nu_{opt} < \nu_c < \nu_x$), we calculate Y_x for electrons radiating at 1 keV at two times, $t_1 = 12.5$ h and $t_2 = 10t_2$, which we define as $Y_{x,1}$ and $Y_{x,2}$, respectively. These times span almost the entire duration of the X-ray observations for GRB 090902B. Steepening the X-ray light curve to the observed value would require $\log_{10}[(1 + Y_{x,2})/(1 + Y_{x,1})] = 0.13$. (2) We calculate the synchrotron cooling frequency at t_1 to see if it is consistent with the orderings considered above, that is, $\nu_{opt} < \nu_c < \nu_x$. (3) We calculate the optical flux at 21 h, which we compare to the observed value of 12.0 ± 0.1 μJy (Pandey et al. 2010). (4) The radio flux at 8.46 GHz is also calculated at 5.6 d, and it is compared to the observed value of 130 ± 34 μJy detected by the Very Large Array (Cenko et al. 2010). (5) We calculate the Compton-Y parameter for electrons radiating at $\lesssim 2$ eV (optical), Y_o, at t_1 and t_2, to see if Y_o and Y_x behave differently or not. The results of our numerical calculation are shown in Figure 4.3.
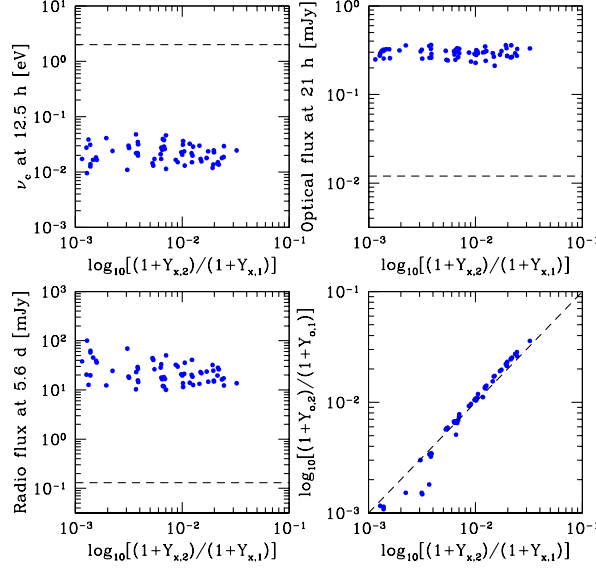
Figure 4.3: We solve for the allowed 4-D external forward shock parameter space for constant CSM and $p = 2.3$ (ϵ_e, ϵ_B, n, $E_{KE,iso}$) by imposing only two constraints: (i) The X-ray flux at $t_1 = 12.5$ h should be consistent with the observed value and (ii) the injection frequency, ν_i, should be < 2 eV at the same time (see text). For this allowed parameter space we calculate (blue points) the cooling frequency at t_1 (top left), the optical flux at 21 h (top right), the radio flux at 5.6 d (bottom left) and the Compton-Y for electrons radiating at 2 eV, Y_o (bottom right). All quantities are plotted as a function of the ratio of Compton-Y for electrons radiating at 1 keV, Y_x, at two times, t_1 and $t_2 = 10t_1$, with subscripts "1" and "2", respectively. We *only* plot the data for which $(1+Y_x)$ increases with time. In order to steepen the X-ray light curve for GRB 090902B, with $\nu_i < \nu_{opt} < \nu_c < \nu_x$ (Option 2), to make it consistent with the observed behavior requires $\log_{10}[(1 + Y_{x,2})/(1 + Y_{x,1})] = 0.13$, which is not found for any point in the 4-D parameter space. Also, we find $\nu_c < 2$ eV, inconsistent with Option 2 (the horizontal dashed line shows $\nu_c = 2$ eV – top left). Moreover, the optical and radio fluxes are inconsistent with the observed values (horizontal dashed lines). The bottom right panel shows that $(1 + Y_x) \propto (1 + Y_o)$, and therefore whenever the X-ray light curve is steepened due to the increase of Y_x with time, the optical light curve is also steepened by the same amount.

96

As can be seen from Figure 4.3, no part of the parameter space reaches the desired value of $\log_{10}[(1 + Y_{x,2})/(1 + Y_{x,1})] = 0.13$. The maximum value reached is $\log_{10}[(1 + Y_{x,2})/(1 + Y_{x,1})] \sim 0.03$, which means that the X-ray decay would only steepen at most to $t^{-1.26}$, which is inconsistent with the observed value by more than 3-σ. Moreover, the optical and radio fluxes are inconsistent with the observed values by a factor of ~ 20 and ~ 100, respectively (Fig. 4.3). More importantly, we also find that ν_c at 12.5 h is actually below the optical band, which is inconsistent with the frequency ordering we are considering here (see Fig. 4.3). All these issues rule out the possibility that the temporal evolution of Compton-Y can explain the observed X-ray data.

In Option 1, the optical and X-ray bands are below ν_c, and thus the fluxes in these bands do not depend on Compton-Y – see equation (4.1). For this reason the temporal evolution of Compton-Y cannot be invoked in this case to reconcile the difference between the data and the expectation of the external forward shock model.

Let us now explore Option 3, where both optical and X-ray bands lie above the cooling frequency, therefore the fluxes in both bands in this case depend on Compton-Y. For $p = 1.5$, the optical flux would decay as $\propto t^{-(3p+10)/16}\nu^{-p/2} = t^{-0.91}\nu^{-0.75}$ and both the optical spectrum and optical decay index are consistent with the observed values within 1-σ. The X-ray decay then, must be steepened by $t^{-0.45}$ to match the observed value, therefore, we check to see if $(1 + Y_x) \propto t^{0.45}$ is allowed by a subset of the 4-D parameter space. Moreover, $(1 + Y_o)$ should evolve very slowly with time, otherwise the optical light curve would *also* steepen and that would be inconsistent with the observed optical data.

Our numerical code is unable to handle $p < 2$, thus we cannot calculate

the allowed parameter space for $p = 1.5$. However, we can run our code for $p = 2.05$ and compare our results with $p = 2.3$. We impose the same two observational constraints as before. For $p = 2.05$ we find that the magnitude of $\log_{10}[(1 + Y_{x,2})/(1 + Y_{x,1})]$ remains roughly the same as it is for $p = 2.3$; however, $\log_{10}[(1 + Y_{o,2})/(1 + Y_{o,1})]$ increases by a constant factor of ~ 2. This means that $(1 + Y_o)$ increases with time faster than $(1 + Y_x)$. We expect this behavior to continue when we decrease the value of p to $p = 1.5$ (there is no reason for an abrupt change when p falls below 2) therefore, the effect of Inverse Compton cooling on the electron energy distribution in this case is to steepen the optical light curve more than the X-ray light curve. This suggests that the temporal evolution of Compton-Y in Option 3 to explain the observed data can be also ruled out.

4.4.1 What is the real solution?

If the X-ray, optical and radio data are consistent with the external forward shock model predictions, then we should be able to find a subset of the 4-D parameter space for which the optical and radio fluxes agree with the observed values (the X-ray flux agrees with the observed value by design). Although we just found out that this subspace does not exist when we require $(1 + Y_x)$ to increase with time (see Figure 4.3), this subspace does exist when $(1 + Y_x)$ *decreases* with time (not plotted in Figure 4.3).

We take now the result of the parameter search in the previous subsection and further constrain it with the following conditions: (i) The external forward shock optical flux at 21 h should be consistent with the observed value within 1-σ, and (ii) the external forward shock radio flux at 5.6 d should be consistent with the observed value within 1-σ. This gives us a subspace

of 4-D parameter space for which the X-ray, optical and radio fluxes as predicted by the synchrotron process in the external forward shock agree with the observed values within 1-σ. We show this subspace projected on the ϵ_B-n plane in Figure 4.4 and we show ν_c at 12.5 h as a function of $E_{KE,iso}/E_{\gamma,iso}$. We compare our result of ϵ_B with the expectation of a magnetic field that is shock-compressed CSM field with pre-shocked value of B_0. The value of ϵ_B downstream of the shock-front resulting from the shock compressed CSM field is $\epsilon_B \approx B_0{}^2/(2\pi n m_p c^2)$, where m_p is the proton mass and $n m_p$ is the CSM mass density. As shown in Fig. 4.4, $B_0 \sim 10~\mu$G can explain all the afterglow radiation without the need for a strong dynamo amplification of shock compressed field.

We find that ν_c at 12.5 h is always $\gtrsim 1$ keV. Note that $\nu_c \sim 1$ keV – within a factor of ~ 3 – only for $E_{KE,iso}/E_{\gamma,iso} \lesssim 0.06$, which would require an extremely high efficiency of $\gtrsim 95\%$ in producing the prompt gamma-rays. The overwhelming majority of the parameter space agrees very well with the expectations of Option 1, that is, ν_c is above 1 keV at 12.5 h. However, how do we reconcile the different temporal decay indices of the X-ray and optical light curves? This is addressed below.

4.4.2   Curvature in the injected electron spectrum

The only option left to explore is the possibility that the spectrum of injected electrons exhibits some curvature, that is, that the value of p is not the same for all observed bands, but that it is a function of electron energy. In this scenario, we allow p to vary and determine the best p values – the ones that give us the best agreement within the observed uncertainties – which are consistent with: (i) the observed optical spectrum and temporal decay (p_{opt}),
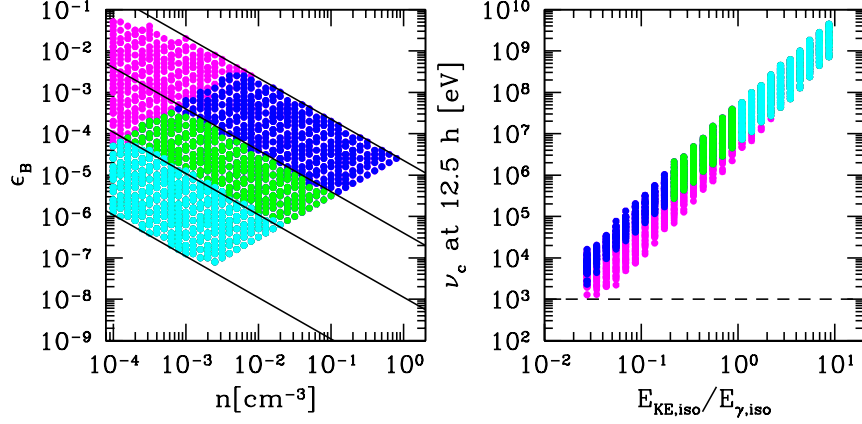
Figure 4.4: Allowed ϵ_B-n plane and ν_c at 12.5 h as a function of $E_{KE,iso}/E_{\gamma,iso}$ (left and right panels, respectively) for constant CSM and $p = 2.3$ when the X-ray, optical and radio fluxes predicted by the external forward shock model at 12.5 h, 21 h and 5.6 d, respectively, are consistent with the observed values within 1-σ (Constraint 1). We further narrow down the allowed parameter space with the following constraints: $\epsilon_e > 0.2$ (Constraint 2 - see Section 4.5), $E_{KE,iso}/E_{\gamma,iso} > 0.2$ (Constraint 3) and $E_{KE,iso}/E_{\gamma,iso} > 1$ (Constraint 4). The points are color coded according to the applied constraints (in parenthesis): magenta (1), blue (1 and 2), green (1, 2 and 3) and cyan (1, 2 and 4). The solid black lines show the expectations for the shock-compressed magnetic field of seed values 1, 10, 60 and 450 μG (from bottom to top – see text). The horizontal dashed line shows $\nu_c = 1$ keV. The injection frequency at 12.5 h is $\nu_i \sim 0.04$ eV. Notice that these figures have many more points than the ones on Figure 4.3, since there are many more solutions for which $(1 + Y_x)$ decreases with time. For the points in these figures, we find that, at most, $(1 + Y_x) \propto t^{-0.2}$, however, as seen in the right panel, $\nu_x < \nu_c$, therefore, the X-ray temporal decay index is unaffected.

and (ii) consistent with the observed X-ray spectrum and temporal decay (p_x).

We will consider the only viable option we have found – $\nu_i < \nu_{opt} < \nu_x < \nu_c$ (Option 1) – and calculate the required values of p from the data. From the observed α_{opt} and β_{opt}, we find that $p_{opt} = 2.3$ would consistently explain the optical data to within 2-σ, and for the observed values of α_x and β_x we find that $p_x = 2.8$ would consistently explain the optical data to within 1-σ.

If $\nu_i < \nu_{opt} < \nu_c < \nu_x$ (Option 2), then the values of p_{opt} and p_x that best fit the data are $p_{opt} = 2.3$ (to within 2-σ) and $p_x = 2.5$ (to within 3-σ). On the other hand, if $\nu_i < \nu_c < \nu_{opt} < \nu_x$ (Option 3), then the values of p_{opt} and p_x that best fit the data are $p_{opt} = 1.5$ (to within 1-σ) and $p_x = 2.5$ (to within 3-σ). Requiring a change in p in Option 3 from $p_{opt} = 1.5$ to $p_x = 2.5$ seems unlikely, since this change is exactly the change one expects due to the cooling frequency, which for Option 3 should be below the optical band. Moreover, the X-ray data only agrees within 3-σ. For these two reasons, we rule out Option 3. It might seem that Option 2 provides a good solution, since $p_{opt} \approx p_x$, however, according to Figure 4.4, for $p = 2.3$ ($p_{opt} = p_x$) there is no parameter space where $\nu_c < \nu_x$. If we repeat the calculation for $p = 2.4$, which is an average of p_{opt} and p_x in Option 2, we find that Figure 4.4 is basically unchanged. For this reason, we rule out the possibility that Option 2 with a curvature in the electron distribution function can explain the observed data. Therefore, Option 1 is the only viable solution for the afterglow data of GRB 090902B.

In conclusion, we find that the external forward shock model can explain the afterglow data for GRB 090902B provided that the cooling frequency (ν_c) is larger than 1 keV at ~ 0.5 d and $\nu_i < 2$ eV. We also find that in order

101

to explain the different temporal decay indices of the optical and X-ray light curves, there must be a slight curvature in the electron energy distribution function, where the spectrum of injected electrons steepens from $\propto \gamma_e^{-2.3}$ to $\propto \gamma_e^{-2.8}$, when γ_e increases by a factor of ~ 30, corresponding to electron synchrotron frequency increasing from optical to ~ 1 keV. This happens effectively at a LF which corresponds to synchrotron frequency ν_b. The energy spectrum below (above) ν_b should be $\propto \nu^{-0.65}$ ($\propto \nu^{-0.9}$) and the light curves should decay as $\propto t^{-0.98}$ ($\propto t^{-1.36}$). In the next section we determine this break frequency (ν_b), although, one should keep in mind that this break might not be sudden but is probably gradual.

4.4.2.1   Break frequency

Using the X-ray and optical data at a specific time, we can determine the effective break frequency necessary to explain the observations. At 21 h, the optical flux (2 eV) is 12 μJy and the X-ray flux (at 1 keV) is 0.2 μJy (Pandey et al. 2010). At this time, one can show that a single power-law spectrum with $\nu^{-0.65}$ reconciles these two fluxes, which means that ν_b should be very close to 1 keV. We estimate ν_b at 21 h and find that it should be at 650 eV (this validates the calculation of the parameter space shown in Figure 4.4: at 21 h the curvature of the spectrum is just starting to be evident in the X-ray data). One expects ν_b to decrease with time, therefore, the evidence for the proposed curvature in the spectrum should become stronger with time.

We use the combined spectrum presented in Pandey et al. (2010) fig. 2 at 1.9 d to determine the location of ν_b at later times. The optical flux (2 eV) at this time is 7 μJy and the X-ray flux (at 2.88 keV) is 0.03 μJy. Again, assuming that the spectrum below (above) ν_b is $\nu^{-0.65}$ ($\nu^{-0.9}$), we can

determine ν_b to be ≈ 160 eV. The values of ν_b at 21 h and 1.9 d allow us to find that it decreases with time as $\sim t^{-1.8}$, which is roughly the same time dependence as ν_i, which exhibits $\nu_i \propto t^{-1.5}$.

At the beginning of the *Swift* XRT observations at 12.5 h, we therefore expect ν_b to be ~ 1.6 keV, and at 1.3 d, we expect ν_b to be ~ 0.3 keV, which is the lower bound of the XRT energy range. Therefore, there should be a small difference in the spectrum and light curves between the $0.3 - 1.5$ keV and $1.5 - 10$ keV bands during 12.5 h to about 1.3 d if our interpretation that there is some curvature in the spectrum is correct.

4.5   Early high energy data

Using the parameter space we have obtained in Section 4.4.1 from late times radio, optical and X-ray data, we can calculate the external forward shock flux at high energies (*Fermi*/LAT band) at early times. We choose to calculate the flux at 50 s and at 100 MeV. If the LAT emission has an external forward shock origin, then this flux should be consistent with the observed value of 220 nJy (Abdo et al. 2009d). On the other hand, the GBM band flux (~ 100 keV) is dominated by the typical prompt variable source, whose origin remains uncertain; this emission lasts for ~ 30 s and then it exhibits a sharp decay in the flux. The external forward shock emission at 100 keV and 50 s should be smaller than the observed 100 keV flux, which is ~ 0.4 mJy (Abdo et al. 2009d), so that the external forward shock flux does not prevent the observed flux to decay very rapidly ($\propto t^{-3}$) as it is observed.

The calculation of the external forward shock emission at early times is not straightforward, since we find that the spectrum of injected electrons has a curvature. This should be taken into account when extrapolating from

103
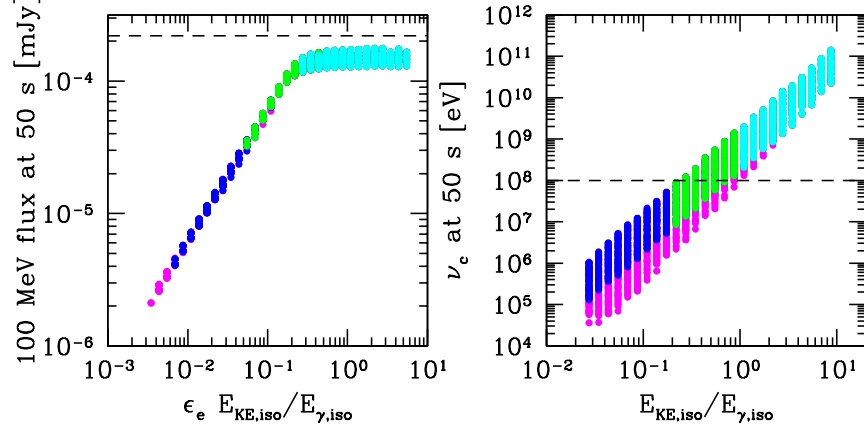
Figure 4.5: 100 MeV flux as a function of $\epsilon_e E_{KE,iso}/E_{\gamma,iso}$ and ν_c at 50 s as a function of $E_{KE,iso}/E_{\gamma,iso}$ in the left and right panels, respectively (for $p = 2.3$). The dashed lines indicate the observed flux at 50 s and $\nu_c = 100$ MeV, respectively. The injection frequency at 50 s is $\nu_i \sim 1$ keV (2 keV) for $p = 2.3$ ($p = 2.55$). The color coding is the same as in Figure 4.4.

about a day to a few tens of seconds. Using the estimated evolution of ν_b as $\propto t^{-1.8}$ (Section 4.4.2.1), one finds that ν_b is ~ 300 MeV at 50 s. However, the temporal evolution of ν_b is highly uncertain and we do not know if it monotonically extends to very early times. For this reason, we use two different values of p when extrapolating from ~ 1 d to 50 s: $p = 2.3$, consistent with the p used before and $p = 2.55$, which is the average of p_{opt} and p_x obtained in Section 4.4.2. The results of these calculations are presented in Figure 4.5.

We find a large range of values for the external forward shock flux at 100 MeV and 50 s and plot this flux against $\epsilon_e E_{KE,iso}/E_{\gamma,iso}$; we choose this parameter because the flux above ν_c is roughly proportional to $\epsilon_e E_{KE,iso}$ (see eq. 4.1) and we normalize $E_{KE,iso}$ to $E_{\gamma,iso}$. Taking $\epsilon_e > 0.2$ as found for

many GRB afterglows by Panaitescu & Kumar (2001) and $E_{KE,iso}/E_{\gamma,iso} > 1$ (so that $\eta < 0.5$), suggests that $\epsilon_e E_{KE,iso}/E_{\gamma,iso} > 0.2$, and in that case the calculated 100 MeV flux is consistent with the observed value to within a factor of 1.4 (for $p = 2.3$). For $p = 2.55$ and $\epsilon_e E_{KE,iso}/E_{\gamma,iso} > 0.2$ the 100 keV flux at 50 s is similar to the one obtained for $p = 2.3$ only shifted downwards by a constant factor of 2.5, therefore, it is smaller than the observed value by a factor of ~ 3. This is a remarkable agreement given the fact that we have extrapolated the afterglow data from ~ 1 d to 50 s, and from radio, optical and X-ray to 100 MeV.

It is also important to know the location of the cooling frequency at 50 s, which would allow us to determine the spectrum and temporal decay index of the > 100 MeV light curve. For both values of p, the cooling frequency is identical, and we plot it as a function of $E_{KE,iso}/E_{\gamma,iso}$ in Figure 4.5. We can see that for $E_{KE,iso}/E_{\gamma,iso} > 1$, 100 MeV $\lesssim \nu_c \lesssim 100$ GeV at 50 s, therefore, one expects three possibilities: (i) $\nu_c \sim 100$ MeV and it will very shortly fall below the 100 MeV band, and the > 100 MeV spectrum in this case should be consistent with being $\propto \nu^{-p/2}$, (ii) ν_c is much higher than 100 MeV and will thus remain above it until 10^3 s, which marks the end of the LAT observations and (iii) $\nu_c > 100$ MeV and it will cross the 100 MeV band during the observations. For (i), the 100 MeV light curve would be $f_\nu \propto t^{-1.23}\nu^{-1.15}$ for $p = 2.3$ or $f_\nu \propto t^{-1.4}\nu^{-1.23}$ for $p = 2.55$. For (ii) the 100 MeV light curve would be $f_\nu \propto t^{-0.98}\nu^{-0.65}$ for $p = 2.3$ or $f_\nu \propto t^{-1.16}\nu^{-0.78}$ for $p = 2.55$, and, lastly, for (iii) the light curve will transition from (i) to (ii).

The observed $0.1 - 300$ GeV light curve for GRB 090902B decayed as $t^{-1.5\pm0.1}\nu^{-1.1\pm0.1}$ in the time interval $25 - 1000$ s (Abdo et al. 2009d). This light curve could be explained by scenario (i) above, for $p = 2.55$, within

1-σ. This agrees nicely with the results shown in Figure 4.4; one can see that the 100 MeV flux increases almost linearly with $\epsilon_e E_{KE,iso}$ as expected for $\nu_c < 100$ MeV and then reaches a plateau. The reason for this plateau is that it corresponds to $\nu_c \gtrsim 100$ MeV at 50 s, and the flux below ν_c has already been precisely fixed by the X-ray flux at 12.5 h (one of the constraints), therefore, the 100 MeV flux would also be fixed precisely. Shortly after 50 s, the > 100 MeV spectrum is consistent with being above ν_c as suggested by the data. Scenario (ii) above can be ruled out, because the LAT light curve decreases faster than predicted and also the predicted spectrum is too shallow compared with the observed one. Finally, scenario (iii) can also be ruled out, since a break in the LAT light curve was not detected in the data for GRB 090902B (Abdo et al. 2009d). It is worth mentioning that there is a small steepening of the > 100 MeV light curve by, at most, $\sim t^{-0.03}$ when $\nu_c < 100$ MeV, due to the increase of $(1 + Y)$ for electrons radiating at 100 MeV.

The flux from the external forward shock at 100 keV, which decays as $\sim t^{-1}$ would dominate the observed 100 keV light curve and prevent it from decaying quickly as it is observed ($\sim t^{-3}$) unless the external shock contribution to the 100 keV flux is much smaller than the observed flux. To check this, we calculate the external forward shock flux at 100 keV and 50 s and find it to be ~ 0.01 mJy (for both p values), which is a factor of ~ 40 smaller than the observed value. This allows the observed prompt 100 keV flux to decay rapidly as observed.

4.6 The additional power-law component extending to 10 keV

The GRB 090902B spectrum at early times displays a Band function in the sub-MeV energy range. Time-resolved spectral analysis also shows a significant power-law component that appears to extend from the GeV range to the lowest energies (~ 10 keV) and it is more intense than the Band function both for photon energy $\lesssim 50$ keV and > 100 MeV (Abdo et al. 2009d). The Band function is usually associated with the prompt emission and its origin remains uncertain. We address here the question whether the extra power-law component in the spectrum could have an external forward shock origin. We do this at 7 s, which is the midpoint of interval b in the analysis of Abdo et al. (2009), where the power-law contribution is best constrained and its spectrum is $\beta = 0.94 \pm 0.02$. The observed flux at 10 keV and 7 s is ~ 12 mJy.

For the external shock origin of the power-law component at 7 s, the injection frequency should be below ~ 10 keV and the cooling frequency should be above the highest photon energy detected at that time, which is a few GeV. Using the same procedure as in the last section we calculate ν_i, ν_c and the flux at 10 keV at 7 s[1]. We find that the injection frequency has a very narrow range of allowed values, $\nu_i \sim 20$ keV and $\nu_i \sim 40$ keV for $p = 2.3$ and $p = 2.55$, respectively. The cooling frequencies at 7 s for $p = 2.3$ and $p = 2.55$ are identical and are just a factor of $(50/7)^{1/2} \sim 2.7$ higher than the value at 50 s (see Figure 4.5), that is, 300 MeV $\lesssim \nu_c \lesssim 300$ GeV at 7 s for $E_{KE,iso}/E_{\gamma,iso} > 1$. However, ν_c at 7 s cannot be larger than a few GeV, otherwise it will stay above

---

[1]Note that the > 100 MeV light curve starts decaying at ~ 10 s, which might correspond to the beginning of the deceleration phase of the external forward shock, however, extrapolating back to 7 s does not introduce a significant error.

100 MeV for the entire duration of the LAT emission, which is inconsistent with the observed spectrum during this period. In addition, the expected spectrum between ν_i and ν_c would be $\beta = 0.65$ and $\beta = 0.78$ for $p = 2.3$ and $p = 2.55$, respectively, which is inconsistent with the observed value. Finally, the expected flux at 10 keV and 7 s lies in a very narrow range, and it is ~ 0.5 mJy (for both p values), which is a factor of ~ 20 smaller than the observed value. All these arguments suggest that the power-law detected in addition to the Band spectrum at early times is unlikely produced by the external shock, at least in the simplest version of this model.

4.7   Discussion

In this chapter we have considered the late afterglow data of GRB 090902B in the context of the external forward shock model. The optical data is entirely consistent with this model. However, the X-ray flux decays faster than expected for the observed X-ray spectrum. We consider three possibilities that could have steepened the X-ray light curve falloff.

First, we considered radiative losses or evolving microphysical parameters that might steepen the X-ray flux. However, since the optical and X-ray fluxes have very similar dependence on these parameters, it is not possible to steepen the X-ray light curve and at the same time not steepen the optical light curve, that is, obtain a solution consistent with the observations. Second, we carried out a very detailed calculation of the Compton-Y parameter in hopes that its increase with time could steepen the X-ray data if the cooling frequency is below the X-ray band. However, we find that its effect on the steepening of the light curve is extremely small and unable to explain the observed data.

Another modification of the standard external forward shock model we considered is the possibility that the spectrum of injected electrons at the shock front is not a single power-law, but that it exhibits some curvature. We find that this is the only modification that can reconcile the theoretical expectations with the afterglow data of GRB 090902B.

The curvature we find in the spectrum of injected electrons might not be able to be ruled out with the resolution and uncertainties in the most recent particle-in-cell simulations of particle acceleration in relativistic collisionless shocks (Sironi & Spitkovsky 2011). Simulations need to be able to run for longer to achieve time-scales and energy range relevant to the GRB afterglow. Future simulations should be able to explore our claim of the presence of curvature in the electron energy distribution. The slight curvature, invoked phenomenologically, is tied to the physics of particle acceleration, which suggests in this case that the higher energy electrons – those radiating X-rays – are accelerated slightly less efficiently than those radiating optical photons. The fact that we find a "downward" curvature ($p_x > p_{opt}$) is reassuring, since the opposite would have been contrived.

The synchrotron frequency that corresponds to the electrons Lorentz factor at which the spectrum curves should be at ~ 1.6 keV at the beginning of the *Swift*/XRT observations.

The break frequency decreases with time as $\sim t^{-1.8}$ and it falls below the XRT band at about ~ 1.3 d (Section 4.4.2.1). An inspection of the 0.3-1.5 keV XRT light curve shows a slight flattening during this time in this light curve compared to the 1.5-10 keV one, just as predicted (Evans et al. 2007). A careful analysis of the XRT data shows that the 0.3-1.5 keV data are well fit by a broken power-law as predicted, but the presence of this break in the light

curve cannot be claimed with high statistical significance; the predictions of this model however cannot be ruled out due to the sparseness of the data and the fact that the theoretical decay slopes before and after the break ($t^{-0.98}$ and $t^{-1.36}$) are very similar (Margutti, personal communication). Similarly, the possible break in the spectrum cannot be found since the errors in the spectrum are on the order of the difference between the two different indices (before and after the break) that one expects.

This work assumes that the late afterglow in all bands is produced by the same population of electrons. Can we abandon this scenario and invoke one in which, for example, the X-ray and optical data are produced by two different sources? It seems unlikely. We discuss this below.

Let us start with the assumption that the X-ray flux is originated in the external forward shock, that is, by the interaction of the GRB jet with the CSM. The optical data might have another origin. However, since the optical flux decays as a single power-law for a long period of time, its origin is also some form of an external shock. This external shock does not have to necessarily be the same one that produced the X-ray afterglow. It could be, for instance, that a lower LF cocoon material interacts with the CSM and drives an external shock which produced the optical radiation. As can be seen in Section 4.4.2.1, the optical and the X-ray fluxes close to 1 d fall on a single power-law spectrum which is roughly consistent with the observed optical and X-ray spectra. If we assume that for these two shocks ϵ_e, ϵ_B, and n are approximately equal, then $E_{KE,iso}$ should also be the same. Why should $E_{KE,iso}$ for the two different and unrelated sources be the same? For this reason, we think that this possibility is contrived and suggest the same origin for both X-ray and optical photons.

Even if X-ray and optical photons are produced by the same population of electrons: Could it be that optical (and radio) photons are produced via synchrotron while X-ray photons originate via Inverse Compton radiation scattering of synchrotron photons? This interesting possibility can be ruled out. At ~ 1 d, if we extrapolate the optical flux using optical spectrum to radio band we overestimate the observed radio flux by a factor of ~ 700. This means that there is a break in the spectrum, which would correspond to ν_i, at $\sim 10^{-2}$ eV. At this frequency, the peak synchrotron flux is ~ 1 mJy. The optical depth to Thompson scattering in the external forward shock at ~ 1 d is $\tau_e \sim \sigma_T nR \sim 10^{-7}$, while the ratio of X-ray flux to the peak synchrotron flux at the same time is $\sim 10^{-4}$. Therefore, this possibility can be safely ruled out since the X-ray flux is at least 10^3 times larger than the maximum expected flux for the synchrotron-self-Inverse Compton process.

We have also found that when we constrain the X-ray, optical and radio fluxes at ~ 1 d one finds a large allowed range for ϵ_B. When we further constrain $\epsilon_e > 0.2$, as found by Panaitescu & Kumar (2001) and take the isotropic kinetic energy in the blast wave to be larger than the isotropic radiated gamma-ray energy during the prompt phase ($E_{KE,iso} > E_{\gamma,iso}$), then the magnetic field in the source is consistent with being produced via shock-compressed CSM field as shown in Figure 4.4 and suggested by Kumar & Barniol Duran (2009, 2010), Barniol Duran & Kumar (2010). The required seed field – the upstream field – before compression is $\lesssim 10\mu$G. The constraint $E_{KE,iso} > E_{\gamma,iso}$ is applied in order to avoid a radiative efficiency larger than 50%; however, even when we take $E_{KE,iso} > E_{\gamma,iso}/5$ – corresponding to a radiative efficiency of 80% – we still find that the shock compression scenario holds with just a slightly larger seed field of $\lesssim 60\mu$G (see Figure 4.4).

To obtain the region of ϵ_B-n plane allowed by the GRB 090902B data we have used the X-ray, optical and radio fluxes at $\gtrsim 1$ d, since the external reverse shock might dominate the optical data until ~ 0.7 d (see fig. 1 of Pandey et al. 2010). There is the possibility, however, that the radio flux at ~ 1 d might still be dominated by the external reverse shock, since the external reverse shock at the radio band might decay slower than at the optical band. This is the reason why we have obtained the ϵ_B-n plane using the radio flux at 5.6 d (Cenko et al. 2010). We expect that at this time the contribution from the reverse shock to the radio flux is negligible. Nevertheless, if instead of using the radio flux at 5.6 d we use the radio flux measured at 1.3 d at the Westerbork Synthesis Radio Telescope (van der Horst et al. 2009), we find that our general results are not modified: the requirements for the magnetic field are the same; however, the density increases by a factor of ~ 10; points shown in Figure 4.4 are shifted to the right by a factor of ~ 10 along the diagonal bands in this case.

4.7.1 Electron acceleration and the upstream magnetic field

Recently, the detection of 100 MeV photons up to $\sim 10^3$ s in *Fermi* GRBs has been used to calculate a lower limit on the upstream CSM field by requiring that the Inverse Compton loss timescale is larger than the acceleration timescale of electrons radiating at 100 MeV (Li 2010). For the subspace of 4-D parameter space (ϵ_e, ϵ_B, n, $E_{KE,iso}$) consistent with the data for GRB 090902B (Section 4.4.1) we calculate Compton-Y for electrons radiating at 100 MeV at 10^3 s (using $p = 2.3$), and use that to determine a lower limit to the upstream field (Figure 4.6). We calculate another lower limit to the upstream field by requiring that electrons radiating in the LAT band are confined to

the shock front (Piran & Nakar 2010, Barniol Duran & Kumar 2011a); we determine this lower limit for electrons radiating at 100 MeV and 10^3 s (see equation (3) in Barniol Duran & Kumar 2011a). The true lower limit to the upstream magnetic field is taken to be the larger of these two limits and the result is shown in Figure 4.6. We find that for GRB 090902B the electron confinement requirement gives a larger upstream field for much of the allowed parameter space, and an upstream field of $\sim 5\mu$G is sufficient to confine electrons producing 100 MeV radiation and to avoid excessive Inverse Compton losses while electrons are traveling upstream of the shock front.

The lower limit on the upstream CSM magnetic field we find is much smaller than the one found by Li (2010). This discrepancy arises mainly because of the difference between the calculation of Inverse Compton loss – Li (2010) used a simplified analytical calculation for Inverse Compton loss whereas we have carried out an almost exact calculation numerically as described in Section 4.3.2.1.

We note that the ϵ_B-n parameter space shown in Figure 4.4 should be slightly revised to reflect our findings in Figure 4.6; results in Figure 4.4 did not include the constraints on magnetic field due to electron acceleration arguments. However, the modification to the lower limit of the CSM field in the ϵ_B-n parameter space is very small, and it is non-existent for the case when $E_{KE,iso} > E_{\gamma,iso}$.

4.8 Conclusions

We have analyzed the late time afterglow X-ray, optical and radio data for GRB 090902B in the context of the synchrotron radiation mechanism in the external forward shock model. We find that a curvature in the power-
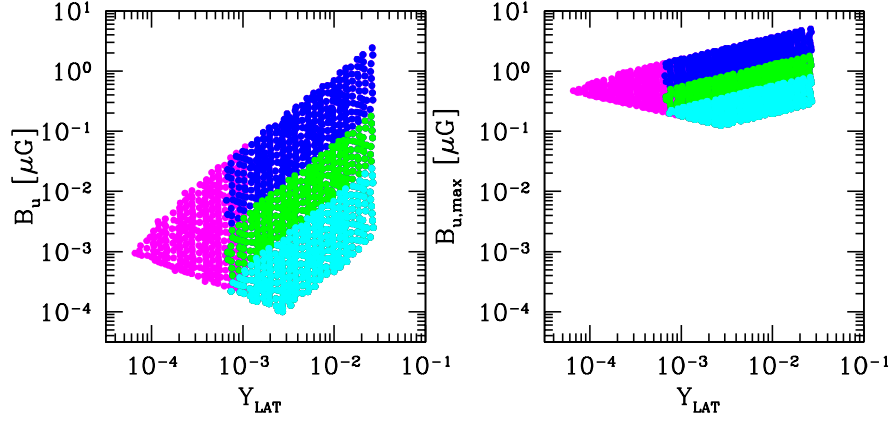
Figure 4.6: Lower limit on the upstream circumstellar medium magnetic field, B_u, as a function of the Compton-Y parameter for electrons radiating at 100 MeV at 10^3 s, Y_{LAT} (left panel). Y_{LAT} is calculated using the method described in Section 4.3 for the allowed subspace of the 4-D parameter space (ϵ_e, ϵ_B, n, $E_{KE,iso}$) for GRB 090902B afterglow data shown in Figure 4.4 (for $p = 2.3$). B_u was obtained by requiring that the Inverse Compton cooling time for these electrons is larger than their acceleration timescale: Method 1. We also calculate a lower limit on B_u by requiring that the electrons radiating at 100 MeV at 10^3 s are confined to the shock front: Method 2 (B_u obtained by this method does not depend on Y_{LAT} and has an extremely weak time dependence). The maximum of these two values, $B_{u,max}$, is the true minimum of B_u, which for GRB 090902B is given by Method 2 (right panel) and it is plotted as a function of Y_{LAT} to aid in the comparison between the two panels; $B_{u,max} \lesssim 5$ μG. The color coding is the same as in Figure 4.4.

law electron energy distribution is needed in order to provide a good fit to the late time optical and X-ray data; radiation losses, varying microphysical parameters and an increase in Inverse Compton losses all fail to explain the observed data. The late time afterglow fit gives an ϵ_B (fraction of total energy in the shock imparted to magnetic fields) consistent with shock-compressed circumstellar medium magnetic field of $\lesssim 10$ μG and $\lesssim 60$ μG if we take the efficiency for producing gamma-rays to be $\sim 50\%$ and $\sim 80\%$, respectively.

Particle acceleration in the external forward shock allows us to set a lower limit on the upstream circumstellar medium magnetic field. We find that the field strength in the unshocked medium in the vicinity of GRB 090902B must be at least 2 μG in order to produce 100 MeV photons at $50\text{ s} \lesssim t \lesssim 10^3$ s (Barniol Duran & Kumar 2011a).

The calculation presented in this chapter represents an improvement in our previous afterglow modeling due to a more precise calculation of Inverse Compton losses. Here, we include Klein-Nishina effects and also relativistic corrections of the outgoing energy of the Inverse Compton scattered photons. We also calculate the electron energy distribution self-consistently by determining the synchrotron emission and using it to determine the Inverse Compton losses, which in turn modify the electron energy distribution.

The flux calculated at 100 MeV at 50 s using the external forward shock parameters obtained from the late afterglow data is consistent with the *Fermi*/LAT data, confirming our previous claims (Kumar & Barniol Duran 2009, 2010). We also calculated the expected external forward shock at 100 keV and 50 s. At this time, the observed 100 keV light curve is undergoing a fast decay ($\sim t^{-3}$). We find that the external forward shock at 100 keV and 50 s is smaller than the observed value by a factor of ~ 40, easily allowing the

observed light curve to decay quickly (confirming our earlier results in Kumar & Barniol Duran 2010). We speculate that for some small fraction of GRBs this steep decay will not be seen, instead, one will see a smooth slowly decaying $(\sim t^{-1})$ light curve emerge after the main prompt, variable, emission is over.

We find that the cooling frequency at ~ 50 s is ~ 100 MeV for GRB 090902B. If this is correct, one should be able to track the cooling frequency as it passes through the LAT band at earlier times ($\nu_c \propto t^{-1/2}$). A presence of this behavior in the data of this and other LAT detected GRBs would help confirm an external shock origin for the LAT emission.

Finally, the prompt spectrum of GRB 090902B contains a power-law component in addition to the usual Band function. We argue against the external shock origin of the extra power-law component at 7 s (Section 4.6).

Chapter 5

Adiabatic expansion, early X-ray data and the central engine in GRBs

5.1 Introduction

The central engine of GRBs is hidden to direct observations and its workings are largely unknown. The only information that we currently have about the GRB is obtained from its electromagnetic radiation. We have to look for signatures in the radiation mechanism to understand how Nature produces these outbursts.

The *Swift* satellite has provided very early X-ray data that shows that for most bursts there is a very steep decay lasting for about 10 minutes (Tagliaferri et al. 2005, Nousek et al. 2006 - see Zhang et al. 2006 and references therein for possible physical explanations). These observations suggest that the rapidly declining X-ray light curve (LC) and the burst are produced by the same source, because the X-ray LC, when extrapolated backwards in time, matches the gamma-ray LC (O'Brien et al. 2006). Therefore, a natural question arises: Is the early X-ray data really just a rapidly declining continuation of the central engine activity, originally seen in the gamma-ray band, but now seen at lower energy? Or does the central engine switch off abruptly and the early X-ray data does not reflect the activity of the central engine?

If the central engine completely shuts off when the gamma-ray photons' flux falls below the gamma-ray detector sensitivity, then the emission from a

cooling "ember" would be responsible for the early X-ray steep decay. This source - which had just produced the gamma-ray emission - would be cooling by adiabatic expansion (AE). In this chapter, we study the flux properties of a "hot" shell that undergoes AE and cools. The goal is to determine if the observed X-ray steep decay data is consistent with the AE scenario. If so, then the central engine did shut off abruptly right after the gamma-ray emission ceased. On the other hand, if it isn't, then the data is reflecting the rapidly declining activity of the central engine. The reason for this is that any other process that does not invoke central engine activity to explain the early X-ray data has problems explaining the smooth temporal connection observed in the LC between the prompt emission and the early X-ray data.

AE has been studied before to predict the long-wavelength afterglow from GRBs (Mészáros & Rees 1997) and also, the optical flashes from internal and reverse shocks (Mészáros & Rees 1999, Sari & Piran 1999a). In this chapter, we describe the evolution of a collisionless plasma due to AE and show that this is in general different from AE of an ideal gas.

In this chapter, we first present the micro-physics of the AE for a collisionless plasma in Section 5.2. Then, we use it to calculate the flux properties of a source undergoing AE in Section 5.3. We look at what the current observations tell us in Section 5.4, and we put them in the context of the central engine in Section 5.5. We summarize our results and give our conclusions in Section 5.6.

5.2 Micro-physics of the Adiabatic Expansion

For an ideal gas, the pressure evolves due to adiabatic expansion as $P_{ej} \propto \rho^{a_e} \propto V^{-a_e}$, where $a_e = 4/3$ for a relativistic gas and ρ and V are

the co-moving density and ejecta volume, respectively. The collisions between electrons are extremely rare in GRB relativistic shocks, therefore, one needs to be careful in the use of this formula[1].

For a collisionless magnetized plasma, assuming that no collective plasma processes randomize the particles' velocity due to scattering, particles move along a magnetic field line and, by using the concept of *adiabatic invariant* (Jackson 1998, Rybicki & Lightman 1979), we can calculate the particles' energy. This invariant describes that, for slowly varying fields, the magnetic flux through the orbit of the particle is a constant, or $p_\perp^2/B$ is an adiabatic invariant, where $p_\perp$ is the component of the particle's momentum transverse to B, the co-moving magnetic field. For highly relativistic particles, $p_\perp \approx m_e c \gamma_\perp$, so that

$$\gamma_\perp^2/B = \text{constant} \tag{5.1}$$

can be used, where $\gamma_\perp$ is the Lorentz Factor (LF) of the electron in the transverse direction, m_e is the electron's mass and c is the speed of light (from now on, $c = 1$). This relationship can be used because the magnetic field decays on a much larger length-scale than the electron's gyro-radius (see Appendix A).

---

[1]We have estimated the mean free path for Coulomb scattering between a hot electron and a cold electron and find it to be much larger compared to the shell thickness. The electric field associated with a relativistic hot electron is calculated using the Liénard-Wiechert potential, and we find the cross-section for a significant interaction, that is, leading to a fraction of the energy of the hot electron transferred to a cold electron, is close to the Thomson cross section ($\sigma \approx \sigma_T/3$). The mean free path is $\lambda = (n\sigma)^{-1}$, where n is the electron density. From the total energy E, the distance of the shell from the center of explosion R, the source LF Γ, and the co-moving shell width Δ', we find $n = E/(\Gamma m_p c^2 4\pi R^2 \Delta')$. Using the usual notation $Q_n = Q/10^n$, we obtain: $\lambda/\Delta' \approx 700 R_{15}^2 \Gamma_2 E_{52}^{-1}$. For scattering between hot electrons, the conclusion is the same. Therefore, Coulomb scattering between the electrons is not significant.

It is worth noting that the parallel component of the electron's momentum remains unchanged; this will be briefly discussed in the last section.

In the next sections, we will make use of (5.1) to predict the evolution of the electrons' LF in a hot shell that undergoes AE. We will use it to calculate the properties of its synchrotron and synchrotron-self-Compton (SSC) radiation.

5.3 Analytical light curves of an adiabatically cooling ember

Let's assume that the GRB ejecta was heated by some process (shocks or magnetic dissipation) and suddenly the central engine switches off completely. There is no other energy injection mechanism at hand, so it begins to coast (the LF of the ejecta is constant, see Section 5.3.6) and cools via AE. We will calculate the flux properties of this cooling ember.

5.3.1 Ejecta width and magnetic field

In the following subsections we will provide the basic ingredients for the radiation calculation. First, we need to determine the co-moving thickness of the ejecta, which could be:

$$\Delta' = R/\Gamma \qquad \text{or} \qquad \Delta' = \Delta_0.$$

We will call these cases: thin ejecta shell (an ejecta that undergoes significant spreading) and thick ejecta shell (an ejecta that experiences no significant spreading), respectively. The observed time is $t \propto R/\Gamma^2$, where R is the distance of the source from the center of the explosion and Γ is the LF of the

source with respect to the rest frame of the GRB host galaxy.

The magnetic field in the GRB ejecta could be a combination of frozen-in field from the central explosion and field generated locally. We prescribe the decay of the field by using the flux-freezing condition (Panaitescu & Kumar 2004), which gives:

$$B_\perp \propto (R\Delta')^{-1} \qquad \text{and} \qquad B_\parallel \propto R^{-2}.$$

We will use the field that decays slower, although this is highly uncertain. This is because the magnetic field generation mechanism for GRBs is still not well understood, so the relative strength of $B_\perp$ and $B_\parallel$ is unknown.

5.3.2 Electrons' energy distribution

For an adiabatically expanding source, no more energetic electrons are injected in the system when the shock has run its course. This means that, after some time, there will be few electrons with energies higher than the cooling electron LF, γ_c. Therefore, the electron population above γ_c will be truncated due to radiation losses and the emission for $\nu_c < \nu$ will rapidly shut off (ν_c is the synchrotron frequency corresponding to electrons with γ_c). At this point, the electron distribution will follow $\propto \gamma^{-p}$ for $\gamma_i < \gamma < \gamma_c$, where γ_i is the typical LF of the electrons, since we would be dealing only with adiabatic electrons. Moreover, since the radiative cooling quickly becomes less important than the adiabatic cooling because the magnetic field decays rapidly with the expansion of the ejecta, both γ_i and γ_c will evolve in the same way.

For the case $\gamma_c < \gamma_i$, the radiation losses would dominate and, after some time, they would make the whole electron distribution collapse to a value

close to γ_c. A narrower range in the electron distribution would be responsible for the radiation. In this chapter we focus on the $\gamma_i < \gamma_c$ case.

5.3.3 Basics of Synchrotron and SSC

The electrons' four-momentum is given by $P = m_e(\gamma, \gamma \cos \alpha', \gamma \sin \alpha', 0)$, which can be also written as $P = m_e(\gamma, \gamma_{\parallel}, \gamma_{\perp}, 0)$, where $\gamma_{\parallel}$ is the component of the electrons' momentum parallel to B. The pitch angle, which is the angle between B and the velocity of the electrons, is α'. In this notation, the electron's LF is then $\gamma^2 = \gamma_{\parallel}^2 + \gamma_{\perp}^2$. According to the prescription of the adiabatic invariance, $\gamma_{\perp}$ evolves following (5.1) and $\gamma_{\parallel}$ remains unchanged. We assume that at the onset of the adiabatic expansion $\gamma_{\perp} \sim \gamma_{\parallel}$, then quickly when time doubles, the radius would have also doubled, making the magnetic field decrease by at least that factor and reducing $\gamma_{\perp}$ making $\gamma_{\parallel} > \gamma_{\perp}$, which gives:

$$\gamma = \gamma_{\parallel}\sqrt{1 + \frac{\gamma_{\perp}^2}{\gamma_{\parallel}^2}} \approx \gamma_{\parallel} \quad \text{and} \quad \sin \alpha' = \frac{\gamma_{\perp}}{\gamma} \approx \frac{\gamma_{\perp}}{\gamma_{\parallel}}. \tag{5.2}$$

As the transverse component of the momentum decreases, due to the decay of the magnetic field, the pitch angle decreases, which makes the electron's momentum more aligned with the local magnetic field.

Knowing the electrons' energy distribution, the emission at any given frequency and time can be calculated using the synchrotron spectrum:

$$F_{\nu} = F_{\nu_i} \begin{cases} (\nu/\nu_a)^2(\nu_a/\nu_i)^{1/3} & \nu < \nu_a \\ (\nu/\nu_i)^{1/3} & \nu_a < \nu < \nu_i \\ (\nu/\nu_i)^{-(p-1)/2} & \nu_i < \nu < \nu_c, \end{cases} \tag{5.3}$$

for the case $\nu_a < \nu_i < \nu_c$, where ν_a is the self absorption frequency and it is

obtained using equation (52) of Panaitescu & Kumar (2000) (see, e.g., Katz & Piran 1997, Sari & Piran 1999b). The characteristic synchrotron frequencies are obtained from the corresponding electrons LFs:

$$\nu_{i,c} = \frac{eB\gamma_{i,c}^2\Gamma}{2\pi m_e(1+z)}\sin\alpha',\tag{5.4}$$

where $\gamma_{i,c}$ and $\sin\alpha'$ are given by (5.2). The observed peak flux is

$$F_{\nu_i} = \frac{(1+z)\sqrt{3}e^3N_eB\Gamma}{4\pi d_L^2(z)m_e}\sin\alpha',\tag{5.5}$$

where d_L is the luminosity distance, N_e is the number of radiating electrons (which in this scenario is constant), z is the redshift and e is the electron's charge.

For the SSC case, the flux peaks at $\nu_i\gamma_i^2$ with magnitude $\tau_e F_{\nu_i}$, where $\tau_e = N_e\sigma_T/(4\pi R^2)$ is the optical depth to electron scattering. We will calculate SSC emission for photons above ν_a. We will use the same synchrotron piecewise spectrum, which is just a very crude approximation.

5.3.4 Temporal and spectral properties

For synchrotron emission of a cooling ember undergoing AE, we find:

$$F_{\nu_i} \propto t^{-3}(t^{-3/2}), \quad \nu_{i,c} \propto t^{-3}(t^{-3/2}), \quad \nu_a \propto t^{-12/5}(t^{-9/5})\tag{5.6}$$

and

$$F_\nu \propto \begin{cases} t^2(t^2)\nu^2 & \nu < \nu_a \\ t^{-2}(t^{-1})\nu^{1/3} & \nu_a < \nu < \nu_i \\ t^{-3(p+1)/2}(t^{-3(p+1)/4})\nu^{-(p-1)/2} & \nu_i < \nu < \nu_c, \end{cases}\tag{5.7}$$

123

where the time dependences are reported for the thin ejecta shell and paren-
thesis are used for the thick ejecta shell.

Using the same notation as above, for SSC emission, we find:

$$F_{\nu_i \gamma_i^2} \propto t^{-5}(t^{-7/2}), \quad \nu_{i,c} \gamma_{i,c}^2 \propto t^{-3}(t^{-3/2}) \tag{5.8}$$

and

$$F_\nu \propto \begin{cases} t^{-4}(t^{-3})\nu^{1/3} & \nu \lesssim \nu_i \gamma_i^2 \\ t^{-(3p+7)/2}(t^{-(3p+11)/4})\nu^{-(p-1)/2} & \nu_i \gamma_i^2 \lesssim \nu \lesssim \nu_c \gamma_c^2. \end{cases} \tag{5.9}$$

One can see that for the synchrotron case, the flux decays rapidly
for $\nu_i < \nu < \nu_c$; for the SSC case, the flux decays even more rapidly for
$\nu_i \gamma_i^2 \lesssim \nu \lesssim \nu_c \gamma_c^2$. For both cases, the peak frequencies of the spectrum also show
a fast decrease with time. Also, for both cases, the thin ejecta case gives a
faster time decay, since the shell spreads significantly, allowing the ejecta to
cool faster.

To compare our theory with the observations, we provide relations be-
tween the temporal decay index α and the spectral index β in Table 5.1, using
the convention $F_\nu \propto t^{-\alpha} \nu^{-\beta}$.

To summarize, the emission from an adiabatically cooling source has
the following properties:

1. Its spectral index must be equal to the one at the end of the prompt
   emission phase of the gamma-ray burst, β_γ.

2. The temporal decay index must obey one of the closure relations in Table
   5.1.

	Synchrotron	SSC
	$\nu_i < \nu < \nu_c$	$\nu_i \gamma_i^2 \lesssim \nu \lesssim \nu_c \gamma_c^2$
Thick ejecta	$\alpha = 1.5\beta + 1.5$	$\alpha = 1.5\beta + 3.5$
($\Delta' = \Delta_0$)		
Thin ejecta	$\alpha = 3\beta + 3$	$\alpha = 3\beta + 5$
($\Delta' = R/\Gamma$)		

Table 5.1: Closure relations between α (decay index) and β (spectral index) for a cooling ember undergoing AE ($t_0 = t_c$, see Section 5.3.5).

3. The peak frequency of the spectrum should decrease with time as predicted in (5.6) and (5.8).

4. After some time, on the order of t_c (defined below), the spectrum should have an exponential cut-off at frequencies greater than the cooling frequency.

Points 2 and 3 above have to correspond to the same radiation mechanism (synchrotron or SSC) and the same ejecta width case (thin or thick).

If one were to consider the electrons' energy as given by the adiabatic expansion of an ideal relativistic gas, instead of using the methods of adiabatic invariance, then $\gamma \propto V^{-1/3}$ (Section 5.2, see also Section 3 of Mészáros & Rees 1999). In this case, the velocity distribution of the electrons during the adiabatic expansion phase is isotropic, therefore, $\sin \alpha'$ is a time independent constant of order unity. We calculate the temporal decay indices as done above and find the following results. For synchrotron: $\alpha = 2.3\beta + 1$ and $\alpha = 4\beta + 2$, and for SSC: $\alpha = 3.7\beta + 3$ and $\alpha = 6\beta + 4$, for the thick and thin ejecta cases, respectively. The difference in the temporal decay indices for the synchrotron

case compared to the ones on Table 5.1 is $\lesssim 20\%$ for $\beta \in [0.5 - 2]$. Because SSC has a stronger dependence on γ, the difference we find in α is larger.

So far, we have considered only the flux-freezing condition to prescribe the evolution of the magnetic field, but we can also determine the magnetic field using the equipartition consideration, that is, the energy density in the magnetic field is a constant fraction of the electrons' internal energy density (Sari, Piran & Narayan 1998). To obtain this last quantity, one needs to know γ, which could be obtained either using the adiabatic invariance methods or by the ideal gas law - as mentioned in the last paragraph. But for the equipartition consideration we will only consider the ideal gas law, because if there is a mechanism that maintains an equipartition between magnetic energy and electron energy, then that same process is also likely to keep different components of electron momentum coupled and that will lead to an ideal gas expansion law for electrons. Therefore, the magnetic field in this case is given by $B^2 \propto V^{-4/3}$, where $V \propto R^2 \Delta'$. The synchrotron and SSC emission decays, for the thick case, are both steeper by $0.3\beta + 0.3$ than the ones presented on the last paragraph, but both thin cases remain unchanged.

5.3.5   Large Angle Emission

If the central engine switches off abruptly and the gamma-ray producing ejecta has a opening angle θ_j, such as $\theta_j > \Gamma^{-1}$, Large Angle Emission (LAE) will be also present (Fenimore & Sumner 1997, Kumar & Panaitescu 2000). The LAE flux declines as $\alpha = 2 + \beta$ and the peak frequency of the spectrum decays as t^{-1}. Therefore, the AE flux generally[2] decays faster than LAE's and the AE's peak frequencies always decrease faster than LAE's.

---

[2]Except when $\beta < 1$ for the AE case of synchrotron emission from a thick ejecta shell.

The time-scales for these two phenomena, LAE and AE, are essentially the same, they are set by

$$t_c = \frac{R}{2\Gamma^2}. \tag{5.10}$$

LAE and AE start at the same time, t_0, and same site, R_0: right after the central engine has switched off, and the fluxes decline with time as:

$$F_\nu = F_0\left(1 + \frac{t - t_0}{t_c}\right)^{-\alpha}, \tag{5.11}$$

where F_0 is the flux at t_0 and α is the decay index of either LAE or AE. The shape of the LC depends on the values for t_0 and t_c (Figure 5.1); for Section 5.3.4, $t_0 = t_c$. The case $t_0 < t_c$ is unphysical, since it implies that when AE starts, the shell's electrons have not yet cooled substantially, that is, the shell's radius hasn't doubled.

If $\theta_j \lesssim \Gamma^{-1}$, then there will be no LAE, so AE would be the only emission present after the central engine turns off. On the other hand, if $\theta_j > \Gamma^{-1}$, then LAE will dominate over AE (see footnote 2). LAE will cease with the detection of the last photons coming from θ_j and, at this time, the flux will smoothly become dominated by the AE emission, that is, there will be a break in the LC to the power law decay for AE (Figure 5.1: Right). The photons from θ_j will arrive at a time $t_j \approx t_0 + R\theta_j^2/2 = t_0 + \theta_j^2\Gamma^2 t_c$.

5.3.6 Electron-positron pair-enriched ejecta

When the ejecta cools by adiabatic expansion, the thermal energy of the protons and electrons is converted back to bulk kinetic energy of the shell, increasing Γ. Even in an extreme case where all the electrons' energy goes into
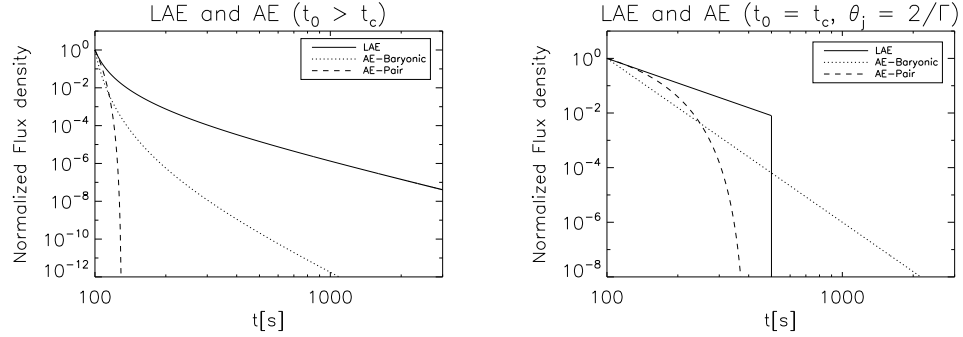
Figure 5.1: The normalized flux density, equations (5.11) and (5.12), plotted vs. observed time, assuming that the observed frequency ν is always between ν_i and ν_c (if $\nu_c < \nu$, then there is no AE, only LAE if $\theta_j > \Gamma^{-1}$, see Section 5.3.2). This emission is produced by the last ejected shell, because contributions from previously ejected shells would be buried in the emission of subsequent shells, since both LAE and AE decay very fast. Left panel: Using $t_0 = 100$ s and $t_c = 10$ s. The LAE and AE-Baryonic decay indices correspond to $\alpha = (3, 6)$, respectively, and the AE-Pair has $\delta = 8$ ($\beta = 1$, using AE: Synchrotron - thin ejecta). Right panel: Using $t_0 = t_c = 100$ s and the same α's and δ as above. In this illustrative example we have $\theta_j = 2/\Gamma$, therefore, LAE dominates over AE until $t_j = 500$ s, when AE-Baryonic takes over. This break in the LC from the LAE to the AE power law decay (which should be a smooth transition and it is done in the figure for display purposes) has never been observed.

the shell expansion, Γ increases only by a factor of ~ 2, if the protons and electrons energy is $\lesssim m_p c^2$.[3] Therefore, the effect of this change to the observed flux is less than a factor of 2, a relatively small effect. For this reason, we have used a constant Γ for the calculations done so far.

On the other hand, if the ejecta consists of $e^{\pm}$ pairs, then the increase in Γ during the adiabatic expansion would be considerable, and it would scale as $\propto \gamma^{-1}$ (the observed energy in the shell is a constant and scales as $\propto \gamma\Gamma$). Since Γ increases, then the observed time is $t - t_0 = \int_{R_0}^{R} dR/(2\Gamma^2)$. For the thin ejecta case, we find:

$$F_\nu = F_0 \Big(1 - \frac{t - t_0}{3t_c}\Big)^{\delta},\qquad(5.12)$$

with characteristic frequencies $\propto [1-(t-t_0)/(3t_c)]^4$, where $\delta = (4\beta+4, 4\beta+10)$ for the synchrotron ($\nu_i < \nu < \nu_c$) and SSC ($\nu_i\gamma_i^2 \lesssim \nu \lesssim \nu_c\gamma_c^2$) cases, respectively. The time decay index, for the $t_0 = t_c$ case, is $\delta\frac{(t/t_0)}{(4-t/t_0)}$, therefore, the LC steepens continuously. It decays even faster than the AE-Baryonic case, since the observed time gets compressed because Γ is increasing considerably. If $\theta_j > \Gamma^{-1}$, then LAE prevents it from steepening more than $2+\beta$: completely taking over the emission since essentially t_0 (Figure 5.1: Right).

---

[3]We have assumed a co-moving observer sitting in the middle of an infinite parallel shell that sees the left and right halves of the shell move away from him. Assuming the electrons' LF in the shell rest frame is 10^3 (and that the protons are essentially cold since the heating mechanism energized all particles equally), the LF of the shells would be $1+10^3 m_e/m_p = 1.5$. An observer far away would mainly detect radiation from the half moving towards him, since the radiation is beamed. This observer would see that the LF of this half has increased by a factor of ~ 2.

5.3.7   Reverse Shock emission

In this short subsection, we explore the possibility that the GRB ejecta, that just produced the prompt emission, interacts with the interstellar medium (ISM) and a reverse shock (RS) crosses it. The ejecta cools adiabatically after the RS has passed through it and we assume that it follows the Blandford-McKee self similar solution (Blandford & McKee 1976), during which Γ decays in time.

Using the same methods as in the previous subsections, we can calculate the LF of the electrons in the ejecta after the passage of the RS (see Appendix B). We find that the RS flux decays as $\propto t^{-411(p+1)/568} = t^{-2.53}$ (synchrotron emission: $\nu_i < \nu < \nu_c$, for a thin shell, using $B_\perp$ and $p = 2.5$), which gives the closure relation: $\alpha = 1.45\beta + 1.45$ (and $\alpha = 1.45\beta + 1.67$ for SSC). If we determine the electrons' LF using the ideal gas law, then the RS synchrotron flux would decay as $\propto t^{-(20p+7)/24} = t^{-2.38}$ (for the same case as above), which is still steeper than the $\propto t^{-(73p+21)/96} = t^{-2.12}$ derived by Sari & Piran (1999a), where they used $\gamma \propto V^{-1/3}$ and the equipartition consideration.

5.4   Application to the GRB early "afterglow"

AE, together with LAE, dictates the emission of the source after the central engine has completely turned off. In this section, we will determine if the early X-ray steep decay observed by *Swift* obeys our theoretical LCs for AE and LAE [4]. We will do this for each one of the cases considered in the

---

[4]If the prompt emission is attributed to synchrotron, then, for some fraction of the parameter space, the radiative cooling timescale, t_{rad} is less than t_c. However, shortly after the onset of the adiabatic expansion, $t_{rad} > t_c$, since the magnetic field decays rapidly with the expansion of the ejecta. For the SSC case, $t_{rad} \gtrsim t_c$ is very likely at the onset of the adiabatic expansion, making the radiative cooling unimportant.

previous section.

The early X-ray data shows a single power law decay with $3 \lesssim \alpha \lesssim 5$ (Nousek et al. 2006, O'Brien et al. 2006, Willingale et al. 2007). With this information, the $t_0 > t_c$ case can be ruled out, since, for this case, the theoretical shape of the LCs for LAE and AE-Baryonic is inconsistent with the early X-ray observations and the AE-Pair LC decays extremely fast (Figure 5.1: Left). Therefore, we focus on the $t_0 = t_c$ case only.

The next possibility we explore is to see if the early X-ray data obeys LAE or AE (from a baryonic ejecta). To check the validity of these two scenarios, respectively, we will take a sample of bursts and see how many cases are possibly consistent with either LAE or AE.

Our sample consists of 107 GRBs for which their spectral index during the early X-ray decay (β_x) and their temporal decay index during this phase have been previously determined (the sample of Willingale et al. 2007). We first select the bursts for which $\beta_\gamma = \beta_x$, which cuts down the sample to 55 bursts. Eight of these bursts show strong spectral evolution, inconsistent with LAE and with AE (Zhang et al. 2007: Zhang et al's sample essentially contains all our sample), which leaves us with 47 bursts. Moreover, we check how many of these satisfy the relations between α and β for LAE or AE (Table 5.1) within about a 90% confidence level, and that narrows down the sample to 20 bursts. In conclusion, only a small percentage of the sample, 19%, is consistent with LAE or AE, which leads us to suggest that, for most bursts, the early X-ray data results from some other process, and the most natural conclusion is continued central engine activity.

It has also been claimed that the γ-ray emission extrapolated to X-ray energies, together with the early X-ray data, can be well fitted with a falling

exponential followed by a power law (O'Brien et al. 2006). At first, this could be thought to be explained by a pair ejecta with $\theta_j \lesssim \Gamma^{-1}$ undergoing AE, since its LC also steepens continuously (Figure 5.1: Right). However, for 3 bursts that show this continuous steepening: GRB 050315 (Vaughan et al. 2006, Lazzati & Begelman 2006), GRB 050724 (Barthelmy et al. 2005) and GRB 060614 (Mangano et al. 2007), the theoretical LC decays too fast and can't fit the observed early X-ray LC. Therefore, we rule out the possibility that the observed early X-ray decay is from a pair ejecta undergoing AE.

Finally, we use our sample to test if the observed early X-ray steep decay is consistent with the closure relations derived for the RS (Section 5.3.7). In this case, the condition $\beta_\gamma = \beta_x$ is not necessary, therefore we start with the entire sample: 107 bursts. We eliminate 19 of these, which show strong spectral evolution, inconsistent with RS. Out of the remainder, only 26 bursts (24%) are possibly consistent with the RS (16 of these are simultaneously consistent with LAE and AE). However, this scenario could be ruled out since it would be difficult to explain the connection observed in the LC between the prompt emission and the early X-ray data. The only way they could be smoothly connected is if the prompt gamma-ray emission is produced also by the RS, for which we lack evidence.

5.5 Discussion: The central engine

The results of the last section lead us to believe that the observed early X-ray decay for $\gtrsim 70\%$ of GRBs is produced by the rapidly declining continued activity of the central engine, if we assume that there is a one-to-one correspondence between the temporal behavior of the central engine activity and the observed emission (Figure 5.2).

132

There are two other arguments that support the idea that, for most bursts, neither LAE nor AE might be consistent with the observed early X-ray decay. First, for some bursts, a break frequency has been seen passing through the X-ray band during the early steep decay, and it evolves faster than the $\propto t^{-1}$ expected in LAE: $\propto t^{-2}$ for GRB 060614 (Mangano et al. 2007[5]) and $\propto t^{-3} - t^{-4}$ for GRB 060904A (Yonetoku et al. 2008). Second, if AE is entirely responsible for this phase, then θ_j has to be very small. If this is the case, then we should have observed the edge of the jet (a jet break with a $\propto t^{-p}$ optical LC) very early on. After inspecting many optical LCs (Butler & Kocevski 2007, Liang, E.-W. et al. 2007, Liang, E.-W. et al. 2008, Melandri et al. 2008, Panaitescu & Vestrand 2008), we can conclude that most bursts with available early optical data do not show this expected jet break starting at very early times, i.e. $t <$ a few hours.

One way that we might have missed these early jet breaks could be explained by the "porcupine" model. In this model, the central engine ejects many very small angle $(\theta_j \lesssim \Gamma^{-1})$ jets. One of these jets, directed towards the observer, produces the gamma-ray emission. The central engine shuts off, and then the AE emission is produced. After a short time, all these small jets combine and give rise to a single jet with $\theta_j > \Gamma^{-1}$ that interacts with the interstellar medium, giving rise to a forward shock (optical afterglow). This model leaves no sign of a jet break. Another possible explanation for the lack of a very early jet break is that there is energy injection to the forward shock, making the $\propto t^{-p}$ optical LC more shallow. This last scenario is unlikely, as a large amount of energy is required - more than a factor of 10 increase - to

---

[5]Mangano et al. (2007) mention in their work that this could be attributed to the ν_c decrease due to adiabatic cooling of shock heated shells after an internal shock.

make a $\propto t^{-p}$ LC as shallow as $\sim t^{-1}$, which is the usual observed optical LC decay.

It has been suggested that the observed early X-ray decay is produced by the forward shock (FS) driven by the ejecta interacting with the ISM (Panaitescu 2007). This scenario has problems explaining the smooth temporal connection in the LC between the prompt emission and the early X-ray steep decay.

The model presented in this chapter has several uncertainties. For example, we are not specifying how the magnetic field is generated during the prompt emission. We are assuming: (i) that the magnetic field coherence length-scale is larger than the electron gyro-radius, based on the observations (see Appendix A), and (ii) that there are no collective plasma effects that randomize the electrons' velocity. These assumptions allow us to use the adiabatic invariant presented in Section 5.2. If, for some reason these conditions are violated, then the adiabatic invariance of electron magnetic moment can't be used. However, the light-curve from an expanding shell is similar whether we follow electron cooling via adiabatic invariance or ideal gas law and therefore, the main conclusions we have presented here are unchanged. Another assumption made in the application of this model is that *Swift*'s X-ray telescope band lies between ν_i and ν_c (in that order), which can be inferred from the spectral information of most bursts during this phase. If, however, $\nu_c < \nu_i$, then there will be no emission coming from the part of the shell that lies within an angle of Γ^{-1} to the observer line of sight - the only emission would be from LAE (if $\theta_j > \Gamma^{-1}$).
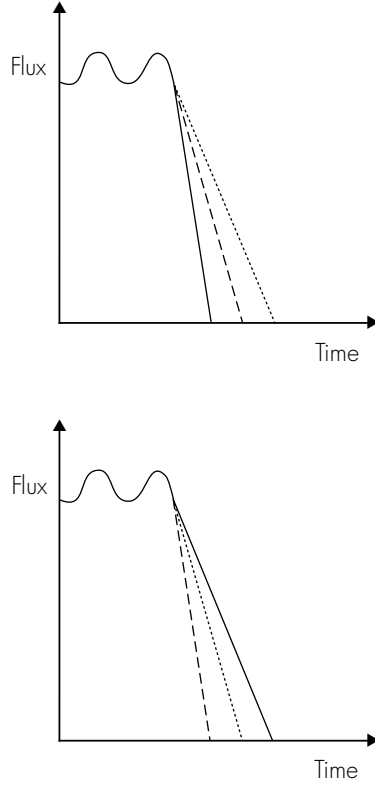
Figure 5.2: Two possible scenarios for the contribution of LAE (dotted), AE (dashed) and the rapidly declining central engine activity (solid), as seen in the X-ray band. The two "humps" represent the γ-ray detection (from *Swift* BAT), extrapolated to the X-ray band, attributed to activity of the central engine. Top panel: The case for which the central engine activity drops extremely fast and LAE and AE appear. Only $\sim 20\%$ of our sample is possibly consistent with this scenario. Bottom panel: Our preferred scenario, where the central engine activity is the dominant contribution and it decays slower than the theoretical LCs for LAE and AE.

5.6   Conclusions

We have explored the situation in which the central engine shuts off and the ejecta cools via adiabatic expansion (AE). We have derived and discussed this emission's temporal and spectral properties using a new treatment for the micro-physics of the AE: the adiabatic invariant $\gamma_\perp^2/B$, describing the electron momentum normal to the magnetic field (see summary in Section 5.3.4). At the onset of the adiabatic expansion, as B decays rapidly, this component of the momentum decreases while the parallel one remains unchanged, making the electrons more and more aligned with the local magnetic field as the ejecta expands. The adiabatic invariant enables us to calculate the electrons' energy for a collisionless magnetized plasma, if no other collective plasma effects that randomize the electrons' velocity are present.

In regards to the central engine activity, we can draw a conclusion: The fastest way that the observed flux can decline after the central engine shuts off is set by the Large Angle Emission (LAE) and the Adiabatic Expansion cooling (depending on the value of θ_j).

The early X-ray steep decay shown in most of *Swift* bursts has been attributed to LAE. In this chapter, we consider both AE and LAE for the very early X-ray data. LAE and AE both start with the assumption that the central engine shuts off abruptly. Only $\sim 20\%$ of our sample of 107 bursts is possibly consistent with either LAE or AE, thereby suggesting that the observed early X-ray steep decay for a large fraction of bursts might be produced by the rapidly declining continuation of the central engine activity.

The component of the electron's momentum parallel to the magnetic field is unconstrained by the adiabatic invariance. This component would probably cool via Inverse Compton scattering with synchrotron photons. Another

possibility is that the electrons are scattered by small scale fluctuations in the magnetic field, which would effectively couple the parallel and perpendicular components of their momentum, resulting in an adiabatic cooling similar to that in the ideal gas case, Section 5.2 (personal communication, Granot).

Any process that does not rely on the central engine activity to explain the observed early X-ray steep decay (for example: RS, FS) has problems explaining the smooth temporal connection observed in the LC between the prompt emission and the early X-ray steep decay.

Chapter 6

Conclusions

We analyze the >100 MeV data for 3 GRBs detected by the *Fermi* satellite (GRBs 080916C, 090510, 090902B) and find that these photons were generated via synchrotron emission in the external forward shock (Kumar & Barniol Duran 2009, 2010). We arrive at this conclusion by four different methods as follows. (1) We check the light curve and spectral behavior of the >100 MeV data, and late time X-ray and optical data, and find them consistent with the so called "closure relations" – which is a relation between the spectral and temporal decay indices – for the external forward shock radiation. (2) We calculate the expected external forward shock synchrotron flux at 100 MeV, which is essentially a function of the total energy in the burst alone, and it matches the observed flux value. (3) We determine the external forward shock model parameters using the >100 MeV data (a very large phase space of parameters is allowed by the high energy data alone), and for each point in the allowed parameter space we calculate the expected X-ray and optical fluxes at late times (hours to days after the burst) and find these to be in good agreement with the observed data for the entire parameter space allowed by the >100 MeV data. (4) We calculate the external forward shock model parameters using only the late time X-ray, optical and radio data and using these parameters estimate the expected flux at >100 MeV at the end of the sub-MeV burst (and at subsequent times) and find that to be entirely

consistent with the high energy data obtained by *Fermi*/LAT. The ability of a simple external forward shock, with two empirical parameters (total burst energy and energy in electrons) and two free parameters (circumstellar density and energy in magnetic fields), to fit the entire data from the end of the burst (1 - 50 s) to about a week, covering more than eight decades in photon frequency — $>10^2$ MeV, X-ray, optical and radio — provides compelling confirmation of the external forward shock synchrotron origin of the >100 MeV radiation from these *Fermi* GRBs. Moreover, the parameters determined in points (3) and (4) show that the magnetic field required for synchrotron radiation in these GRBs is consistent with shock-compressed magnetic field of the circumstellar medium with pre-shocked values of a few tens of micro-Gauss.

We investigate whether electrons can be accelerated to energies such that they radiate synchrotron photons with energy up to about 10 GeV in the external forward shock scenario with a weak magnetic field (Barniol Duran & Kumar 2011a) – consistent with shock compressed upstream magnetic field of a few tens of micro-Gauss. We do this using two methods: (i) we check if these electrons can be confined to the shock front by the weak upstream magnetic field; and (ii) we calculate radiative losses while they are being accelerated. We find that these electrons remain confined to the shock front, as long as the upstream magnetic field is $\gtrsim 10\mu$G, and do not suffer substantial radiative losses; the only condition required is that the synchrotron radiation produced by the external-reverse-shock heated GRB jet be not too bright: peak flux less than 1 Jy in order to produce photons of 100 MeV, and less than ~ 100 mJy for producing 1-GeV photons. We also find that the acceleration time for electrons radiating at 100 MeV is a few seconds (in observer frame), and the acceleration time is somewhat longer for electrons radiating at a few GeV.

This could explain the lack of >100 MeV photons for the first few seconds after the trigger time for long GRBs reported by the *Fermi* Satellite, and also the slight lag between photons of GeV and 100 MeV energies. We model the onset of the external forward shock light curve in this scenario and find it consistent with the sharp rise observed in the 100-MeV light curve of GRB 080916C and similar bursts.

We carried out a detailed analysis of the late time afterglow data of GRB 090902B using a very careful accounting of the Inverse Compton losses (Barniol Duran & Kumar 2011b). We find that in the context of the external forward shock model, the only viable option to explain the X-ray and optical data of GRB 090920B is to have the electron energy distribution deviate from a power-law shape and exhibit some slight curvature immediately downstream of the shock front (we explored other models that rely on a single power-law assumption, but they all fail to explain the observations). We find the fraction of the energy of shocked plasma in magnetic field to be $\sim 10^{-6}$ using late time afterglow data, which is consistent with the value obtained using early gamma-ray data. Studies like the present one might be able to provide a link between GRB afterglow modeling and numerical simulations of particle acceleration in collisionless shocks. We also provide detailed calculations for the early ($\lesssim 10^3$ s) high energy (> 100 MeV) emission and confirm that it is consistent with origin in the external forward shock. We investigated the possibility that the ~ 10 keV excess observed in the spectrum during the prompt phase also has its origin in the external forward shock and found the answer to be negative.

Finally, the *Swift* satellite early X-ray data shows a very steep decay in most of GRBs light curves. This decay is either produced by the rapidly declining continuation of the central engine activity or by the left-over radiation

when the central engine shuts off. The latter scenario consists of the emission from an "ember" that cools via adiabatic expansion, and the large angle emission if the jet angle is larger than the inverse of the source Lorentz factor. In this work, we calculate the temporal and spectral properties of the emission from such a cooling ember, providing a new treatment for the micro-physics of the adiabatic expansion. We use the adiabatic invariance of $p_\perp^2/B$ ($p_\perp$ is the component of the electrons' momentum normal to the magnetic field, B) to calculate the electrons' Lorentz factor during the adiabatic expansion; the electron momentum becomes more and more aligned with the local magnetic field as the expansion develops. We compare the expected X-ray flux during the adiabatic expansion (and the large angle emission) with the current observations of the early X-ray data and find that only $\sim 20\%$ of our sample of 107 bursts is potentially consistent with this model. This leads us to believe that, for most bursts, the central engine does not turn off completely during the steep decay of the X-ray light curve; therefore, this phase is produced by the continued rapidly declining activity of the central engine (Barniol Duran & Kumar 2009).

Appendices

Appendix A

Electron gyro-radius versus Magnetic field length-scale

The observed peak energy in the prompt phase of a GRB is given by $\nu_i = (1.15 \times 10^{-8} eV) B \gamma_i^2 \Gamma (1+z)^{-1}$, assuming synchrotron emission. The value of Γ can be constrained to be a few hundred. There is a wide range of allowed values for γ_i. For $\gamma_i = 10^3$, $\nu_i = 100$ keV, $\Gamma = 100$ and $z = 1$, then $B = 2 \times 10^5$ G, and in that case, the electrons' gyro-radius is $r = m_e c^2 \gamma_i / (eB) \approx 10$ cm.

If the magnetic field responsible for the prompt emission is the frozen-in field from the central explosion, then it decays on a length-scale on the order of the source size, which is much larger than the electrons' gyro-radius and the adiabatic invariant presented in Section 5.2 can be used.

If the field is produced locally (e.g. by the Weibel instability), then we need to estimate its coherence length and compare it with the electrons' gyro-radius. For instance, magnetic field generated by the Weibel instability will have a coherence length on the order of the plasma length $\lambda_B = c/\omega_p$, where $\omega_p = (4\pi e^2 n/m_e)^{1/2} = 6 \times 10^4 (n)^{1/2}$ s^{-1} and n is the co-moving electron number density in units of cm^{-3}. For the prompt emission, recent studies have shown that the radius of emission is on the order of 10^{15-16} cm or even larger (Kumar et al. 2007, Racusin et al. 2008, Zou, Piran & Sari 2009, Kumar & Narayan 2009), therefore $n = 5 \times 10^{5-8}$ cm^{-3} (see footnote 1 in Section 5.2), which gives $\lambda_B = 20 - 700$ cm, making λ_B larger than r by at least a factor of

2. Moreover, this magnetic field decays extremely fast in time (in about ω_p^{-1}), which would be less than 10^{-8} s in the source co-moving frame or 10^{-10} s in the observer frame. This locally generated magnetic field cannot be responsible for the prompt emission, unless it is sustained for at least ~ 1 s (the co-moving time-scale of a few millisecond prompt pulse), which would require a much larger λ_B (Keshet et al. 2009 mention that the field must persist over $10^{10}\lambda_B$ downstream, which in this case would be $\sim 10^{12}$ cm). Therefore, it is safe to assume that even if the field is generated locally $r << \lambda_B$, allowing us to use the adiabatic invariant.

The prompt emission phase could also be attributed to the SSC emission, which requires smaller values for γ_i and B. For $\gamma_i = 10^2$, then $B = 2 \times 10^3$ G, which gives $r \approx 100$ cm $\sim \lambda_B$. But as mentioned above, the field has to be coherent on length-scale $\sim 10^{12}$ cm in order that it does not decay away on time $\lesssim 1$ s.

Appendix B

Reverse Shock emission calculation

After the RS has crossed the ejecta, it roughly follows the Blandford-McKee self-similar solution (Blandford & McKee 1976), in which the bulk LF and pressure of the shocked ISM are given by:

$$\gamma(t,r) = \gamma(t)\chi^{-\frac{1}{2}}, \quad P(r,t) = 4m_p c^2 n[\gamma(t)]^2 \chi^{-\frac{17-4s}{12-3s}}, \tag{B.1}$$

where $\gamma(t) \propto R^{-(3-s)/2}$ is the LF of material just behind the shock, $n \propto R^{-s}$ is the ISM particle number density, χ is the similarity variable and m_p is the proton mass (see, e.g, Sari 1997).

Let us assume that the ejecta is at χ_{ej} and it has a pressure P_{ej} and a LF Γ_{ej}, which - because of pressure and velocity equilibrium at the contact discontinuity - should be the same as the bulk LF and pressure of the shocked ISM at χ_{ej} (B.1). The pressure in the ejecta for the thin case ($\Delta' = R/\Gamma_{ej}$) is given by $P_{ej} \propto V^{-1}\gamma_\perp$, where $V \propto R^2\Delta'$, and using the adiabatic invariance (equation 5.1), we can use $\gamma_\perp \propto B_\perp^{1/2}$, where $B_\perp$ is given in Section 5.3.1. Therefore, we have $P_{ej} \propto R^{-4}\Gamma_{ej}^{3/2}$ and using (B.1) and the contact discontinuity equilibrium conditions we obtain:

$$\Gamma_{ej} = \gamma(t)\chi_{ej}^{-\frac{1}{2}}, \quad P_{ej} = 4m_p c^2 n[\gamma(t)]^2 \chi_{ej}^{-\frac{17-4s}{12-3s}}. \tag{B.2}$$

We can solve for Γ_{ej} in terms of R, which gives $\Gamma_{ej} \propto R^{-\frac{2(63-32s+4s^2)}{32-7s}}$. For uniform ISM ($s = 0$), we can determine the observed time by $t - t_0 = \int_{R_0}^{R} dR/(2\Gamma_{ej}^2)$ and following the procedure on Section 5.3.3, we can find that the RS shock flux decays as $\propto t^{-411(p+1)/568} = t^{-2.53}$ for $p = 2.5$ ($\nu_i < \nu < \nu_c$).

We can also determine the electrons' LF by using the ideal gas law. For this case, $\gamma \propto V^{-1/3}$, therefore the pressure in the ejecta is $P_{ej} \propto V^{-4/3}$. For the thin ejecta case, we can repeat the calculation done before (B.2), just modifying P_{ej}, and we obtain $\Gamma_{ej} \propto R^{-(7-2s)/2}$. To calculate the RS synchrotron emission for uniform ISM, we can use $B_\perp \propto (R\Delta')^{-1}$ and we can follow the procedure on Section 5.3.3, but as mentioned before, for this case $\sin \alpha' \sim 1$. We find that the RS decays in this case as $\propto t^{-(20p+7)/24} = t^{-2.38}$ for $p = 2.5$ ($\nu_i < \nu < \nu_c$). If we determine the magnetic field using the equipartition consideration and determine the electrons' LF with the ideal gas law, then we get the same result reported by Sari & Piran (1999a).

Bibliography

[1] Abdo A.A. et al., 2009a, Science, 323, 1688

[2] Abdo A.A. et al., 2009b, preprint (arXiv:0908.1832)

[3] Abdo A.A. et al., 2009c, Nature, 462, 331

[4] Abdo A.A. et al., 2009d, ApJ, 706, L138

[5] Achterberg A., Ball L., 1994, A&A, 284, 687

[6] Achterberg A., Gallant Y. A., Kirk J. G., Guthmann A. W., 2001, MN-RAS, 328, 393

[7] Akerlof C. et al., 1999, Nature, 398, 400

[8] Asano K., Inoue S., Mészáros P., 2010, ApJ, 725, L121

[9] Axford W. I., Leer E., Skadron G., 1978, Proc. 15 Int. Cosmic Ray Conf. (Plovdiv) 11, B'lgarska Akademiia na Naukite, Sofia, Bulgaria, p. 132

[10] Band D. et al., 1993, ApJ, 413, 281

[11] Baring M.G., 2004, Nucl. Phys. B, 136, 198

[12] Barniol Duran R., Kumar P., 2011a, MNRAS, 412, 522

[13] Barniol Duran R., Kumar P., 2011b, MNRAS, submitted

[14] Barthelmy, S.D. et al., 2005, Nature, 438, 994

[15] Bell A.R., 1978, MNRAS, 182, 147

[16] Beloborodov A., 2010, MNRAS, 407, 1033

[17] Blandford R. D., McKee C. F., 1976, Phys. Fluids, 19, 1130

[18] Blandford R.D., Ostriker J.P., 1978, ApJ, 221, L29

[19] Blandford R.D., Eichler D., 1987, Phys. Rep., 154, 1

[20] Bloom J.S. et al., 1999, Nature, 401, 453

[21] Bloom J.S., Djorgovski S.G., Kulkarni S.R., 2001, ApJ, 554, 678

[22] Blumenthal G.R., 1970, Phys. Rev. D, 1, 1596

[23] Blumnthal G.R., Gould R.J., 1970, Rev. Modern Phys., 42, 237

[24] Boër M., Atteia J.L., Damerdji Y., Gendre B., Klotz A., Stratta G., 2006, ApJ, 638, L71

[25] Bošnjak Ž., Daigne F., Dubus G., 2009, A&A, 498, 677

[26] Butler N., Kocevski D., 2007, ApJ, 663, 407

[27] Cenko S.B. et al. 2010, ApJ, submitted (arXiv:1004.2900)

[28] Cheng K.S., Wei D.M., 1996, MNRAS, 283, L133

[29] Chincarini G. et al., 2007, ApJ, 671, 1903

[30] Christensen L., Hjorth J., Gorosabel J., 2004, A&A, 425, 913

[31] Cohen E., Piran T., Sari R., 1998, ApJ, 509, 717

[32] Corsi A., Guetta D., Piro L., 2010, ApJ, 720, 1008

[33] Costa E. et al., 1997, Nature, 387, 783

[34] Couch S.M., Milosavljević M., Nakar E., 2008, ApJ, 688, 462

[35] Cucchiara A., Fox D.B., Tanvir N., Berger E., 2009, GCN Circ., 9873

[36] Daigne F., Bošnjak Ž., Dubus G., 2011, A&A, 526, A110

[37] de Jager O.C., Harding A.K., Michelson P.F., Nel H.I., Nolan P.L., Sreekumar P., Thompson D.J., 1996, ApJ, 457, 253

[38] De Pasquale M. et al. 2010, ApJ, 709, L146

[39] Dermer C.D., Mitman K.E., 1999, ApJ, 513, L5

[40] Eichler D., Livio M., Piran T., Schramm D.N., 1989, Nature, 340, 126

[41] Evans P.A. et al., 2007, A&A, 469, 379

[42] Evans P.A. et al., 2009, MNRAS, 397, 1177

[43] Falcone A.D. et al., 2006, ApJ, 641, 1010

[44] Fan Y.Z., Dai Z.G., Huang Y.F., Lu T., 2002, Chinese J. Astron. Astrophys., 2, 449

[45] Fan Y.Z., Wei D.M., Wang C.F., 2004, A&A, 424, 477

[46] Fan Y.Z., Piran T., 2008, Front. Phys. China, 3, 306

[47] Feng S.Y., Dai Z.G., 2010, preprint (arXiv:1011.3103)

[48] Fenimore E., Sumner M., 1997, "All-Sky X-ray Observations in the Next Decade", eds. M. Matsuoka and N. Kawai, Riken Institute, Japan, p. 167 (astro-ph/9705052)

[49] Fong W., Berger E., Fox D.B., 2010, ApJ, 708, 9

[50] Fox D.W. et al. 2003, Nature, 422, 284

[51] Frail D.A., Kulkarni S.R., Nicastro S.R., Feroci M., Taylor G.B., 1997, Nature, 389, 261

[52] Frail D.A. et al., 2001, ApJ, 562, L55

[53] Galama et al., 1998, Nature, 395, 670

[54] Gallant Y.A., Achterberg A., 1999, MNRAS, 305, L6

[55] Gao W.-H., Mao J., Xu D., Fan Y.Z., 2009, ApJ, 706, L33

[56] Gehrels N. et al., 2004, ApJ, 611, 1005

[57] Gehrels N., Ramirez-Ruiz E., Fox D.B., 2009, ARA&A, 47, 567

[58] Ghirlanda G., Ghisellini G., Nava L., 2010, A&A, 510, 7

[59] Ghisellini G., Ghirlanda G., Nava L., 2010, MNRAS, 403, 926

[60] Giannios D., Spruit H.C., 2007, A&A, 469, 1

[61] Giannios D., Mimica P., Aloy M.A., 2008, A&A, 478, 747

[62] Giuliani A. et al., 2010, ApJ, 708, L84

[63] Goodman J., MacFadyen A., 2008, J. Fluid Mech., 604, 325

[64] Greiner J. et al., 2009, A&A, 498, 89

[65] Grupe D., Hoverstein E., 2009, GCN Circ., 9341

[66] Guidorzi C. et al., 2009, GCN Circ., 9875

[67] Guilbert P.W., Fabian A.C., Rees M.J., 1983, MNRAS, 205, 593

[68] Gupta N, Zhang B., 2007, MNRAS, 380, 78

[69] Harrison F.A. et al., 1999, ApJ, 523, L121

[70] Jackson J. D., 1998, Classical Electrodynamics. Wiley, New York

[71] Jokipii J.R., 1987, ApJ, 313, 842

[72] Jones F.C., 1968, Phys.Rev., 167, 1159

[73] Kaneko Y., Preece R.D., Briggs M.S., Paciesas W.S., Meegan C.A., Band D.L., 2006, ApJS, 166, 298

[74] Katz J.I., Piran T., 1997, ApJ, 490, 772

[75] Keshet U., Katz B., Spitkovsky A., Waxman E., 2009, ApJ, 693, L127

[76] Klebesadel R.W., Strong I.B., Olson R.A., 1973, ApJ, 182, L85

[77] Klotz A., Gendre B., Stratta G., Atteia J.L., Boër M., Malacrino F., Damerdji Y., Behrend R., 2006, A&A, 451, L39

[78] Kouveliotou C., Meegan C.A., Fishman G.J., Bhat N.P., Briggs M.S., Koshut T.M., Paciesas W.S., Pedleton G.N., 1993, ApJ, 413, L101

[79] Krymskii G. F., 1977, Sov. Phys. Dokl., 22, 327

151

[80] Kumar P., 2000, ApJ, 538, 125

[81] Kumar P., Panaitescu A., 2000, ApJ, 541, L51

[82] Kumar P. et al. 2007, MNRAS, 376, L57

[83] Kumar P., McMahon E., 2008, MNRAS, 384, 33

[84] Kumar P., Narayan R., Johnson J.L., 2008, MNRAS, 388, 1729

[85] Kumar P., Barniol Duran R., 2009, MNRAS, 400, L75

[86] Kumar P., Narayan R., 2009, MNRAS, 395, 472

[87] Kumar P., Barniol Duran R., 2010, MNRAS, 409, 226

[88] Lazar A., Nakar E., Piran T., 2009, ApJ, 695, L10

[89] Lazzati D., Begelman M.C., 2006, ApJ, 641, 972

[90] Lemoine M., Pelletier G., Revenu B., 2006, ApJ, 645, L129

[91] Li W., Filippenko A.V., Chornock R., Saurabh J., 2003, ApJ, 586, L9

[92] Li Z., 2010, ApJ, submitted (arXiv:1004.0791)

[93] Liang E.-W., Zhang B.-B., Zhang B., 2007, ApJ, 670, 565

[94] Liang E.-W., Racusin J.L., Zhang B., Zhang B.-B., Burrows D.N., 2008, ApJ, 675, 528

[95] Lithwick Y., Sari R., 2001, ApJ, 555, 540

[96] Liu R.-Y., Wang X.-Y., 2011, ApJ, 730, 1

[97] Lyutikov M., Blandford R., 2003, preprint (arXiv:astro-ph/0312347)

[98] MacFadyen A.I., Woosley S.E., 1999, ApJ, 524, 262

[99] Mangano V. et al., 2007, A&A, 470, 105

[100] McBreen S. et al., 2010, A&A, 516, 71

[101] Medvedev M.V., Loeb A., 1999, ApJ, 526, 697

[102] Meegan C.A., Fishman G.J., Wilson R.B, Horack J.M., Brock M.N., Paciesas W.S., Pendleton G.N., Kouveliotou C., 1992, Nature, 355, 143

[103] Mészáros P., 2006, Rep. Prog. Phys., 69, 2259

[104] Mészáros P., Rees M.J., 1993, ApJ, 405, 278

[105] Mészáros P., Rees M.J., 1997, ApJ, 476, 232

[106] Mészáros P., Rees M.J., 1999, MNRAS, 306, L39

[107] Mészáros P., Rees M.J., 2000, ApJ, 530, 292

[108] Melandri A. et al, 2008, ApJ, 686, 1209

[109] Milosavljević M., Nakar E., 2006, ApJ, 651, 979

[110] Morsony B.J., Workman J.C., Lazzati D., Medvedev M.V., 2009, MNRAS, 392, 1397

[111] Nakar E., 2007, Phys. Rep., 442, 166

[112] Nakar E., Ando S., Sari R., 2009, ApJ, 703, 675

[113] Narayan R., Paczyński B., Piran T., 1992, ApJ, 395, L83

[114] Norris J.P., Bonnell J.T., 2006, ApJ, 643, 266

[115] Norris J.P., Share G.H., Messina D.C., Dennis B.R., Desai U.D, Cline T.L., Matz S.M., Chupp E.L., 1986, ApJ, 301, 213

[116] Nousek J.A. et al., 2006, ApJ, 642, 389

[117] O'Brien P. et al, 2006, ApJ, 647, 1213

[118] Omodei N. et al., 2009, Proceedings for 31st Int'l Cosmic-Ray Conference, preprint (arXiv:0907.0715)

[119] Paczyński B., 1991, Acta Astron., 41, 257

[120] Paczyński B., Rhoads J.E., 1993, ApJ, 418, L5

[121] Paczyński B., Xu G., 1994, ApJ, 427, 708

[122] Panaitescu A., 2007, MNRAS, 379, 331

[123] Panaitescu A., Kumar P., 2000, ApJ, 543, 66

[124] Panaitescu A., Kumar P., 2001, ApJ, 560, L49

[125] Panaitescu A., Kumar P., 2002, ApJ, 571, 779

[126] Panaitescu A., Kumar P., 2004, MNRAS, 353, 511

[127] Panaitescu A., Mészáros P., Burrows D., Nousek J., Gehrels N., O'Brien P., Willingale R., 2006, MNRAS, 369, 2059

[128] Panaitescu A., Vestrand W.T., 2008, MNRAS, 387, 497

[129] Pandey S.B., Zheng W., Yuan F., Akerlof C., 2009, GCN Circ., 9878

[130] Pandey S.B. et al. 2010, ApJ, 714, 799

[131] Pe'er A., Mészáros P, Rees M.J., 2006, ApJ, 642, 995

[132] Pelletier G., Lemoine M., Marcowith A., 2009, MNRAS, 393, 587

[133] Piran T., 1997, in Unsolved Problems in Astrophysics, edited by J. Bahcall and J. Ostriker (Princeton University Press, Princeton, NJ), p. 273

[134] Piran T., 2004, Rev. Modern Phys., 76, 1143

[135] Piran T., Nakar E., 2010, ApJ, 718, L63

[136] Piran T., Kumar P., Panaitescu A., Piro L., 2001, ApJ, 560, L167

[137] Piro L., 2001, in Gamma-ray Bursts in the Afterglow Era, edited by E. Costa, F. Frontera, and J. Hjorth (Springer, Berlin), p. 97

[138] Preece R.D. et al., 2002, ApJ, 581, 1248

[139] Racusin J.L. et al. 2008, Nature, 455, 183

[140] Rees M.J., Mészáros P., 1992, MNRAS, 258, 41P

[141] Rees M.J., Mészáros P., 1994, ApJ, 430, L93

[142] Rees M.J., Mészáros P., 2005, ApJ, 628, 847

[143] Rhoads J.E., 1999, ApJ, 525, 737

[144] Roming P. et al., 2006, ApJ, 652, 1416

[145] Ruderman M., 1975, in 7th Texas Symposium on Relativistic Astrophysics, Dallas, 1974, Ann. N.Y. Acad. Sci. 262, 164

[146] Rybicki G. B., Lightman A. P., 1979, Radiative Processes in Astrophysics. Wiley-Interscience Press, New York

155

[147] Ryde F., Pe'er A., 2009, ApJ, 702, 1211

[148] Sari R., 1997, ApJ, 489, L37

[149] Sari R., Esin A.A., 2001, ApJ, 548, 787

[150] Sari R., Piran T., 1999a, ApJ, 517, L109

[151] Sari R., Piran T., 1999b, ApJ, 517, L109

[152] Sari R., Piran T., Halpern, J.P., 1999, ApJ, 519, L17

[153] Sari R., Piran T., Narayan R., 1998, ApJ, 497, L17

[154] Shen R., Kumar P., Robinson E.L., 2006, MNRAS, 371, 1441

[155] Sironi L., Goodman J., 2007, ApJ, 671, 1858

[156] Sironi L., Spitkovsky A., 2011, ApJ, 726, 75

[157] Spitkovsky A., 2008a, ApJ, 673, L39

[158] Spitkovsky A., 2008b, ApJ, 682, L5

[159] Swenson C., Stratta G., 2009, GCN Circ., 9877

[160] Tagliaferri G. et al., 2005, Nature, 436, 985

[161] Taylor G.B., Frail D.A., Berger E., Kulkarni S.R., 2004, ApJ, 609, L1

[162] Thompson C., 1994, MNRAS, 270, 480

[163] Toma K., Wu X.-F., Mészáros P., 2010, MNRAS, submitted (arXiv:1002.2634)

[164] van der Horst A.J., Kamble A.P., Wijers R.A.M.J., Kouveliotou C., 2009, GCN Circ., 9883

[165] van Paradijs J. et al., 1997, Nature, 386, 686

[166] Vaughan S. et al., 2006, ApJ, 638, 920

[167] Wang X.-Y., He H.-N., Li Z., Wu X.-F., Dai Z.-G., 2010, ApJ, 712, 1232

[168] Wen L., Panaitescu A., Mészáros P., 1997, ApJ, 486, 919

[169] Wijers R.A.M.J., Rees M.J., Mészáros P., 1997, MNRAS, 288, L51

[170] Willingale R. et al., 2007, ApJ, 662, 1093

[171] Woosley S.E., 1993, ApJ, 405, 273

[172] Woosley S.E., Bloom J.S., 2006, ARA&A, 44, 507

[173] Workman J.C., Morsony B.J., Lazzati D., Medvedev M.V., 2008, MN-RAS, 386, 199

[174] Yonetoku D. et al., 2008, PASJ, 60, 263

[175] Zhang B., 2007, Chinese J. Astron. Astrophys., 7, 1

[176] Zhang B., Mészáros P., 2004, Int. J. Modern Phys. A, 19, 2385

[177] Zhang B., Kobayashi S., 2005, ApJ, 628, 315

[178] Zhang B., Kobayashi S., Mészáros P., 2003, ApJ, 595, 950

[179] Zhang B., Fan Y.Z., Dyks J., Kobayashi S., Mészáros P., Burrows D.N., Nousek J.A., Gehrels N., 2006, ApJ, 642, 354

[180] Zhang B.-B., Liang E.-W., Zhang B., 2007, ApJ, 666, 1002

[181] Zhang B.-B. et al., 2011, ApJ, 730, 141

[182] Zhao X., Li Z., Bai J., 2011, ApJ, 726, 89

[183] Zou Y.C., Fan Y.Z., Piran T., 2009, MNRAS, 396, 1163

[184] Zou Y.C., Piran T., Sari R., 2009, ApJ, 692, 92

Vita

Rodolfo Jose Barniol Duran attended High School at the Humboldt German School in Guayaquil, Ecuador. In May 2004, he received the degree of Bachelor of Science in Physics Engineering from Monterrey Tech (ITESM) in Monterrey, Mexico. During his undergraduate studies, he spent a year in the University of California at Berkeley as an exchange student, where his interest in Astrophysics started. In Fall 2004, he began graduate studies at the University of Texas at Austin.

Permanent address: Ave. Diagonal 219, Colinas de Los Ceibos
                                    Guayaquil, Ecuador

This dissertation was typeset with LaTeX[†] by the author.

[†]LaTeX is a document preparation system developed by Leslie Lamport as a special version of Donald Knuth's TeX Program.